A COMPREHENSIVE STUDY OF CAVITIES ON THE SUN: STRUCTURE, FORMATION, AND EVOLUTION

by

Nishu Karna
A Dissertation
Submitted to the
Graduate Faculty
of
George Mason University
in Partial fulfillment of
The Requirements for the Degree
of
Doctor of Philosophy
Computational Science and Informatics

Committee:

________________________	Dr. Jie Zhang, Dissertation Director
________________________	Dr. William Dean Pesnell, Committee Member
________________________	Dr. Robert Weigel, Committee Member
________________________	Dr. Arthur Poland, Committee Member
________________________	Dr. Joseph Weingartner, Committee Member
________________________	Dr. Kevin Curtin, Acting Department Chair
________________________	Dr. Donna M. Fox, Associate Dean, College of Student Affairs and Special Programs, College of Science
________________________	Dr. Peggy Agouris, Dean, College of Science
Date: ____________________	Spring Semester 2016 George Mason University Fairfax, VA

A Comprehensive Study of Cavities on the Sun: Structure, Formation, and Evolution

A dissertation submitted in partial fulfillment of the requirements for the degree of Doctor of Philosophy at George Mason University

By

Nishu Karna
Master of Science
George Mason University, 2012
Bachelor of Science
St. Cloud State University, 2010

Director: Dr. Jie Zhang, Professor
Department of Physics and Astronomy

Spring Semester 2016
George Mason University
Fairfax, VA

Dedication

I dedicate this dissertation to my parents Mahendra and Manjula, my family and friends who always encourage and support me in this journey.

Acknowledgments

I would like to thank the following people who made this possible. First and foremost I would like to thank my research advisor Dr. William Dean Pesnell who encouraged and supported me to join Graduate school. Special thanks to my advisor Dr. Jie Zhang for his encouragement, continuous support, and patience. Their guidance and insight have made this whole graduate experience possible. I would like to thank my dissertation committee: Dr. Robert Weigel, Dr. Art Poland and Dr. Joseph Weingartner for giving me their time and effort. My deepest gratitudes to my family and friends for their love, concern and encouragement. I could not have done without the support of my family, friends, and instructors.

Table of Contents

List of Tables

List of Figures

Abstract

A COMPREHENSIVE STUDY OF CAVITIES ON THE SUN: STRUCTURE, FORMATION, AND EVOLUTION

Nishu Karna

George Mason University, 2016

Dissertation Director: Dr. Jie Zhang

Coronal cavities are large scale structures in the solar corona that are closely related to the long-term evolution of the magnetic field in the photosphere as well as associated with energetic solar activity such as prominence eruptions and coronal mass ejections (CMEs), which are a primary driver of space weather. Coronal cavities are observed as elliptical-shaped and relatively low density dark regions above the solar limb in extreme ultraviolet (EUV), X-ray, and white-light coronal images. However, the nature of their magnetic field, how they form and their relationship to solar activity are not well understood. In this dissertation, several important questions regarding coronal cavity origin, structure, and relation to the solar cycle are addressed.

To effectively and efficiently identify coronal cavities, we constructed limb synoptic maps from annuli located above the solar limb in EUV images from the Atmospheric Imager Assembly (AIA) instrument on board the Solar Dynamics Observatory (SDO). Based on this method, we have created the largest existing coronal cavity catalog, starting from CR 2097 to CR 2159 (May 20, 2010 - February 1, 2015) and published it online at spaceweather.gmu.edu/projects/synop. The catalog lists the number of cavities seen in each Carrington Rotation along with their length, height, width, heliographic longitudes and

latitudes of the appearance and disappearance of the cavity, and tilt angle. We examined correlations between height, width, and length of 429 coronal prominence cavities. Based on the fitting of the shape of the cross section, we classified cavities into three types: prolate, oblate, and circular. We found that the cavities of all shapes are common in shorter lengths while circular and oblate cavities are more common in longer lengths. In general, we found that the overall 3-D topology of long stable cavities can be characterized as a long tube with an elliptical cross-section. The results on the 3-D geometric shape provide us the necessary information for further study of the formation and stability mechanism of cavities.

Next, we investigated the pattern of cavity location and found that cavities systematically drift towards the pole during the rise of the solar maximum. We found that cavities form a belt in both hemisphere in a plot similar to the classical butterfly diagram of sunspots, which we call that the cavity belt. Our analysis showed that the cavity belts migrate towards higher latitude with time and the cavity belts disappear after the polar magnetic field reversal. This led us to conclude that the polar crown cavity position can be used to establish the time of the polar magnetic field reversal. Further, we measured the drift speed of the cavity belt and found that this drift is caused by the meridional flow. Lastly, we studied the underlying magnetic field of a circumpolar crown cavity that was observed for several Carrington Rotations. Our results showed that the underlying polarity inversion line of cavities is formed between the trailing part of decayed active regions and the unipolar magnetic field in the pole. The long life of cavities was due to the continuous and sustained addition of trailing flux from multiple active regions as their remnants diffused toward the pole.

The research described in this thesis has improved our understanding of the structure, formation, and stability of coronal magnetic structures. Future work includes a comprehensive study of the magnetic structures of cavities on both short and long timescales and their instability. This study will ultimately help improve prediction of eruptions that can mitigate space weather effects on terrestrial technology systems.

Chapter 1: Introduction

1.1 Space Weather

The term "space weather" describes the state of the space environment surrounding the Earth, including conditions in the magnetosphere, ionosphere and thermosphere influenced by the change in the particles traveling outside the Sun due to solar activity (Schwenn, 2006). Space weather effects can reduce satellite operations, damage electronic circuits onboard spacecraft, degrade solar cells, disrupt polar aircraft flights, cause radio communication problems, cause radiation hazards to orbiting astronauts, etc. (Shea and Smart, 2012). Figure 1.1 is NASAs illustrative depiction of the Sun-Earth connection that drives space weather. One of the primary drivers of space weather is the Coronal Mass Ejection (CME) (Hudson, Bougeret, and Burkepile, 2006), an explosion of the magnetic fields and plasma from the Sun's corona. CMEs propagate through interplanetary space, and as they pass through Earth's orbit, they are likely to impact the Earth's magnetosphere and cause a geomagnetic storm (Zhang *et al.*, 2007a,b).

Much research is ongoing to study the kinematical and morphological evolution of CMEs. Satellites such as Solar and Heliospheric Observatory (SOHO), Solar TErrestrial RElations Observatory (STEREO) are routinely observing CMEs. One important component of CMEs is the coronal cavity. When seen in white light observations, cavities are often observed as one part in a three-part CME (Illing and Hundhausen, 1986). These parts are the bright core of an erupting prominence, a relatively dark cavity surrounding the prominence, and a bright leading loop surrounding the cavity (seen in Figure 1.2).

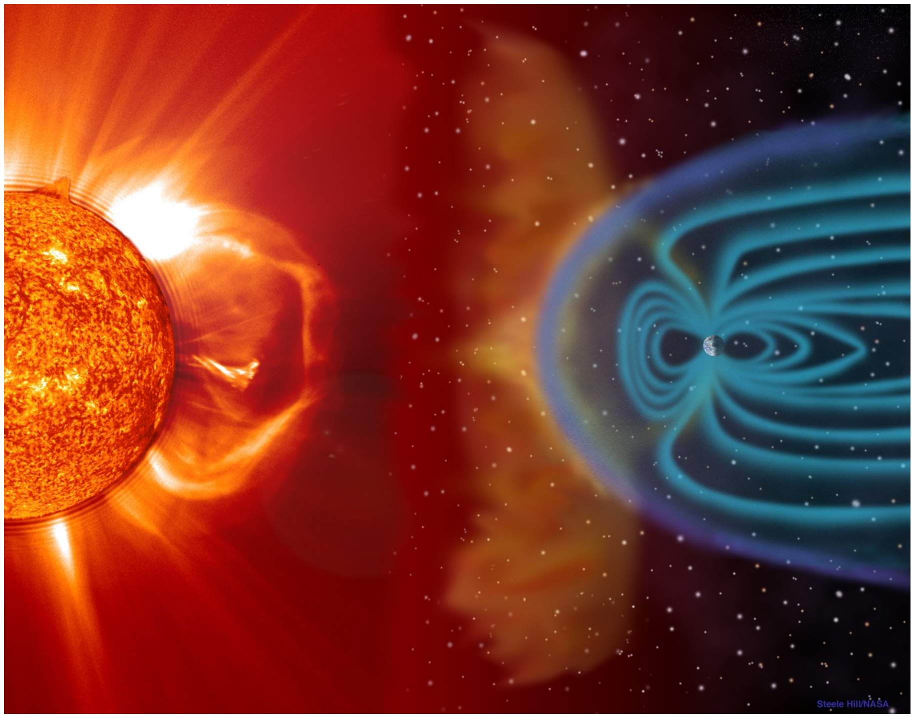

Figure 1.1: The Sun, the Earth and its magnetosphere. Image courtesy NASA.

Cavities are thought to be the precursors of CMEs (Gibson and Low, 1998) and are clues to the magnetohydrodynamic equilibrium states of the corona just prior to a CME (Fuller *et al.*, 2008). The fundamental physics as to how cavities form and disappear is still not fully understood. How a cavity can trigger a filament eruption and CME is still uncertain. Moreover, how cavities vary with the solar cycle has not yet been studied.

1.2 Coronal Cavity And The Associated Structures

Coronal cavities are highly visible, roughly elliptical shaped darkened regions observed above the solar limb in white light, X-ray, and extreme ultraviolet (EUV) coronal images. They are believed to be a region of low density relative to the surrounding corona (Gibson *et al.*, 2010) seen in Figure 1.3. Cavities often surround a prominence and are embedded in helmet streamer (Engvold (1989), see an example in Figure 1.4). Helmet streamers are bright

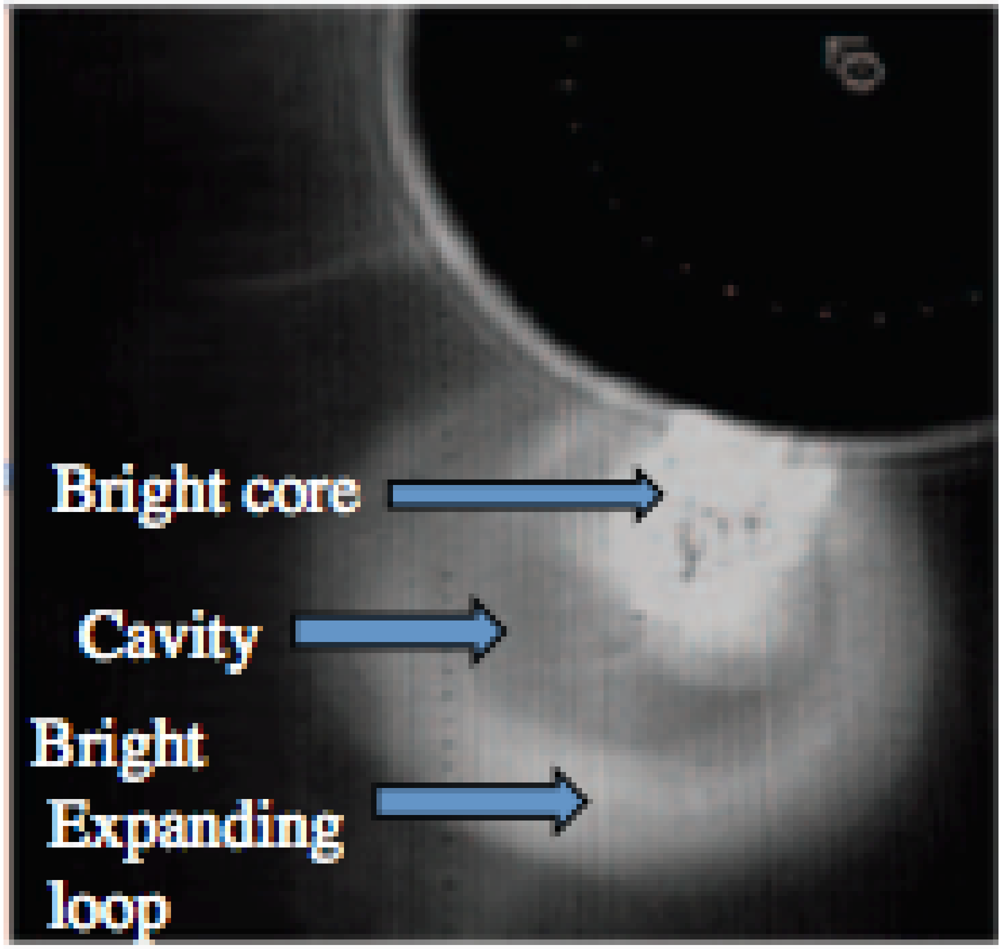

Figure 1.2: 3-D morphology of the CME seen in white light. Figure adapted from Illing and Hundhausen (1986).

structures with long pointed peaks associated with the closed magnetic loops surrounded by the oppositely directed open field lines extended outward into the interplanetary space. In coronagraph observations, a cavity often surrounds the prominence both prior to eruptions and as a part of outgoing CMEs (Gibson *et al.*, 2006). Filaments when seen at the solar limb are referred as *prominences*, and when they are viewed against the solar disk, they are referred as *filaments* (Gibson and Fan, 2006), here I will use both names interchangeably. A prominence always overlies a magnetic neutral line (Babcock and Babcock, 1955). Cavities

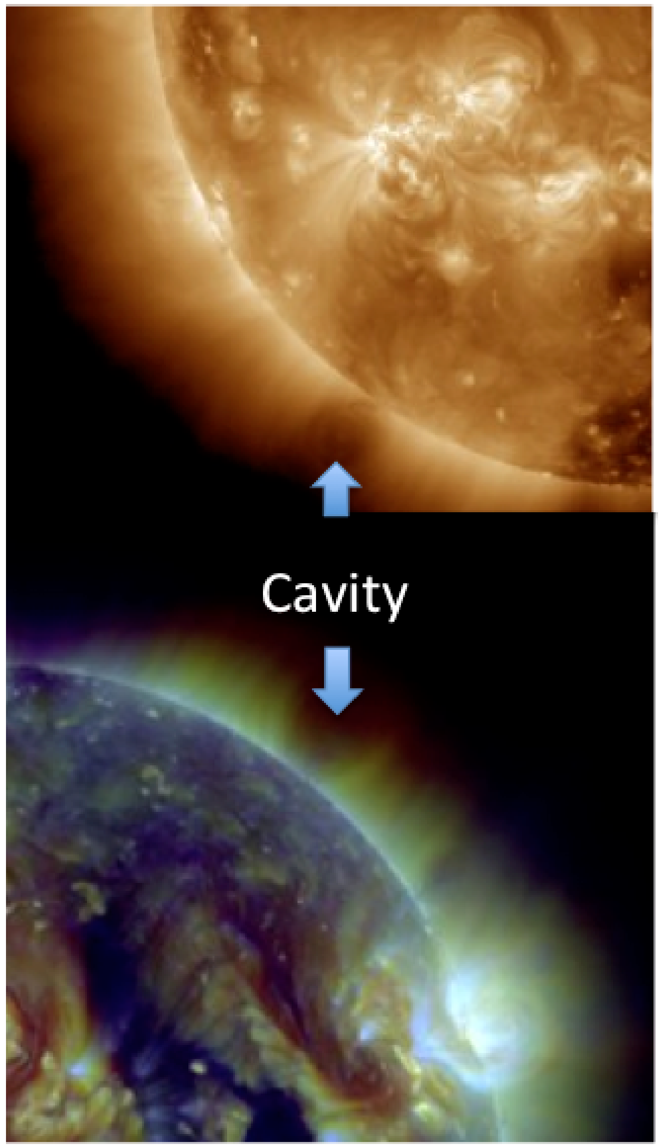

Figure 1.3: Off-limb close-up of a cavity, top 193 Å pass bands, and bottom composite image (211 Å 193 Å and 171 Å pass bands).

are the primary focus, but throughout this thesis I will repeatedly go into the details of prominence physics. The reason for this is related to the nature of the connection between both structures. Prominences are two orders of magnitude cooler and denser than the surrounding coronal atmosphere in which they are suspended (Gibson and Fan, 2006). The structure of a cavity will change very slowly with time until it, in many cases, eventually

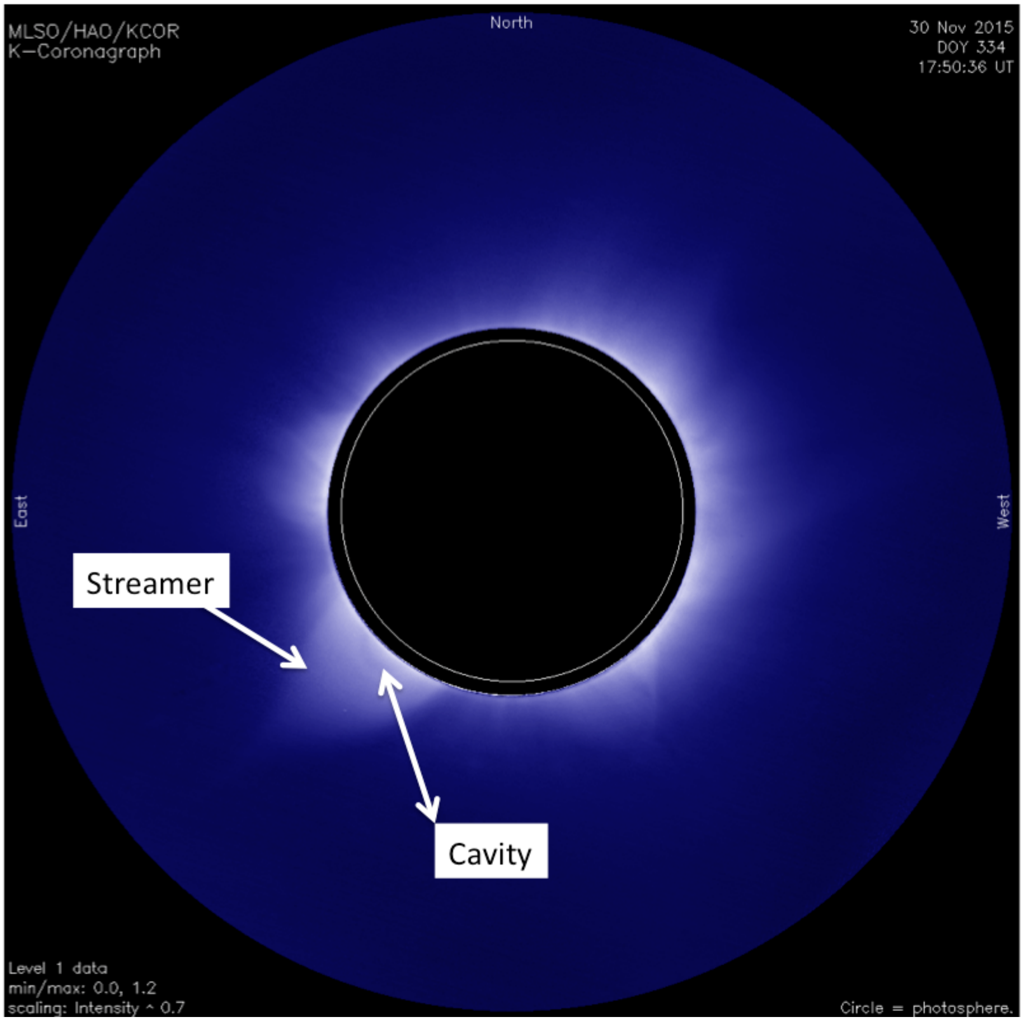

Figure 1.4: Cavity embedded in helmet streamer observed in K-COR/MLSO.

erupts as part of a CME (Gibson *et al.*, 2006; Marqué, 2004; Régnier, Walsh, and Alexander, 2011). A cavity can re-form after the CME eruption (Gibson *et al.* (2010), see an example in Chapter 4). Specifying the properties of cavities from formation to disruption will help us understand the CME's structure before it erupts and may also help understand the solar dynamo.

Cavities come in a range of sizes and shapes, from smaller ones associated with active regions to those associated with large-scale, longitudinally extended polar crown filaments

(Fuller *et al.*, 2008). Cavities are regions of locally enhanced magnetic field where the magnetic pressure balances the gas pressure keeping cavities from inward collapse (Low, 1980). More then two-thirds (2/3) of all CMEs originate from filament eruptions (Gopalswamy *et al.*, 2003; St. Cyr and Webb, 1991). Sometimes, even after an eruption, prominence and cavity remnants often remain or reform (Gibson and Fan, 2006). One concept is that the CME is driven by the magnetic flux rope (group of twisted magnetic fields rotating around a common axis) pushing its way out of the corona, lifting the mass in the leading front (the high-density region surrounding the cavity flux rope) and stretching the embedded, closed bipolar fields of the front (Low, 2001).

Cavities are an important part of the coronal magnetic field. The nature of their magnetic field and how it forms and evolves is not well understood. However, it is well known that cavities are present in the pre-eruption phase of the solar corona and sometimes erupt as a part of CMEs. The goals of this thesis is to make a cavity catalog and to study cavity characteristics along with magnetic field data and address several important scientific questions in solar physics. (1) What is the 3-D structure of coronal cavities? (2) Can cavities act as probes of the magnetic field reversal? (3) How are cavities formed and what determines their stability?

1.2.1 A Brief History Of Coronal Cavities

Saito and Tandberg-Hanssen (1973) traced back the observation of cavities to the eclipse of 29 June 1927, when Balanovsky and Perepelkin (1928) first noticed the reduced brightness surrounding a prominence and described it as an arch systems lying above the quiescent prominence (Figure 1.5). However, at that time "cavity" word was not introduced. The arch system surrounding the prominence drew the attention of many eclipse observers (Kawaguchi, 1967; Leroy and Servajean, 1966; von Klüber, 1961). von Klüber (1961) observed a dome formation on a plate of the 29 June 1927 eclipse (the same eclipse studied by Balanovsky and Perepelkin (1928)). He used the word dome formation rather than arch and

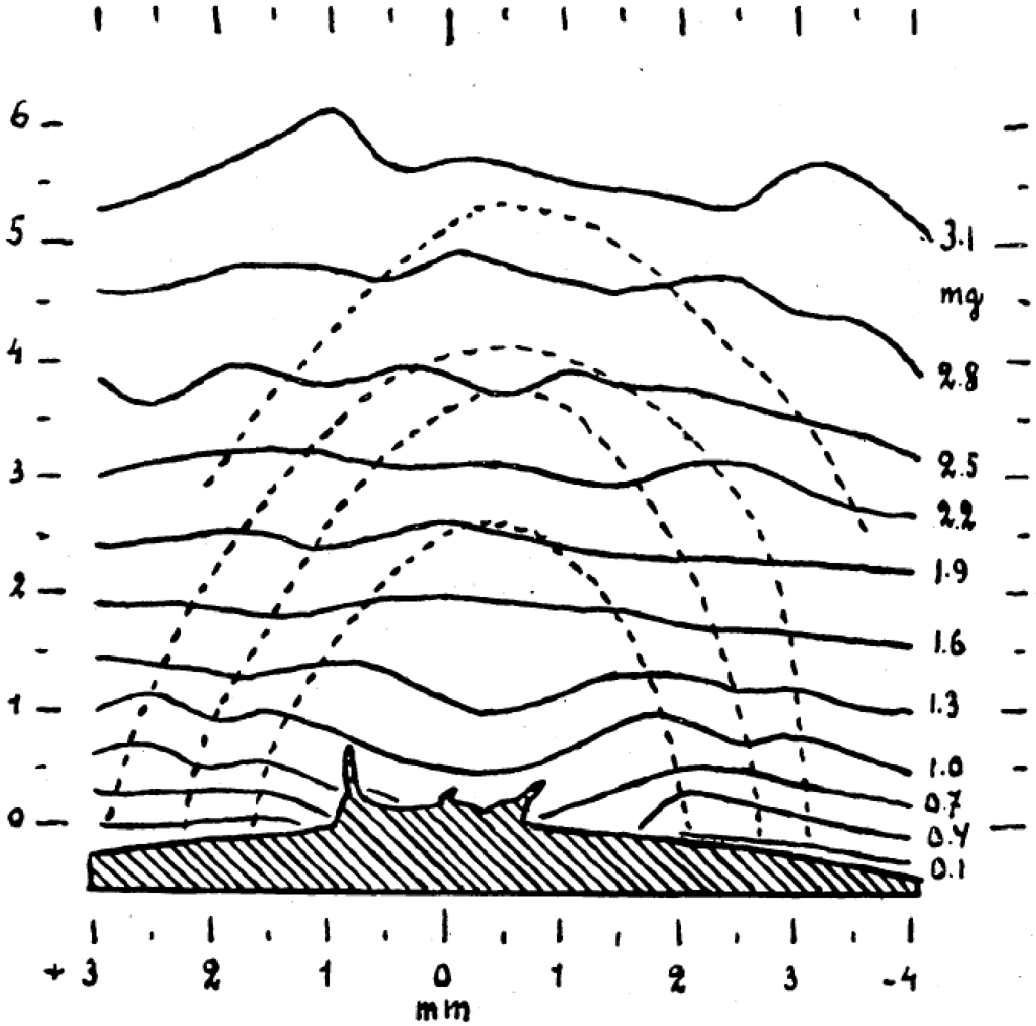

Figure 1.5: Isophate of eclipse observation from June 29, 1927. The dashed lines are the arc formation around the prominence. The solid horizontal lines are the distribution of brightness within the corona units in mg. The size of the plate is 7 by 7 mm. Figure adapted from Balanovsky and Perepelkin (1928).

also used the word dome-like cavities, implying hollow spaces and confirmed that the dark region surrounding the prominence is electron deficient. Later, Saito and Tandberg-Hanssen (1973) observed the eclipse of 4 February 1962 and saw a prominence with multiple overlying arches. They introduced the term cavity to describe the electron-deficient region between the innermost arch and the prominence. Since then cavity has been the accepted term for the dark region. Cavities were later observed in images at a variety of wavelengths : radio (Marqué, 2004; Marqué, Lantos, and Delaboudinière, 2002), soft X-ray and EUV(Heinzel *et al.*, 2008; Hudson and Schwenn, 2000; Hudson *et al.*, 1999; Reeves *et al.*, 2012; Sterling and Moore, 2004; Wang and Stenborg, 2010).

1.2.2 Prominence

Prominences have a temperature around 10^4 K but are surrounded by the 1 MK corona. The prominence formation process is defined by two components: a) A magnetic structure that supports the cool dense plasma in the filament and the cavity; b) A mechanism that fills the magnetic structure with cool dense plasma (Parenti, 2014). Prominences always appear above a polarity inversion line. These properties of prominences provide us insight into how the cavities form. In the absence of magnetic support, this situation is Raleigh-Taylor unstable as the high density plasma in the prominence is suspended against gravity over a low density plasma region.

Filaments typically consist of three components: spine, barbs, and two extreme ends. A spine runs horizontally along the top of the filament and is defined as the upper main body, barbs protrude from the sides of the filament down into the chromosphere and photosphere. The ends of a filament also described as "legs" that bend down towards the photosphere (Lin, Martin, and Engvold, 2008). Figure 1.6 is an example showing the three components of a filament observed with the Big Bear Solar Observatory in H-alpha filter on 25 September 2014 20:06:59 UT. The blue arrow and the red circles shows the filament spine and the barbs. The two red arrows show the two ends of the filament.

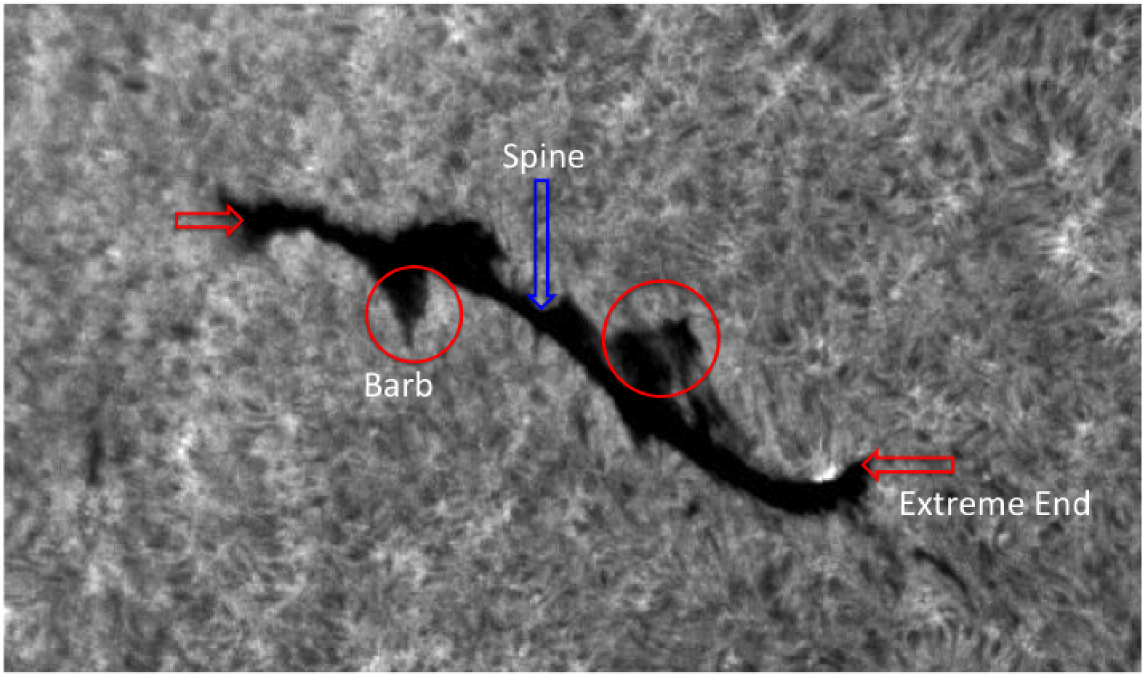

Figure 1.6: A filament observed in the Northern hemisphere with Big Bear Solar Observatory in H-alpha filter on 25 September 2014 20:06:59 UT. The red circles marks the barbs, blue arrow marks the filament spine and the two red arrow shows the two extreme ends of the filament.

1.2.3 Previous Work On Cavities (Geometric Structure, Density and Temperature)

Geometric structure

Various models have been used to characterize the 3-D structure of coronal cavities. Fuller *et al.* (2008) modeled the coronal cavity as a torus that partially encircles the Sun at constant latitude. Gibson *et al.* (2010) defined a global coronal streamer model, which includes a tunnel-like cavity with an elliptical cross-section with Gaussian variation of height along the tunnel length i.e the bottom of the ellipse remains at fixed radial height while the top part varied along the length of the cavity tunnel. Reeves *et al.* (2012) modified the Gibson *et al.* (2010) model by adding a bright core in the cavity center to better fit an observed cavity.

Low and Hundhausen (1995) proposed that the cavities are the fundamental hydromagnetic structure in both the CME and the helmet-streamer before an eruption. Low (1997) suggested that cavities are formed by the slow magnetic flux transport from the photosphere into the corona in the form of a magnetic flux rope. Hudson *et al.* (1999) provided observations of a long-lived cavity with soft X-ray emission, which they interpreted as a flux rope partially embedded in the photosphere. They observed a bright region (core) around the prominence. The core has a higher temperature than the cavity surrounding it. Fan and Gibson (2006) proposed that "bright cores" in a filament channel indicates the presence of a boundary layer or current sheet separating the helical field of a twisted flux rope in a stable confinement (prominence) from the surrounding untwisted fields. All these studies have provided information about the cavity structure.

Density

Many works had been carried out to measure the density of the cavity. The early analysis of eclipse data drew the conclusion that the cavity is a region of reduced electron density (Waldmeier, 1941). Leroy and Servajean (1966) took color photographs of the Sun during the total eclipse of 30 May 1966. They measured the intensity of the immediate neighborhood (3000 km) of the prominence and measured a brightness decrease about 5% lower in the immediate neighborhood. Saito and Hyder (1968); Saito and Tandberg-Hanssen (1973) used eclipse observation data to estimate that the density depletion was 8% or higher. Straka, Papagiannis, and Kogut (1975) used radio data and estimated the depletion was 50%, while Kundu *et al.* (1978) estimated the depletion ranged from 20−30%. Marqué (2004) using radio observation estimates the density depletion in the cavity is 25−50%.

Fuller *et al.* (2008) modeled the coronal cavity as a density-depleted torus encircling the Sun at constant latitude. They fit the model with the data from the Mauna Loa Solar Observatory (MLSO) MK4 chronograph. They concluded that the cavity density is depleted by a maximum of 40% compared to the surrounding streamers and also concluded that the cavity temperature was around 2 MK derived from the assumption of hydrostatic equilibrium. Fuller and Gibson (2009) studied 24 cavities making minor modifications to the methods of Fuller *et al.* (2008) in order to improve the accuracy and versatility and found that the cavity has larger density depletion at low altitudes than it does at high altitudes. At an altitude of 1.2 $R_\odot$, cavities mean depletion was 28% relative to their surrounding streamers.

Vásquez, Frazin, and Kamalabadi (2009) provided three-dimensional (3D) tomographic analyses of EUV images from the STEREO spacecraft and derived differential emission measures (DEM) of cavities and streamers. They concluded that the density inside cavities was 30% less than the streamers. Régnier, Walsh, and Alexander (2011) defined a cavity as a density depleted region sitting above the filament, indicating the existence of a magnetohydrostatic equilibrium. The filament material and plasma in the cavity volume drains down by gravity and sustained by the upwardly-directed magnetic field curvature force. Schmit and Gibson (2011) constrain the density model of a coronal cavity and its surrounding streamer using a forward modeling approach. They compared Hinode/EIS and MK4 data to their model. The best-fit isothermal model determines a cavity density of 1.95×10^8 cm^{-3} and a streamer density of 2.85×10^8 cm^{-3}. The depletion of this cavity was around 32% at 1.08 solar radii.

From previous analyses, we can see that the cavity density depletion varies from 5% to 50%, which is a huge difference. So, still the question remains "what is the actual density of a cavity?"

Temperature

There are several studies of the thermal properties of cavities. Fuller *et al.* (2008) measured the temperature to be around 2 MK based on the assumption of hydrostatic equilibrium. Vásquez, Frazin, and Kamalabadi (2009) concluded that the peak of the DEM that was around 2 MK is most likely to be the temperature of the prominence cavity. Habbal *et al.* (2010) combined white light and the EUV emission from four iron lines (Fe X, Fe XI, Fe XIII, and Fe XIV, temperatures from 0.9 to 2 MK) and concluded that most cavity temperatures are 2 MK or higher. They proposed two main outcomes (1) prominence cavities are intricate magnetic-density structures, with (2) temperatures characteristic, for the most part, of 2 MK plasmas or even higher. Since the hottest spectral line observed was Fe XIV only a lower limit could be placed on the cavity temperatures.

Reeves *et al.* (2012) used XRT filter ratios to estimate the temperatures of three observed cavities and found that the core temperatures were 1.75 MK, 1.7 MK, and 2.0 MK, which is hotter than the surrounding plasma. Kucera *et al.* (2012) used iron lines ratio from Hinode/EIS to constrain the cavity and streamer temperatures and concluded that both the streamer and cavity have temperatures in the range of $1.4 - 1.7$ MK. Guhathakurta *et al.* (1992) studied the temperature and density within large-scale structures of the inner corona during total solar eclipse of 1988 March 17/18. They concluded that cavities may be cooler than their surrounding streamer.

With all these previous analysis, it is difficult to derive the higher and lower limit of cavity temperature. "Is cavity hotter or colder than surrounding streamer" remains an open question. More work must be done to understand the thermodynamics of coronal cavities.

1.2.4 Formation Mechanism Of Cavity And/Or Prominence Magnetic Structure

There is still an ongoing debate regarding the structure of the cavity. Is it a flux rope structure or a sheared arcade? In this section we will describe formation mechanisms of both structures and later in detail, we describe different flux rope models of cavities.

Sheared Arcade

A sheared arcade is formed by the shearing motions of the photospheric footpoints close to the polarity inversion line (PIL, Antiochos, Dahlburg, and Klimchuk (1994); Aulanier, DeVore, and Antiochos (2002); DeVore and Antiochos (2000)). The formation mechanism start when bipoles embedded in a large background dipolar field starts moving parallel to the polarity inversion line due to the shear caused by the motion of the flux tube (bundle of magnetic field lines) footpoints or differential rotation. The footpoints move to new positions that have weaker field strength and are far from the dipole source whereas the midpoint remains in a region of strong magnetic field. Shearing causes a force-free flux tube to expand upward where the expansion varies along the length of the tube. More expansion will be at the footpoints compared to the midpoint consequently producing a dip near in the middle (Antiochos, Dahlburg, and Klimchuk (1994) and reference therein). In the Figure 1.7 (a) red field lines are sheared field lines that carry plasma. Figure 1.7 (b) shows the distribution of normal polarity (red) and inverse polarity (dark blue) magnetic dips. In both overlying green potential field has normal polarity.

Flux Rope

Cavities are generally accepted as the flux rope like structures. Flux ropes are formed either in the corona or emerge bodily from below the photosphere. We will describe the formation mechanism of flux ropes in the corona. van Ballegooijen and Martens (1989) presented a model in which flux cancellation at the neutral line of the sheared magnetic field leads to the formation of helical field lines. These field lines support prominence plasma. The process happens in two steps: 1) Shearing of coronal arcade followed by 2) Reconnection driven by photospheric flux cancellation. The magnetic structure is found to be stable. If flux cancellation continues, it can lead to an eruption. Figure 1.8 shows the flux cancellation process in a sheared magnetic field.

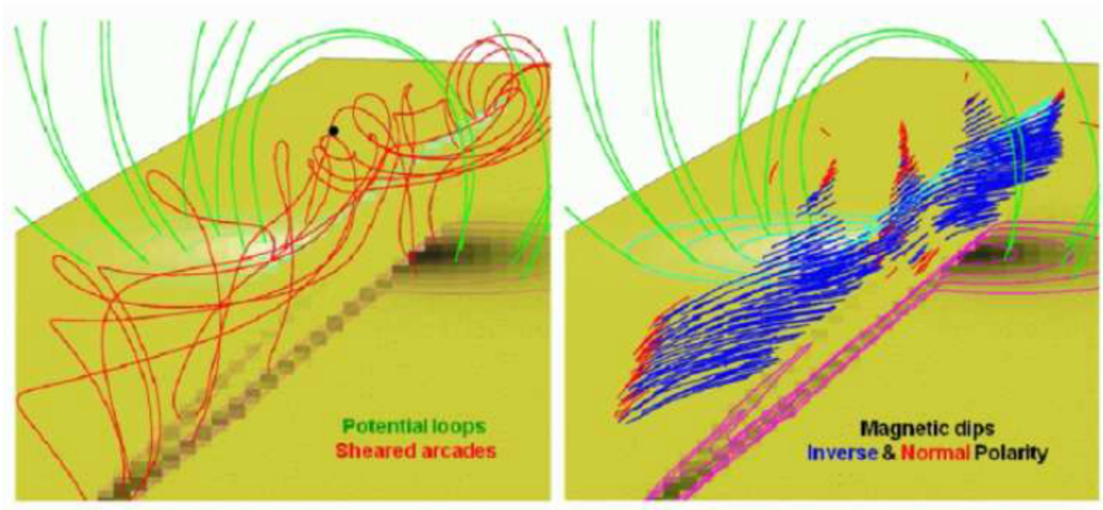

Figure 1.7: Diagram showing sheared arcade model for magnetic field in a filament channel: (a) Red field lines are the sheared field lines and green lines are the overlying potential loops. (b) Shows the distribution of field lines. Red has normal polarity and dark blue has inverse polarity magnetic dips. Figure adapted from Mackay *et al.* (2010).

Modeling Cavity As A Flux Rope

It is now generally accepted by the community that cavities are flux-rope-like structures. The relation between the three-part structure of a CME and the CME eruption has been described in the twisted flux rope topology variation. Some authors describe the prominence alone as the flux rope (Amari *et al.*, 1999; Aulanier and Demoulin, 1998; Priest, Hood, and Anzer, 1989; Rust and Kumar, 1994). While other analysis describe the entire three-part structure to the flux rope (Chen, 1996; Gibson and Low, 1998; Guo and Wu, 1998; Low and Hundhausen, 1995). The prominence and cavity are assumed to be parts of the same magnetic structure, while the streamer shows the outer boundary of the magnetic flux rope model (Gibson and Fan, 2006).

Two of the flux rope models proposed to explain the magnetic feature of cavity are:

Cylindrical Flux Rope

Fan and Gibson (2006) described a 2.5D axisymmetric isothermal cylindrical flux rope model

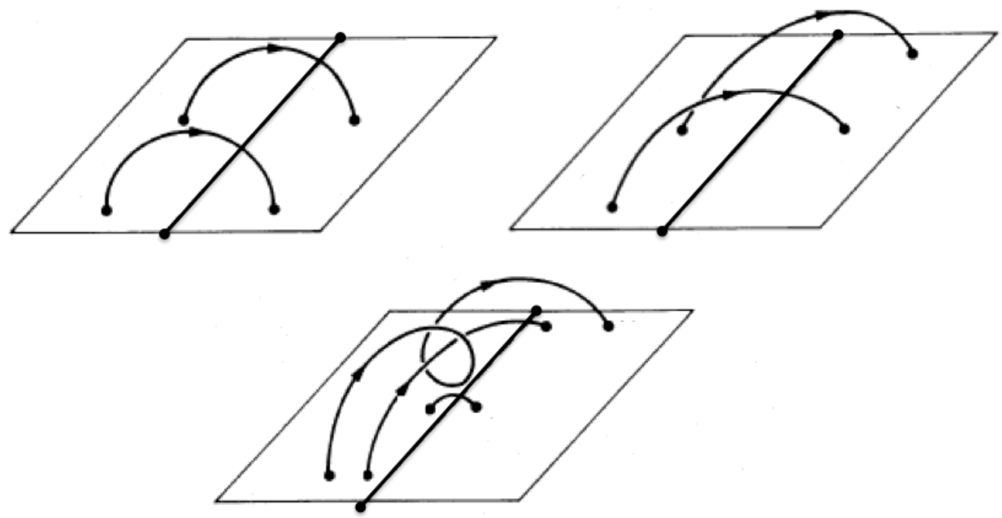

Figure 1.8: A schematic of a flux cancellation filament model. The flux cancellation happens in a sheared magnetic field. The rectangle represents the solar photosphere, and the solid line is the polarity inversion line separating two regions of opposite magnetic polarity. Flux cancellation at the neutral line of the sheared magnetic field leads to the formation of helical field lines. Adapted from van Ballegooijen and Martens (1989).

for long filament channels. In this model, a twisted toroidal flux tube emerges from the lower boundary into the preexisting potential arcade field seen in Figure 1.9. During the quasi-static stage, a cavity and a central prominence are developed in the volume occupied by the flux rope. The flux rope expands due to its toroidal or axial magnetic field resulting in development of a cavity. With extreme twist there is a loss of equilibrium which causes the expulsion of the flux rope (Fan and Gibson, 2006; Rachmeler *et al.*, 2013).

Spheromak Flux Rope Model

The spheromak magnetic flux rope model is based on a solution to the MHD equations in full magnetostatic equilibrium Gibson and Low (1998). This model explains that the cavity arises from strong internal magnetic pressure and twisted field lines winding about

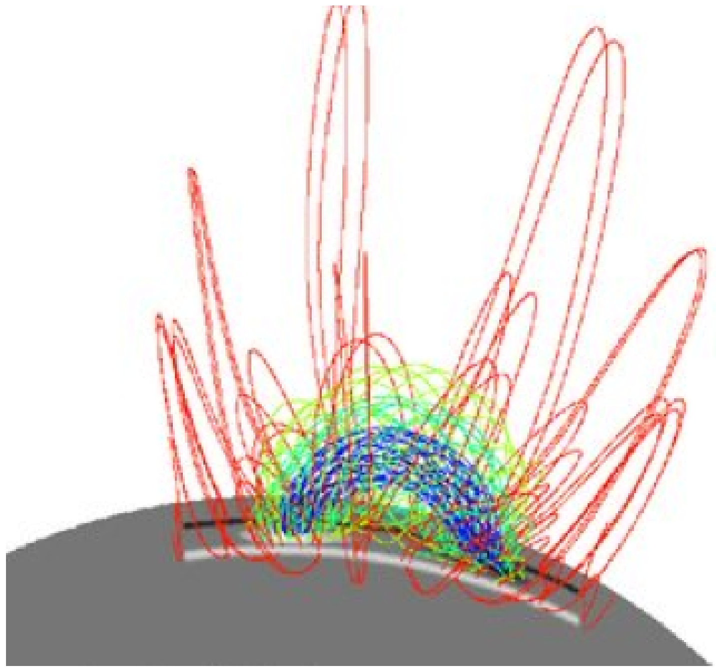

Figure 1.9: Cylindrical flux rope model. Adapted from (Fan, 2010).

an axial field line that is partially detached from the photosphere (Low, 1996), and the prominence is supported in the dips of the magnetic field, and the front or helmet streamer is the interface between the flux rope system and surrounding, more simply sheared arcade field (Low, 1996; Low and Hundhausen, 1995).

A spheromak is a toroidal rope of twisted flux encircling the axis of symmetry as seen in Figure 1.10. Spheromak magnetic topology describes the magnetic properties of both quiescent prominences and their cavities.

1.2.5 Plasma Filling Mechanism Of Cavity And/Or Prominence Magnetic Structure

Throughout the discussion in the previous section, we describe the structure that allows a cavity and prominence to exist in the corona. We have not discussed where the prominence mass comes from and why cavity has low mass. It is important to understand how the cavity-filament mass is formed. The physical processes by which cavity and prominence

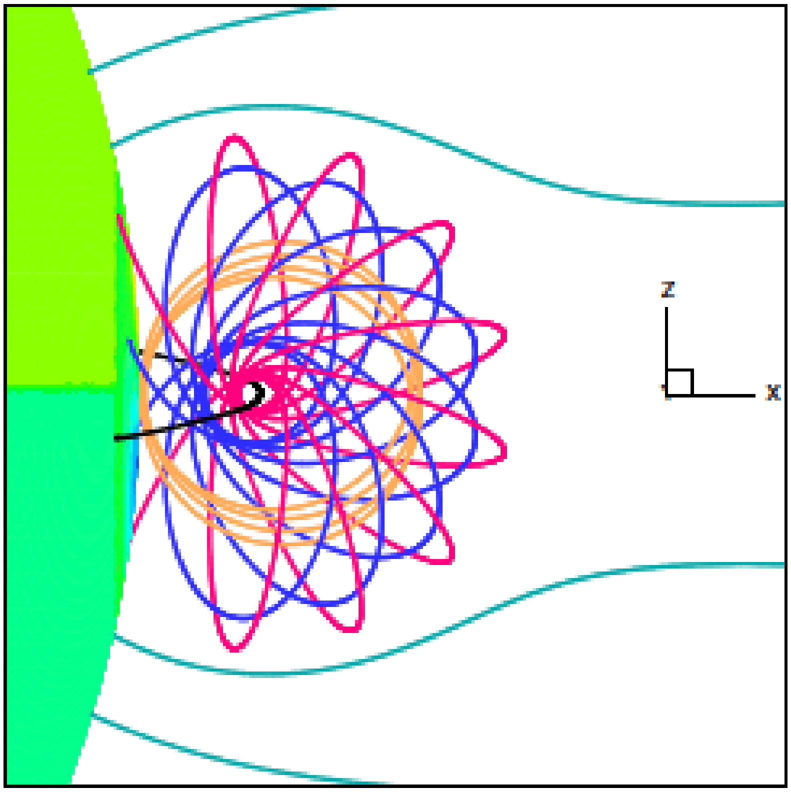

Figure 1.10: GibsonLow spheromak magnetic flux rope model. Red, purple, orange and black field lines traces the model. The view is along the rope axis. Black thick line traces the flux rope axis in the dips of magnetic field and prominence material sits below it. Adapted from Dove *et al.* (2011).

plasma forms and evolves still remain unclear. However, it is clearly understood that the large prominence mass must come from the chromosphere as corona does not have enough plasma. There are many models explaining the transport of chromospheric plasma into the corona. Throughout most of the models, the cavity has been a neglected constraint on prominence structure. While only a few models account physical process for both cavity and prominence. In this section, we will discuss four main types of mass formation models (Karpen (2015); Mackay *et al.* (2010) and references therein).

Injection Model

According to this model, reconnection low in the solar atmosphere drives chromospheric plasma into pre-existing filament-channel flux tubes due to reconnection low in the solar atmosphere (Chae *et al.*, 2001; Wang, 1999) seen in Figure 1.11. Some injection models suggest the PIL as the reconnection sites (e.g., Chae (2003)), while others propose that the jets originate at minority-polarity intrusions offset from the PIL (e.g., Wang (1999)). This model only accounts for prominence mass formation.

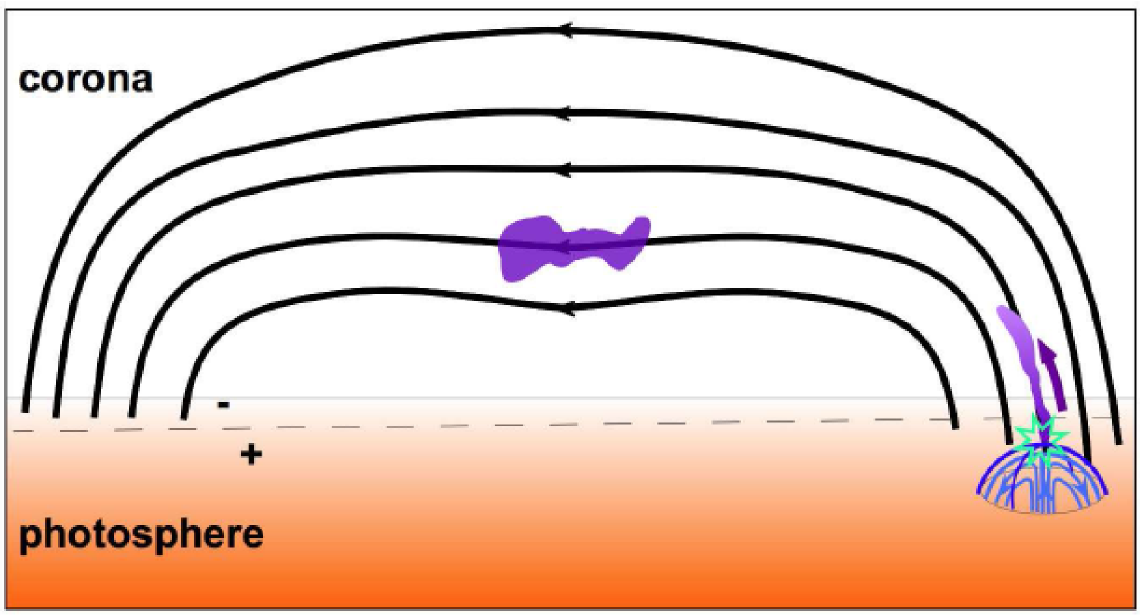

Figure 1.11: Injection Model. Purple color represents the prominence plasma which is formed by the reconnection shown by blue lines. Black lines are the persisting filaments channel field and the dashed line is the polarity inversion line. Adapted from Mackay *et al.* (2010).

Levitation Model

According to this model, the cool plasma is lifted at the PIL and transported transverse to the magnetic field (see Figure 1.12) either by flux rope (concave up) emergence (see, e.g., Lites (2005); López Ariste *et al.* (2006)) or by photospheric or chromospheric reconnection associated with flux cancellation (Litvinenko and Wheatland, 2005; Priest, van Ballegooijen, and Mackay, 1996; van Ballegooijen and Martens, 1989) seen in Figure 1.12. This model only explain about the prominence formation mass.

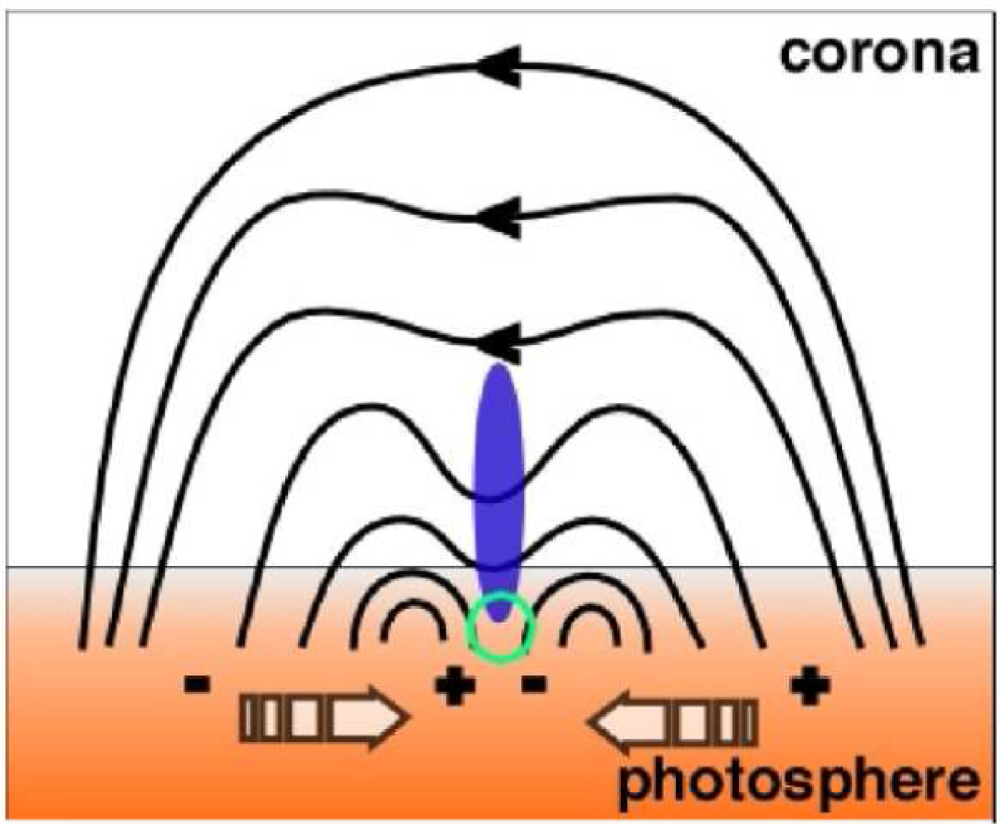

Figure 1.12: Levitation model. Prominence plasma represented by purple color is lifted by U-loop emergence or post reconnection relaxation associated with flux cancellation. Adapted from Mackay *et al.* (2010).

Evaporation-Condensation Model

This model accounts for both cavity and prominence formation. According to the evaporation-condensation model, the chromospheric material is evaporated into the corona by localized heating above the footpoints and condenses to form a cool filament (Antiochos and Klimchuk (1991); Karpen and Antiochos (2008); Poland and Mariska (1986) and references therein) as shown in Figure 1.13. The model is based on the fact that adding heat to a coronal loop increases the density of the corona and slightly decreases the chromospheric mass (Mackay *et al.*, 2010).

According to Xia *et al.* (2014), thermally and gravitationally stratified magnetic flux ropes condense *in situ* due to radiative losses, to form prominence and cavity. The cavity forms simultaneously with the prominence formation. The formation of the cavity starts with the cooling of the dense flux rope region and as the mass of the flux rope continues to drain out, the cavity regains its temperature above a million Kelvin while dropping its density below the density of the surrounding coronal arcade.

Magneto-Thermal Convection

The magneto-thermal convection model introduced by Berger *et al.* (2011) starts with the emergence of twisted magnetic flux from the solar interior into the chromosphere beneath prominences and forming magnetic bubbles. Due to internal reconnection or Alfvén wave dissipation, the plasma contained inside bubbles gets heated, and buoyancy carries them to a prominence height in the corona. It undergoes Rayleigh-Taylor instabilities to form dark plumes carrying hot plasma and magnetic flux into overlying coronal cavities and cold prominence plasma drains back to the chromosphere (Karpen, 2015).

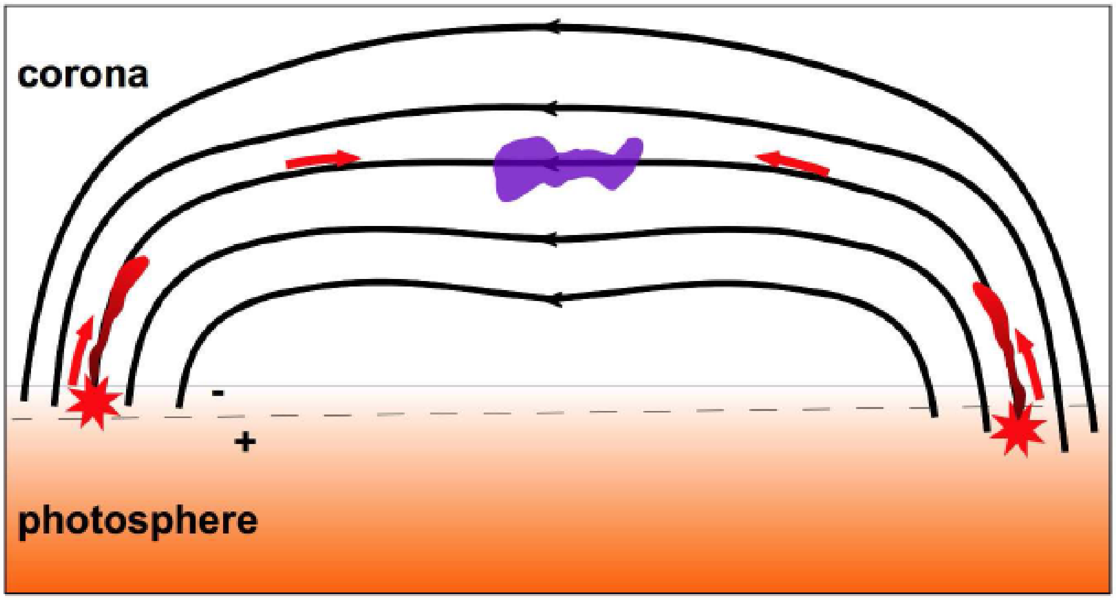

Figure 1.13: Evaporation-condensation model. Red material represents the hot chromospheric plasma flows driven by localized heating above the footpoint and later condenses in the corona as cool prominence material shown by purple color. Adapted from Mackay *et al.* (2010).

1.3 Topics Covered In This Thesis

1.3.1 Developing Limb-Synoptic-Map Method To Detect Cavity and Property Study

The identification and cataloging of cavities are important tasks that provide the basic knowledge for further scientific studies. Currently, one other catalog exists that identifies cavities observed with K-COR white light coronagraph and Coronal Multi-channel Polarimeter (CoMP) instruments on Mauna Loa Solar Observatory (MLSO) since 2014. K-COR observers look through the sequence of K-COR coronagraph and CoMP images report on events that have taken place on a daily basis. This is a preliminary catalog and provides the location of the cavity, K-COR movie, time, and additional comments on shapes, visibility and if prominence was observed or not. This information is currently online at http://mlso.hao.ucar.edu/mlso_event_table.php. However, the detailed measurements on the shape (length, width, and length), positions (latitude, longitude) are not provided.

To date, several cavity detection schemes have been described in the literature. The most common kind is making EUV or White light movies with high cadence data and then analyzing the movies to identify and characterize the cavities. Our method of cavity detection is unique. We first construct limb synoptic maps by concatenating strips of equal width from annuli of radiance above the solar limb from EUV snapshot images from the Atmospheric Imaging Assembly (AIA) instruments on board the Solar Dynamics Observatory (SDO), over a Carrington Rotation (CR) of 27.27 days. The eastern and western limb synoptic maps are constructed separately. The cavity appears as an elongated dark region in both AIA 193 Å and AIA 211 Å wavelength synoptic maps. We also examine AIA 304 Å maps. If a prominence exists at the same location in AIA 304 Å wavelength, we confirm that the dark region is indeed a cavity. In this way, we not only identify the cavity but also get information on the length and width of the cavity.

The advantage of using limb synoptic map is that the length information can be measured in both meters and days. We manually select the cavity border between the elongated dark region and the surrounding bright plasma. Length is measured as the sum of differential length in a spherical coordinate system (please see Chapter 2 and Appendix for detail). Height and width are measured using the snapshot images taken at the middle time frame of cavity's evolution. In order to quantitatively analyze cavities, we fitted the ellipse based on the cavity shape selected between the cavity's dark region and the surrounding bright plasma. We selected points along the edge of the cavity and fit an ellipse to these points. The height is measured as the maximum radial distance of the fit, whereas cavity‘s width is the maximum separation distance between the bounding colatitudes of the ellipse (please see Chapter 2 and Appendix B for details). In our method of fitting the ellipse, the bottom of the ellipse always lies above the solar limb.

We have produced the largest catalog of EUV coronal cavities (429 cavities between May 19, 2010 and Feb 1, 2015) and have made the catalog available for the public. For the first time the length of the cavity is included in the catalog. Each cavity is defined by its measured parameters. These include its starting and ending latitude and longitude, length, width, height, and tilt angle (for cavity list please see fig. 2.2). In Chapter 2, I give an example of one cavity showing how the catalog has helped supplement this thesis.

1.3.2 A Survey Of Coronal Cavity And Statistical Study

Only a few statistical surveys of cavities regarding magnetic structure, density, quantifying cavity morphology with intensity contrast properties focusing in relation to their eruption as CMEs are described in the literature. Gibson *et al.* (2006) made the largest comprehensive study of coronal white-light cavities from MK4 Coronograph, in operation since 1998 November, in order to gain information about the state of the corona prior to CMEs. Twenty-five best cavities were observed from 1999 to 2004 in the Mk4 observations, and a detailed kinematic study was done using observations from Mk4, EUV Imaging Telescope (EIT), and Large Angle and Spectrometric Coronagraph Experiment (LASCO, both on board SOHO) launched in 1995. The studies showed that the evolution of cavities just prior to the CME showed some distinct feature like necking, the rising of associated filaments, and possibly a darkening cavity with a more sharply defined boundary. Fuller and Gibson (2009) made a density study of 24 cavities observed in MK4/MLSO. The density calculations from all 24 cases revealed that the cavity has a larger density depletion at low altitudes than it does at high altitudes. Moreover, they found that a cavity near solar maximum has greater range in density at 1.2 $R_{\odot}$ than solar minimum. However, they did not find any significant correlation between cavity density properties and cavity height.

Forland *et al.* (2013) conducted a survey of 129 cavities in 19 months of data from 01 June 2010 through 31 December 2011 using SDO/AIA images, creating a database that noted correlations between cavity shape aspect ratio and their eruption as CMEs. They fitted the ellipse in which the boundary is selected between the cavity dark region and the surrounding bright plasma. They concluded that the fitted ellipses were taller than they are wide for almost all cavities and on average eruptive cavities are narrow, high-centered, and high-bottomed. Bąk-Stęślicka *et al.* (2013) made a statistical survey of 68 cavities observed by SDO/AIA during 78 days between May 2011 and December 2012 to study the magnetic structure of cavities. They used CoMP observations to search for prominence-cavity signatures in linear polarization and found characteristic lagomorph structures in linear polarization as well as bulls-eye patterns in LOS velocity and concluded that such signatures are well-explained by a flux rope topology.

Our statistical study presented in Chapter 3 focuses on two major topics i) quantifying cavity morphology with length/evolution of cavities, and ii) studying the correlation between cavities and the solar cycle for the first time. The first part of our results showed that cavity's shape can be oblate, near circular or prolate, contradicting the results from Forland *et al.* (2013), who concluded that fitted ellipses are taller than they are wide for almost all cavities. The difference in the result is due to the interpretation of data (we will discuss in Chapter 3).

In the second part of the study, we found that cavities formed a belt in the classical butterfly diagram of sunspots; we called this the cavity belt. Results showed that the cavity belts migrated towards higher latitude with time and the cavity belt disappeared after the polar magnetic field reversal in both the hemispheres. We concluded that the polar crown cavity position can be used to establish the time of polar magnetic field reversal. This result shows that cavity evolution provides new insight into the evolution of the solar cycle.

1.3.3 How is a Circumpolar Cavity Formed?

In Chapter 4, we studied the formation of a long polar cavity that was observed in the southern hemisphere for more than a year. We examined in detail from March 21, 2013−October 25, 2013. During this eight month period, the cavity sometimes erupted and reformed within a few hours. Sometimes even after eruption the cavity was visible at the same location. Eruptions of the cavity as a CME were also observed. There were 19 eruptions during the eight months of data. We did not study the eruptions in details as our goal was to investigate how such a long lived cavity formed and what determined its stability. For this, we made HMI limb magnetic field synoptic maps by rotating data one week ahead or back depending on which limb was been analyzed (for details, please see Chapter 4).

Our observation suggests two necessary conditions to form long stable polar crown cavities: 1) The underlying polarity inversion line should be formed between the trailing part of a strong active region which has been diffused or decayed for a long time and the unipolar magnetic field (polar coronal hole). There is ongoing flux cancelation between trailing flux of multiple decayed active regions and the unipolar magnetic field. 2) The long lasting polar crown cavity is sustained by the flux from the multiple newly transported active regions. This type of study is being presented for the first time. We have created a new category called "Diffused bipole and polar coronal hole interaction region" in the Mackay, Gaizauskas, and Yeates (2008) classification that includes these features.

1.3.4 Comparing Models With Observations

In Chapter 5, we examine the magnetic structure of the cavities using data from CoMP/MLSO. The purpose was to validate which flux rope model best fits the observation. In Section 1.2.4 we have briefly described two existing flux rope models: the cylindrical flux rope model and the spheromak flux rope model. In CoMP linear polarization observations of cavities, "polarization ring" structures were not observed in any case study. However, an almost U-shaped structure is observed with a central dark core. Moreover, a bulls-eye pattern is seen in the LOS velocity. The signatures observed from CoMP data for three case studies are consistent with a flux rope topology, which supports the hypothesis that the cavities are flux rope structures.

1.4 Outline of Dissertation

Chapter 2 describes the innovative method to detect cavities and measure the 3-D structure (length, width and height) and thermal properties of cavities using a case study. Chapter 3 describes a statistical study of the largest number of cavities. This include correlations between the height, width and length of the cavities in Solar Cycle 24 and also the relation between the location of cavities with the solar cycle that follows the evolution of the solar magnetic field. Chapter 4 discusses the photospheric magnetic field evolution of a circumpolar crown cavity, that lasted for several Carrington Rotations. This is the first study of how cavity's underlying PIL formed. Chapter 5 describes the existing flux rope models and presents a study of a cavity using the cylindrical flux rope model. Chapter 6 contains a summary and future plans.

Chapter 2: Developing Limb-Synoptic-Map method to detect cavity and property study

2.1 Introduction

This chapter describes an unique technique to detect coronal cavities and how to measure the 3D geometrical structure using one long cavity as a case study. The cavity appeared during Carrington Rotation (CR) 2113 and spanned more than 170° of heliographic longitude. 3-D geometrical model of cavity based on observations has been created. The thermal and magnetic properties have also been investigated. For this study data was used from the *Atmospheric Imaging Assembly* (AIA) and *Helioseismic Magnetic Imager* (HMI) instruments on board the *Solar Dynamics Observatory* (SDO, Pesnell, Thompson, and Chamberlin (2012)). The chapter is organized as follows: In Section 2.2, data preparation and the method of limb synoptic maps is described. In Section 2.3, the three dimensional sizes (height, diameter and length); magnetic properties, temperatures and the reconstructed 3-D geometric structure of the cavity is presented. Section 2.4 has a discussion on what conclusions could be drawn from these observations.

2.2 Limb Synoptic Map Method and Observations

The AIA instrument on board SDO images the solar atmosphere through ten passbands almost simultaneously. It has a temporal cadence of 12 s, a spatial resolution of 1.2 arc second, and a field of view of 2.6 $R_\odot$ (Lemen *et al.*, 2012). In order to determine in which wavelength cavity visibility is high, we examined observations from seven passbands: 304 Å (He II), 171 Å (Fe IX), 193 Å (Fe XII, XXIV), 211 Å (Fe XIV), 335 Å (Fe XVI), 94 Å (Fe XVIII), and 131 Å (Fe VIII, XX, XXIII). We found that the cavity was most visible in AIA 193 Å and AIA 211 Å as shown for a cavity observed on 14 August 2011 in Figure 2.1. The cavity's depleted center, boundary, and the outer bright streamer were clearly defined in these two passbands. The AIA 304 Å line was used to study the prominence associated with the cavity and AIA 171 Å was used as it showed the best fine structure of loops and prominence features as well.

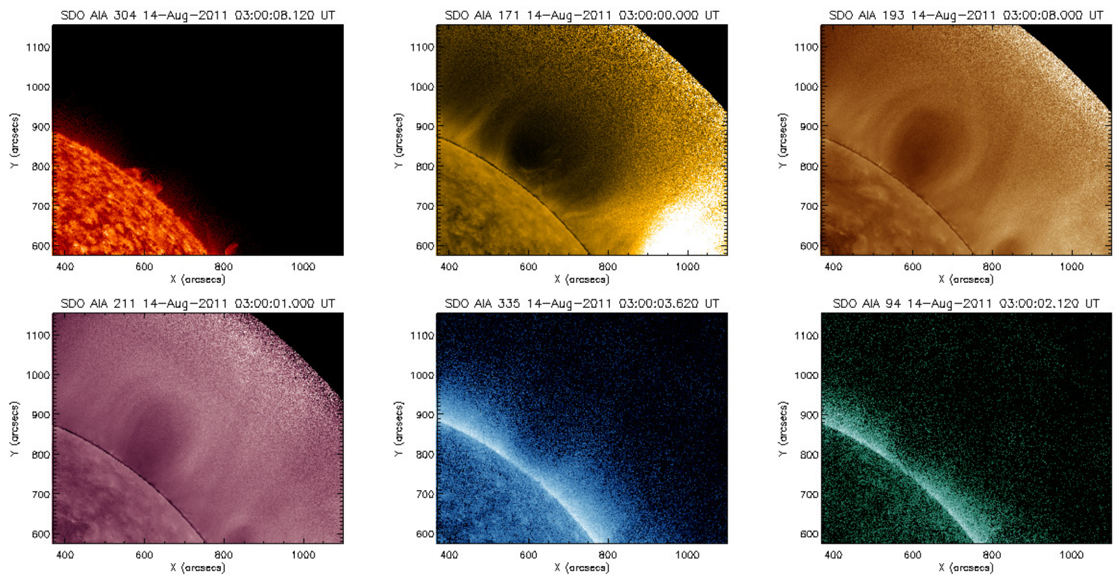

Figure 2.1: Snapshot images of cavity C211347177N as seen on the western limb on 14 August 2011. The images are taken in six wavelengths of 304 Å, 171 Å, 193 Å, 211 Å, 335 Å, and 94 Å.

In AIA 193 Å (third column, first row) and 211 Å (first column, second row) in Figure 2.1, the prominence (or filament when seen on the disk) appears as a thread-like structure connecting the solar surface to the cavity. In the movie, we can see the formation of the cavity and also its disruption at the time of prominence eruption in both AIA 193 Å and 211 Å. The prominence associated with the cavity is best seen in AIA 304 Å (first column, first row). In 171 Å (second column, first row), complex prominence motion along with the lower half of the cavity can be viewed. In AIA 335 Å (second column, second row) and

AIA 94 Å (third column, second row), the cavity is only seen as half dark circular feature.

While observing coronal cavities above the limb, one inherent problem is that coronal cavities are an extended structure, and are not localized in the plane of the sky. Thus, the line-of-sight integration effect is significant. One can not determine the true linear size of cavities along the longitudinal direction in individual coronal images. Moreover, because a cavity can't be observed against the disk, we will use a series of limb observations to visualize the cavity structure over its life time.

In order to determine the 3-D structure of cavities, we developed a Limb Synoptic Map similar to that shown in Figure 8 of Gibson *et al.* (2010). A limb synoptic map is constructed by concatenating strips of equal width from annuli of radiance above the solar limb from snapshot images over a Carrington Rotation (CR) of 27.27 days. The eastern and western limb synoptic maps are constructed separately. The eastern limb is defined from 0° to 180° and western limb from 180° to 360° in position angles in polar coordinates (starting from the North pole, position angle increases counterclockwise). First, the photon intensity of each passband is normalized by the exposure time. Half circular rings from eastern or western limb are extracted from 1.05 to 1.10 $R_\odot$ (1.02 $R_\odot$ to 1.07 for AIA 304 Å) above the solar disk and mapped to a rectangle whose long dimension is latitude and the short dimension is the Carrington longitude of the central meridian $+90°(-90°)$ for western(eastern) limb. After extraction, a radial-gradient filter is applied to the strips to remove the rapid decrease in radiance with increasing height and show details of solar corona at all heights. The 100-pixel strip is then narrowed down to six pixels and mapped by decreasing Carrington Longitude onto a rectangular grid, forming the limb synoptic map (Figure 2.2). We used 24 images per day, so that each synoptic map has 3600 pixels in longitude and 1080 pixels in latitude.

Identifying and Cataloging Cavities

It is relatively easy to identify a cavity in limb synoptic maps. The cavity appears as an elongated dark region in both AIA 193 Å and AIA 211 Å wavelength synoptic maps. We also examine AIA 304 Å maps. If a prominence exists at the same location in AIA

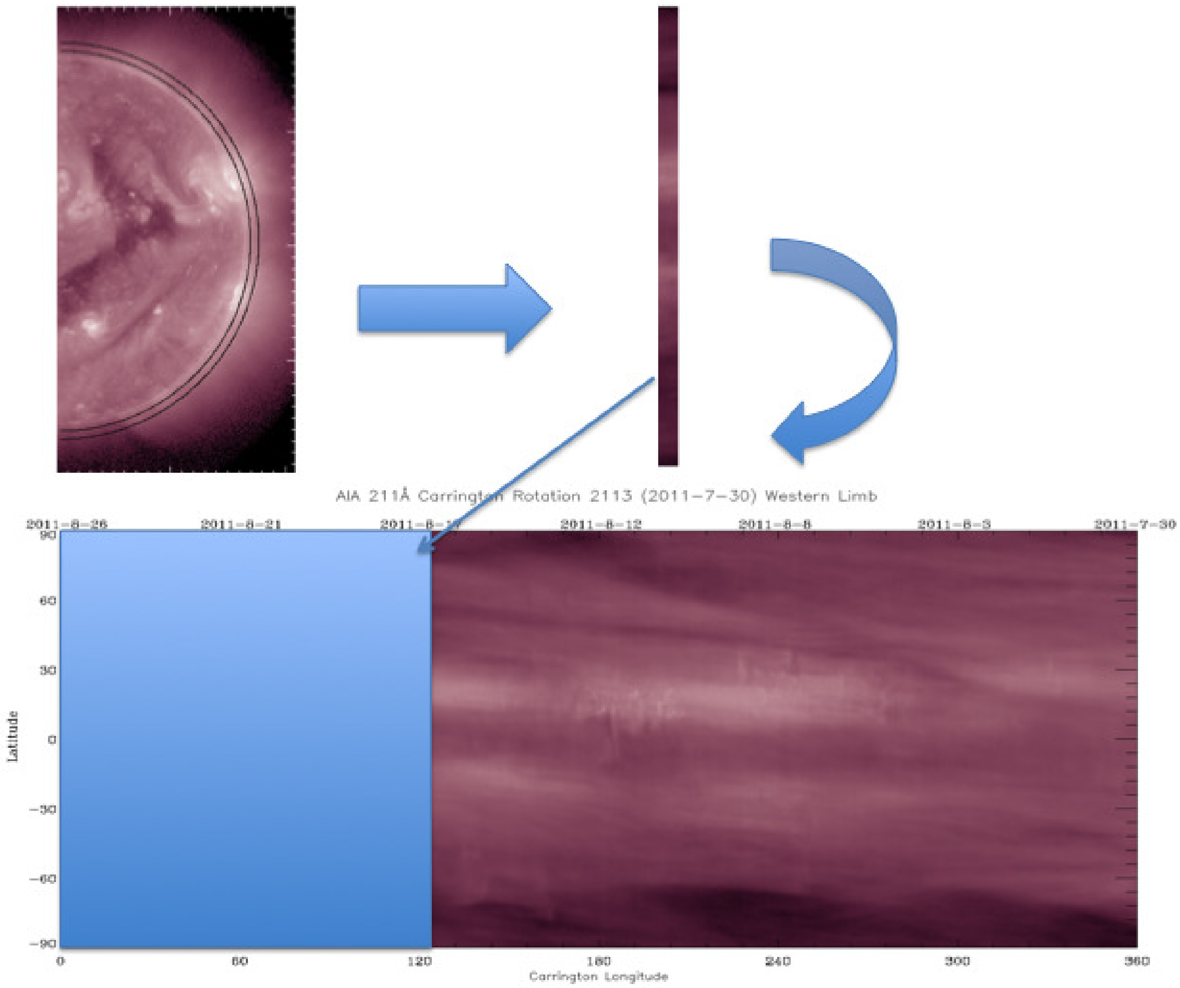

Figure 2.2: The limb synoptic method. Spherical limb half-annuli are transformed to Cartesian stripes and then mapped from right to left for 27.27 days to construct the synoptic map. The stripes are created from annuli spanning 1.05 to 1.10 $R_\odot$.

304 Å wavelength, we confirm that the dark region is indeed a cavity. The bright regions near the equator are active regions and the dark regions at the poles are polar coronal holes. In this way, we identified the polar crown cavity C211347177N appeared during CR 2113 at the northwestern limb of the solar disk (Figure 2.3). Cavity ID is created with a first letter C, followed by the CR number (four digits), average latitude (two digits) and average longitude (three digits), and the last letter N(S) stands for northern(southern)

hemisphere, respectively. This cavity was associated with an eruptive prominence. Cavity C211347177N was first visible on 05 August 2011 05:19 UT and attained its maximum height and maximum width on 14 August 2011 02:19 UT. Another cavity was also visible on the eastern limb on 11 August 2011 02:44 UT, six days after the first appearance of cavity C211347177N in the western limb. This eastern limb cavity might be a part of the same large structure (filament channel) as the prominence on the both limbs erupted at the same time on 17 August 2011 01:26 UT. Cavity C211347177N disappeared on 17 August 2011 22:19 UT, 21 hours after the prominence eruption, while the cavity in the eastern limb disappeared during the same prominence eruption.

2.3 Result

After identifying cavity C211347177N, we measured the three-dimensional geometric structure, thermal properties, and reconstructed the 3-D geometric structure based on these measurements. We used limb synoptic maps to calculate length and width, EUV snapshot images to measure height and thermal properties, and HMI central meridian synoptic map to examine the correlation between the cavity morphology and the underlying magnetic field distribution of the cavity. We describe methods and results below.

2.3.1 Length and Width Measurement

The detailed process of calculating the length of a cavity is described in appendix B.1. Here, we describe in summary. A cavity is assumed to be stable, or at least slowly-evolving in time, thus the change on the limb in time is caused by seeing different parts of the cavity along its length. The length and width of the cavity can be measured from the synoptic maps (Figure 2.3). The length is measured as the sum over the differential lengths along the path of the cavity. The width of the cavity is the distance between the bounding latitudes measured along a meridian (please see appendix B.2).

We have determined that the length of the cavity C211347177N was 1360 Mm as measured in the 193 Å passband. The cavity first appeared at 280° longitude and remained

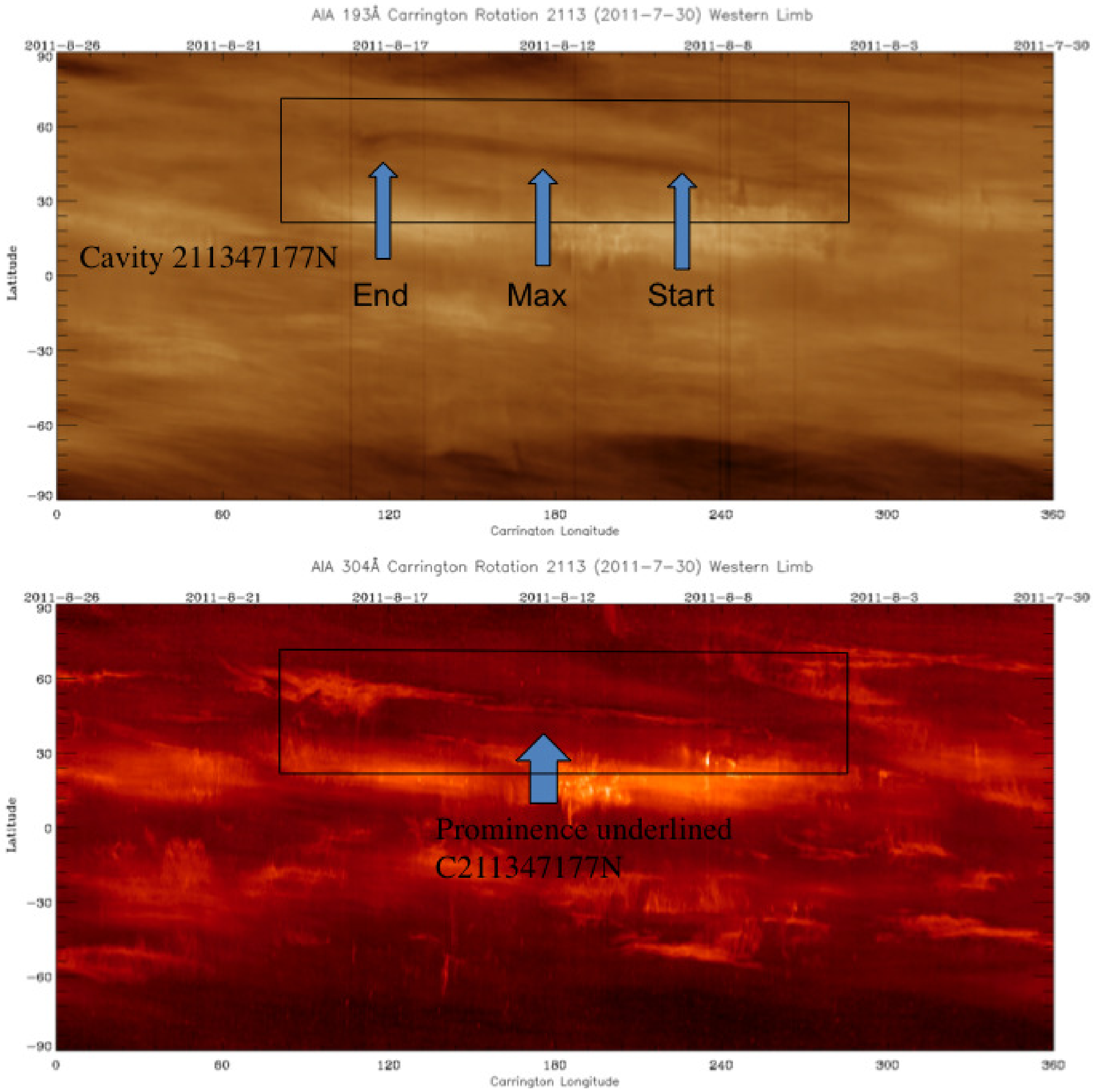

Figure 2.3: Cavity C211347177N displayed in limb-synoptic maps from two AIA passbands. Top: AIA 193 Å CR 2113 western limb synoptic map. The box encloses the cavity. The three arrows indicate the three positions of cavity: the fully developed starting location, its maximum width, and just before disappearing. Bottom: AIA 304 Å CR 2113 western limb synoptic map. The box now encloses the prominence associated with the cavity.

visible until 109°, spanning about 171° degree in longitude. The latitudinal variation along the length of the cavity can be noted from Figure 2.3. The beginning point of the cavity is at 32° N latitude. The cavity then appears gradually at higher and higher latitudes as time goes by. The ending latitude of the cavity was 56° N. The difference between the starting and ending latitude is about 8°. Apparently, the cavity axis is not parallel to the latitudinal line, it is tilted 8°.

The width of the cavity was measured in AIA 193 Å at the three points shown in Figure 2.3: a) The East-end point when the cavity first became fully visible; b) The maximum width attained by the cavity; and c) The West-end point just before the cavity disappeared. The widths at these locations are 113 Mm, 122 Mm and 109 Mm respectively. The aspect ratio between the length and the maximum width, is thus 1360 Mm : 122 Mm, or 11 : 1. Therefore, the shape of the cavity is essentially a long tube, curving above the surface of the Sun.

2.3.2 Height Measurement

Time snapshot images were used to determine the height of the cavity. We applied the radial gradient filter in all snapshot images. Figure 2.4 is an off-limb close-up on the cavity and prominence at 02:19 UT on 14 August 2011. In AIA 193 Å (Figure 2.4a) and AIA 211 Å (Figure 2.4b) passbands, the elliptical boundary of cavity is outlined/defined clearly. In Figure 2.4a and Figure 2.4b, a cavity is seen as a dark ellipse. In AIA 171 Å (Figure 2.4c), a U-shaped feature is noticed. We measured the distance between the solar limb and the U-shape structure, which gives the height of the base of the cavity. Figure 2.4d is a snapshot of the prominence associated with the cavity in AIA 304 Å. The cavity is located just above the elongated prominence material. It is found that the bottom of the cavity is 26 Mm above the solar surface in 171 Å passband. The maximum heights attained by the cavity were 185 Mm (0.27 $R_\odot$) in AIA 193 Å and 170 Mm (0.24 $R_\odot$) in AIA 211 Å.

2.3.3 Magnetic Field

Prominence are always formed above the polarity inversion lines (Mackay and van Ballegooijen, 2009) and cavity C211347177N was associated with a prominence. We used HMI

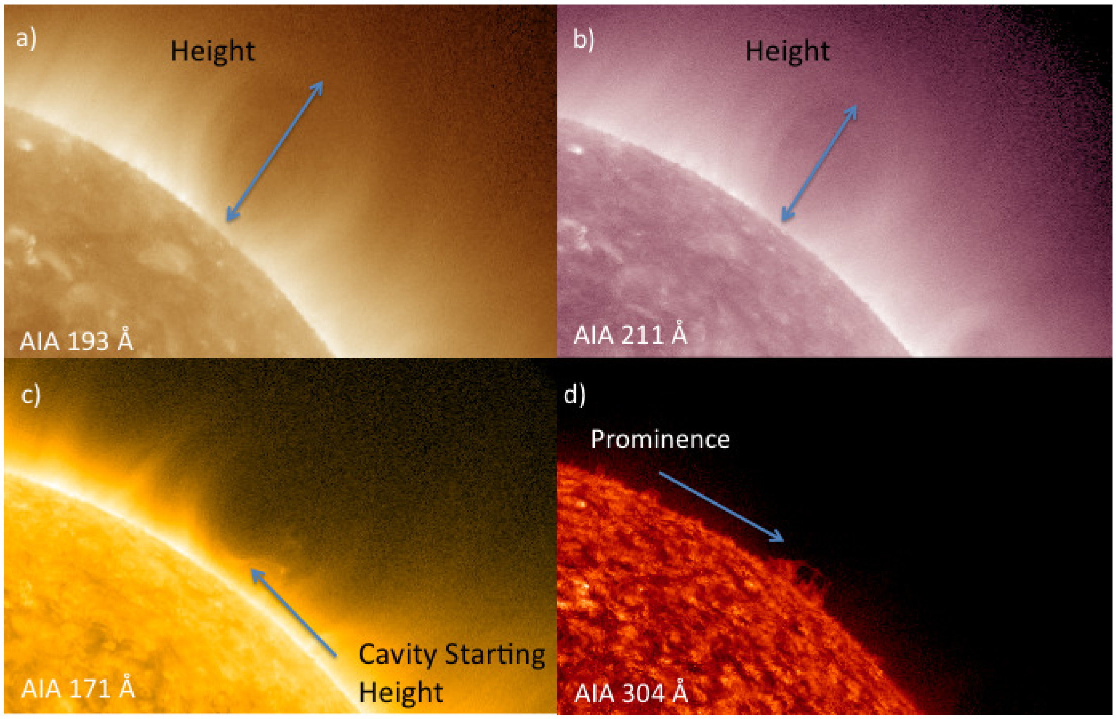

Figure 2.4: Off-limb close-up on the cavity and the prominence structure. The top two images (a and b) show the height of the cavity in 193 Å and 211 Å. The bottom left (c) in AIA 171 Å is the best wavelength passband to measure the starting height of the cavity. The lower right panel (d) shows the prominence associated with the cavity as seen in AIA 304 Å.

magnetic field data (Schou *et al.*, 2012) to examine the correlation between cavity morphology and the underlying magnetic field distribution. An HMI central meridian synoptic map was constructed to study the underlying magnetic field as HMI data at the limb are less useful due to the projection effect in the photosphere. In order to be consistent with the exact cavity location, we used HMI data from one week earlier than the AIA data, as it takes one week for features to rotate from disk center to the western limb. HMI synoptic maps were constructed using a process similar to that used to generate EUV central meridian synoptic maps described in Karna, Hess Webber, and Pesnell (2014). In short, the longitudinal stripes of width 13.6°, centered at the central meridian running from latitude −90° to 90°, four images per day (six hour cadence), are overlapped over each other from right to left onto a rectangular grid for 27.27 days. The total stripes are then divided by the number of overlapped stripes to get the average value at each pixel of the synoptic map. The constructed HMI central synoptic map is 1080 pixels in latitude, and 3600 pixels in longitude (For more details see Appendix).

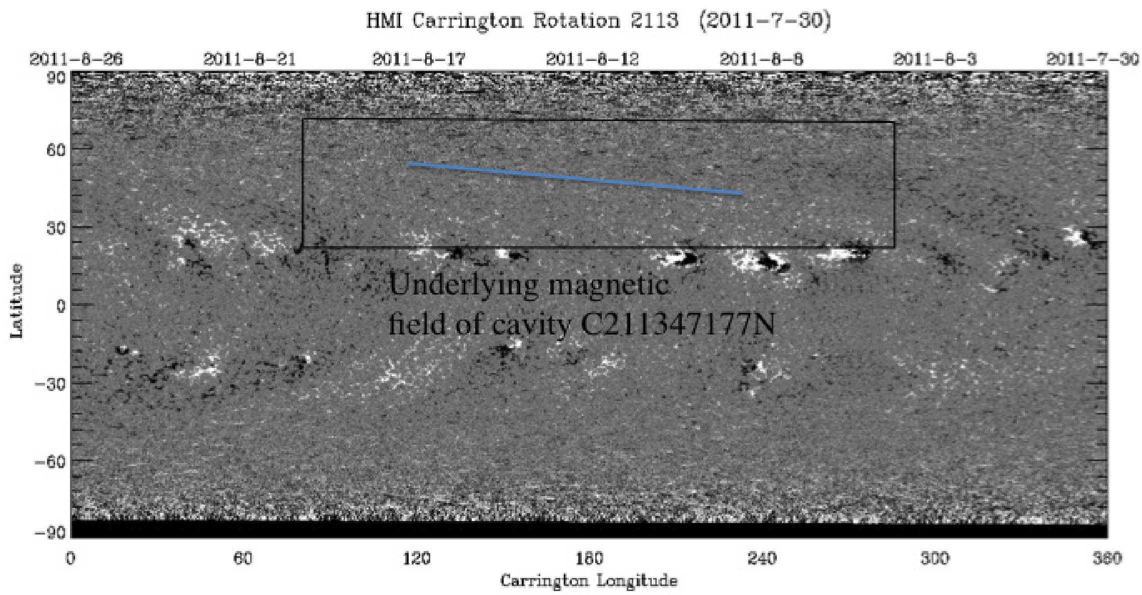

Figure 2.5: HMI synoptic map for Carrington Rotation 2113. The black bounding box is the same as in Figure 2.3. The solid line inside the black bounding box appears to lie in the polarity inversion line, over which prominence is formed. The black region at the bottom shows the heliographic latitudes obscured by the solar B_0-angle.

In Figure 2.5, the outlined polarity inversion line of the magnetic field (blue line) appears at the same location as cavity C211347177N. Apparently, the cavity is caused by the underlying bipolar magnetic field, which is elongated and tilted. We believe such an elongated bipolar field may originate from a decayed active region.

2.3.4 DEM Distribution

We use a Differential Emission Measure (DEM) analysis to infer the temperature and density of the cavity. The DEM analysis is based on the six EUV passband observations of the solar corona from the SDO/AIA (Cheng *et al.*, 2012). The SSW routine `xrt_dem_iterative2.pro` contains the code used to compute the DEM. The routine uses a forward-fitting approach. First the intensity of six passbands are normalized by the exposure time. After that, the cavity and its background regions are selected using the 4×4 pixel square bounding boxes shown in Figure 2.6. Since this routine only works on a single pixel value and N channels at a time, we spatially average over all pixels in the boxes. The averaged count rates are used as the input of `xrt_dem_iterative2.pro` routine to calculate the DEM curve.

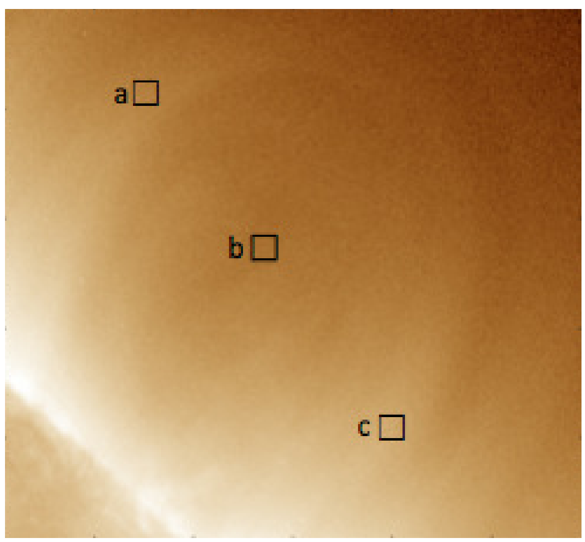

Figure 2.6: Cavity C211347177N as seen on the western limb in AIA 193 Å on 14 August 2011. The boxes show the sub-regions where the DEM was calculated: outside cavity (a and c) and inside cavity (b).

After calculating the DEM, we use DEM-weighted average temperature per pixel $\bar{T}$ to characterize the temperature and emission measure of the cavity, using the Cheng *et al.*

(2012) formula

$$\bar{T} = \frac{\int \mathrm{DEM}(T) \times T \, dT}{\int \mathrm{DEM}(T) \, dT}. \tag{2.1}$$

Next, the total emission measure (EM) is calculated using

$$\mathrm{EM} = \int \mathrm{DEM}(T) \, dT. \tag{2.2}$$

In Figure 2.6, the three regions indicated by boxes a, b, and c correspond to locations of the cavity where the DEM was calculated. Boxes a and c are regions outside of the cavity, and box b is center of the cavity. The red solid curves in Figure 2.7 indicate the best-fit DEM solution to the observed radiances. The dashed lines are the Monte Carlo solutions of the original data within added noise on each channel. The upper and lower dashed lines at a given temperature can be regarded as the uncertainties in the best-fit solution (Cheng *et al.*, 2012). One hundred Monte Carlo realizations of the data are used. The integration is carried out over the temperature range of $5.8 < \log T < 7.1$. From the DEM curves of three sub-regions, we can find that the cavity has a higher temperature, but a lower emission measure than the surrounding plasma (Figure 2.7). The DEM-weighted average temperature of the cavity (box b in Figure 2.6) is 2.8 MK, whereas that of the left (box a) and right (box c) background regions are 2.55 MK and 2.58 MK respectively. The emission measure of the cavity (box b), left (box a), and right (box c) region outside cavity are 1.74×10^{26} cm^{-5}, 2.83×10^{26} cm^{-5} and 1.97×10^{26} cm^{-5} respectively. The root mean squares calculated from the 100 Monte Carlo solutions are regarded as the uncertainties of the temperature and EM of the cavity over the temperature range of $5.8 < \log T < 7.1$. The EM and temperature uncertainties in the cavity were up to 19% ($\pm 5.3 \times 10^{25}$) and 30% (± 0.8 MK), respectively.

2.3.5 Polar view

Figure 2.8 is the northern polar view of Cavity C211347177N in four passbands AIA 193, AIA 211, AIA 171 and AIA 304 Å. Limb synoptic map is applied as a texture to spherical mesh and the polar view is obtained. The cavity appears as an elongated spiral dark region in AIA 193 Å (top left) , AIA 211 Å (top right) and AIA 171 Å (bottom left) wavelength and spiral prominence is observed in AIA 304 Å (bottom right) polar map. The black small circles are the northern poles.

2.3.6 3D Geometric Shape of Cavity

To understand how the 3-D structure of the cavity would be viewed from the Earth, we modeled cavity C211347177N using the length and width measurements from synoptic maps and the height measurements from snapshot images. We use the *paraview* software tool to visualize the cavity's geometry in 3-D (Figure 2.9). The AIA 304 Å limb synoptic map is projected onto a sphere to show as the background. We select nine points along the prominence that refer to nine different time periods. The heights are measured at those times and then the modeled 3-D tube is constructed over it. The cavity width was not observed to change greatly during these observations, so the width of the tube was set to the average width of the cavity, as the aspect ratio of the length to width and the length to height are 11 : 1 and 7 : 1, respectively. These aspect ratios indicate that the cavity has a long tube shape with an elliptical cross section. The black horizontal line represents the equator of the sun and the vertical line represent the meridian at 180°. The elliptical tube shaped cavity is not fixed to the same latitude. The latitudes vary smoothly along the length of the cavity. The tilt angle between the starting and ending latitudes is about 8°.

2.4 Discussion and Conclusions

We have developed a limb synoptic map method to identify coronal cavities and further study their properties. Limb synoptic maps are the convenient way to identify a cavity.

Table 2.1: Cavity Properties from AIA 193 Å

Parameter	Value	
Starting postion	32° (latitude)	280° (longitude)
Ending positon	56° (latitude)	109° (longitude)
Length	1360 Mm (1.96 $R_\odot$)	
Height	185 Mm (0.27 $R_\odot$)	
Width	Start (2011-08-09 05:19:55)	113 Mm (0.16 $R_\odot$)
	Max (2011-08-14 02:19:55)	122 Mm (0.18 $R_\odot$)
	End (2011-08-17 22:19:43)	109 Mm (0.15 $R_\odot$)
Temperature	2.8 ±0.8 MK	
Emission Measure	$(1.74 \pm 0.3) \times 10^{26}$ cm^{-5}	

More important, length can be measured in terms of both days and meters (solar radii). Coronal cavity C211347177N was used in this paper to illustrate such a study. Table 2.1 shows the measurement results of the cavity. Major results are summarized as follows.

- The derived length of the cavity is about 1360 Mm, spanning over 170° in longitude. The cavity was visible above the limb for 13 days. The disappearance of the cavity was associated with an eruption of the underlying prominence.

- The cavity width varies between $0.15 - 0.18$ $R_\odot$ and the height varies between $0.24 - 0.27$ $R_\odot$.

- The Differential Emission Measure method was used to show that the cavity is hotter and it's emission measure is lower than the surrounding corona.

- The overall 3-D topology of the cavity is a long tube with an elliptical cross section. The aspect ratio of the length : width and the length : height are 11 : 1 and 7 : 1, respectively.

- The cavity tube is slightly tilted in latitude, with the starting latitude at 32° and the ending latitude at 56°. The latitude varies smoothly along the length of the cavity.

- An elongated diffuse bipolar region is observed underneath the cavity in the photosphere. The polarity inversion line is consistent with the axis of the cavity.

Fuller and Gibson (2009) found that, in their study of 24 cavities observed in MK4/MLSO, the widths range between 0.12 and 0.76 $R_\odot$ and the heights between 0.24 to $0.6R_\odot$. Our width measurements for cavity C211347177N is $0.15 - 0.18$ $R_\odot$ and heights of $0.24 - 0.27$ $R_\odot$, which falls in the lower end of their range. The reason behind smaller height and width is that we are comparing data from two different instruments having different field of view. In MK4 coronagraph, cavities above $1.14R_\odot$ are only observed implying Fuller and Gibson (2009) survey consists of high lying cavities, whereas we used AIA data having field of view from $1R_\odot$ to $1.3R_\odot$. Moreover, our cavity selection was based on the criteria that at least a part of a cavity should be visible between 1.05 to 1.10 $R_\odot$.

The cavity temperature is around 2.8 MK, which is slightly higher than was found for cavities by other studies (Fuller *et al.*, 2008; Habbal *et al.*, 2010; Reeves *et al.*, 2012; Vásquez, Frazin, and Kamalabadi, 2009). This difference might be due to the fact that our observations were made at solar maximum, whereas the observations of other research groups were made during solar minimum. Fuller and Gibson (2009) noted that, during near solar maximum, cavities of all shapes and sizes, are slightly brighter, denser, and hotter on average, while during the solar minima smaller and thinner cavities are more common.

In conclusion, we have shown that synoptic maps of the limb radiance are a useful way to obtain the geometric properties of coronal cavities.

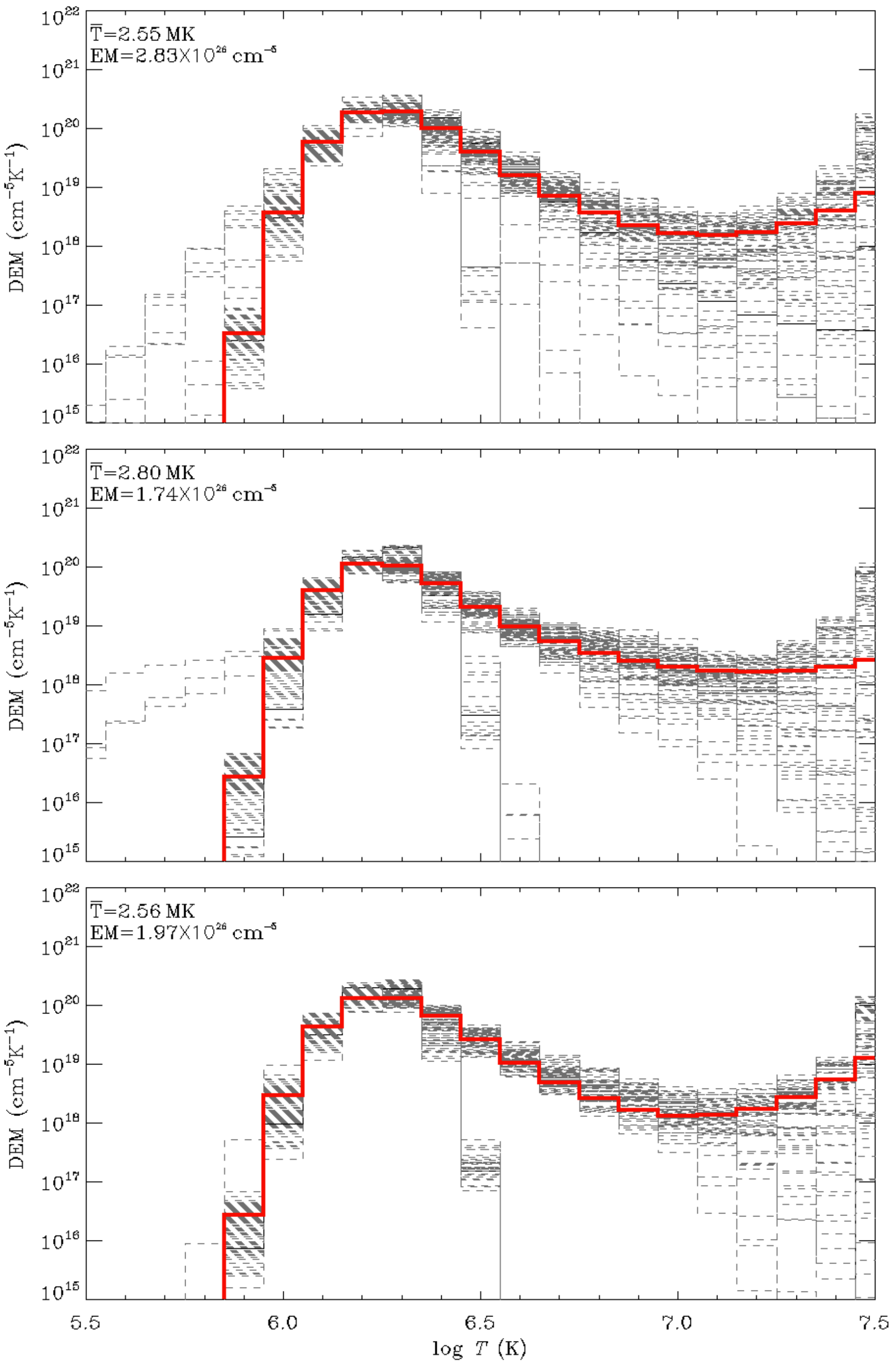

Figure 2.7: DEM measurements at three different cavity locations. The top and the bottom are outside of the cavity (indicated by boxes a and c in Figure 2.6). The middle is the DEM measured inside the cavity (box b in Figure 2.6). The red solid lines are the best fit DEM distributions and the black dotted lines are the MC solutions. The DEM is integrated over the temperature range of $5.8 < \log T < 7.1$ to derive the total EM.

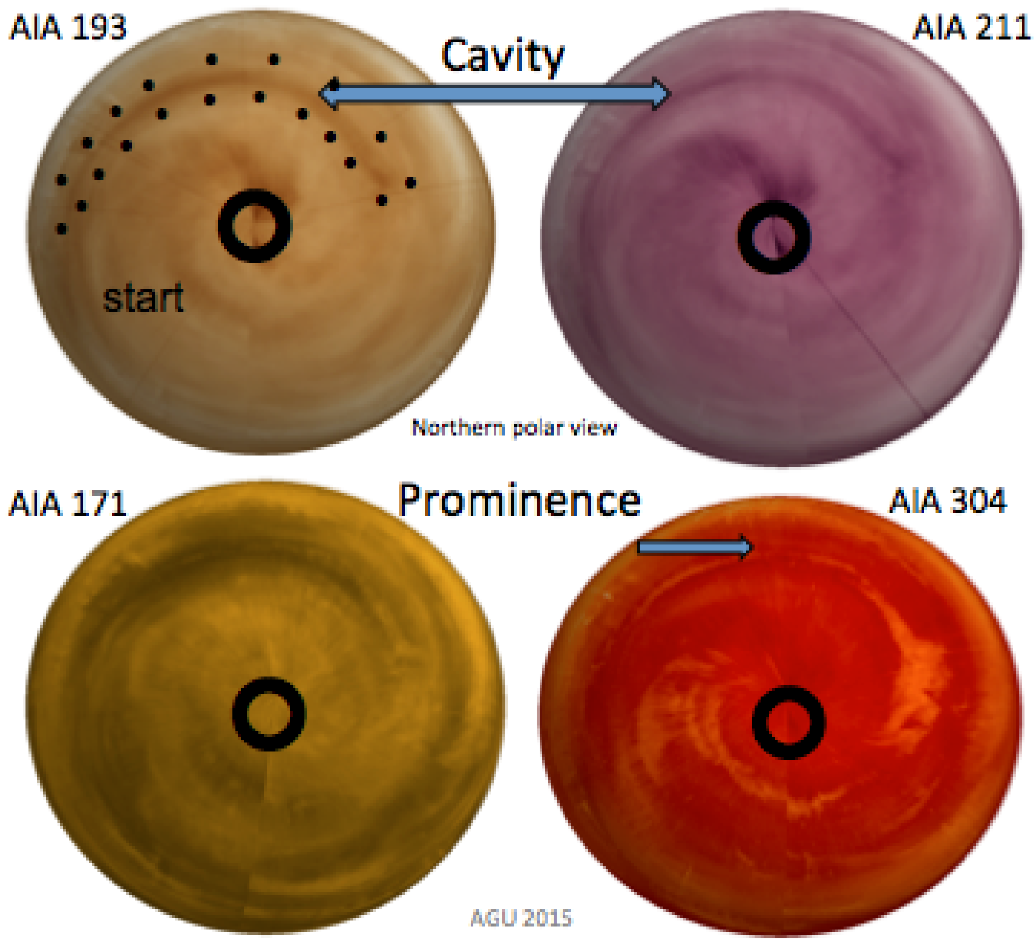

Figure 2.8: Cavity C211347177N as seen from the Northern hemisphere in AIA 193, AIA 211, AIA 171 and AIA 304 Å. The black dots boxes shows the cavity region. The black small circles are the northern poles.

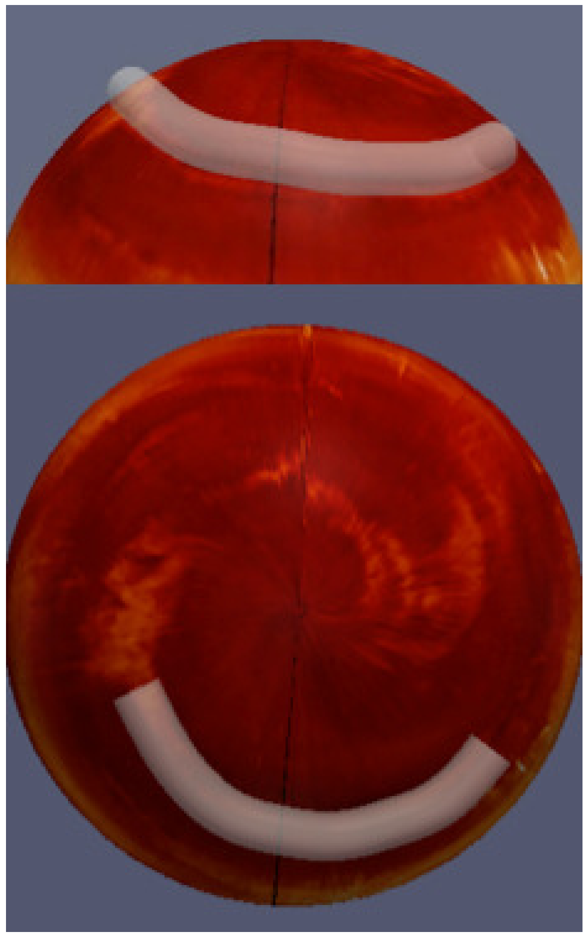

Figure 2.9: A visualization of the 3-D geometrical structure of the cavity. Top: Close-up on tilted view of tube shaped cavity encircling the sun. Bottom: Polar view of the cavity from Northern hemisphere. The black line in both panels represents the meridian at 180°. The black horizontal and vertical lines in the represent the equator and the meridian at 180°, respectively.)

Chapter 3: A survey of coronal cavity and statistical study

3.1 Introduction

This chapter contains a largest survey of 429 coronal prominence cavities found between May 2010–Feb 2015 using EUV limb synoptic maps and investigate how the coronal prominence cavity provides new insight into the global magnetic field evolution. The solar cycle has always been an important topic of research in solar physics. It is a dynamo process involving the transformation of a poloidal magnetic field into a toroidal and from toroidal bands to poloidal field, with the polarity opposite to that present earlier (Dikpati and Charbonneau, 1999; Parker, 1955a). The cycling dynamo is characterized by equatorward migration of sunspots as well as meridional flow. Meridional flow is the latitudinal flow of material from the equator toward the poles at the surface and from the poles to the equator below the surface. An inner return flow has been proposed to carry material from the mid-latitudes to the equator in about 11 years (Hathaway and Rightmire, 2010).

The timing of polar field reversal has been studied using the sunspot number (Babcock, 1959), coronal hole boundaries (Karna, Hess Webber, and Pesnell, 2014; Waldmeier, 1981; Webb, Davis, and McIntosh, 1984), polar magnetic field (Scherrer *et al.*, 1977; Sun *et al.*, 2015). During polar reversal, there is maximum sunspot activity, the polar coronal holes shrink and almost disappear, the polar magnetic field decreases through zero and reverses its polarity. Moreover, the migration of prominences towards the pole at the beginning of the solar cycle has been reported (Li *et al.*, 2008; Makarov and Sivaraman, 1989; Mouradian and Soru-Escaut, 1994; Shimojo, 2013; Shimojo *et al.*, 2006; Topka *et al.*, 1982).

We used data from the *Atmospheric Imaging Assembly* (AIA, Lemen *et al.* (2012)) and *Helioseismic Magnetic Imager* (HMI, Schou *et al.* (2012)) on board the *Solar Dynamics*

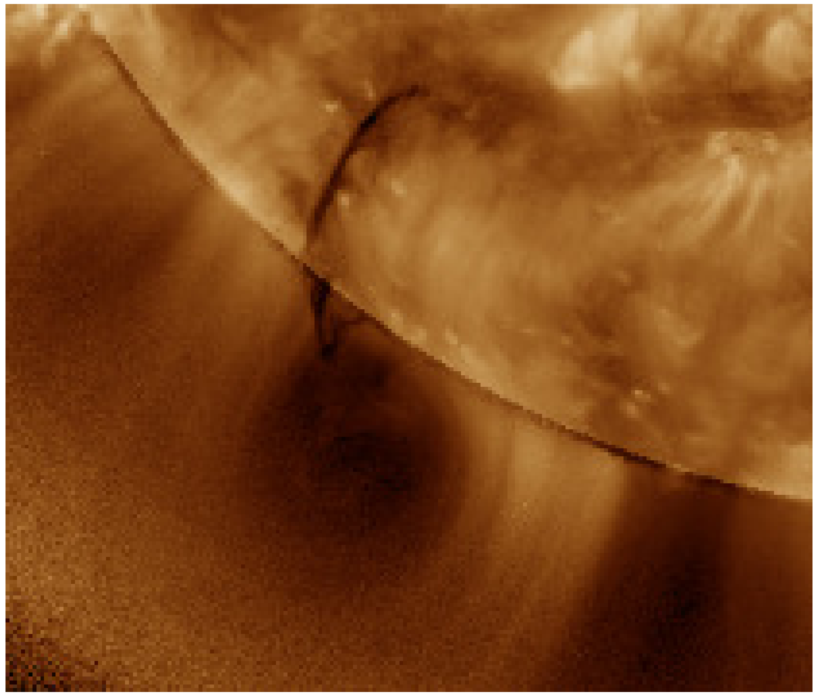

Figure 3.1: Snapshot images of cavity C21295746S as seen on the eastern limb on 30 October 2012 in SDO/AIA 193 Å passband.

Observatory (SDO, Pesnell, Thompson, and Chamberlin (2012)). We studied the 3-D morphological structure of cavities appeared between May 20, 2010–February 1, 2014 using the Limb Synoptic Maps described in Karna *et al.* (2015), hereafter Chapter 2. We measured the length, height, width, the heliographic longitudes and latitudes of the appearance and disappearance of the cavity. We also examined correlations between the heights, widths and lengths of the cavities in the catalog. We also found that cavities formed a belt moving toward the polar region with time; we call this new belt the 'cavity belt', a unquestionable evidence of surface meridional flow. The chapter is organized as follow: In Section 3.2, we describe data measurements. In Section 3.3, we present the results. In Section 3.4, we discuss what we are able to draw from our observations and compare our results with other work. In Section 3.5, we summarize our results and present our conclusions.

3.2 Methodology

We used limb synoptic maps to identify cavities. Limb synoptic maps are constructed from annuli above the solar limb as described in Chapter 2 and fig. 2.2. As described in Chapter 2, a cavity appears as an elongated dark region in both AIA 193 Å and AIA 211 Å wavelength synoptic maps, and we see a prominence at the same location in AIA 304 synoptic maps. We identified 429 cavities since the launch of SDO. We measured the length of each cavity, one advantage measurement from limb synoptic maps as described in Chapter 2. Height, and width are measured using the snapshot images at the middle time frame of cavity's evolution (for details please see appendix B.3).

We have made the following assumptions when counting the cavities.:

- If cavities appear at almost the same locations during a Carrington Rotation and also the following Carrington Rotation, they are counted as two different cavities.
- If a cavity disappears for more than 48 hours (all 48 hours in the sequence of snapshot images) and again reappears at the same latitude, it is counted as a new cavity.

3.3 Result

We made statistical study of 429 cavities observed in four and half years of data (please see appendix B.1). We divided the results in two parts i) Geometric statistical survey result and ii) Cavities evolution with solar cycle.

3.3.1 Geometrical survey

Figure 3.2 is the histogram plots of cavities latitude. It is found that 68% of cavities lied above 50°. 40% of cavities are above 50° and 58% of cavities lied between 50° and 70°. This results indicates that we observe more cavities at higher latitudes. Figure 3.3 is the histogram plot showing the location of active regions and cavities. We notice that the cavities location and Active regions location are in two different latitude range indicating

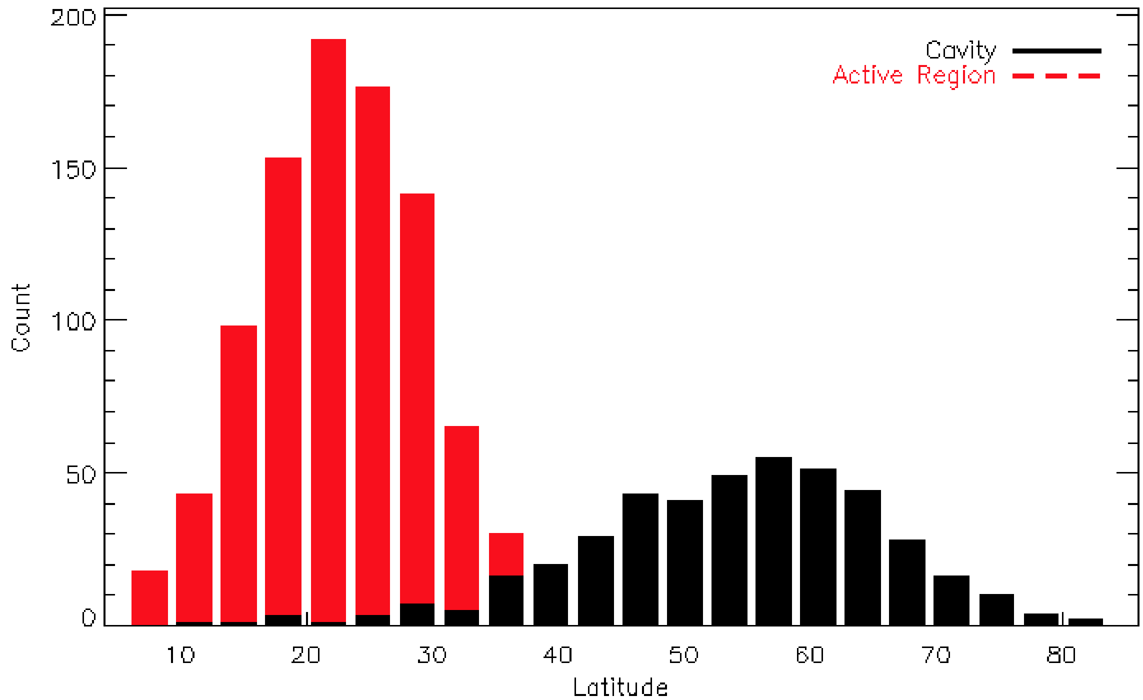

Figure 3.2: Histogram plot of cavity Latitude. Cavity appeared on Northern and Southern hemisphere are combined together.

cavities at high latitude feature and active regions as low latitude features.

Figure 3.4 shows how the height of each cavity varies with the width of the cavity. The heights of the cavities range from 0.08 $R_\odot$ to 0.5 $R_\odot$, whereas the widths vary from 0.09 $R_\odot$ to 0.4 $R_\odot$. We arbitrarily defined the circular boundary ($\frac{\text{Height}}{\text{Width}}$) to be between 0.9–1.1. In the plot the blue line with error bars represents the region of circular cavities. Cavities falling above the blue line are prolate in shape and cavities falling below the blue line are oblate in shape. The plot shows that around 38% cavities are prolate, 27% cavities are oblate, and 35% cavities are circular in shape. Typical error of measurement is 3 pixel (less than 1%), which is based on the standard deviation of measurement data to the ellipse fitting of the cavity. There is a weak linear correlation between height and width. The correlation coefficient between height and width is approximately $r = 0.6$.

Figure 3.5 shows how the length of each cavity varies with the height of the cavity. The

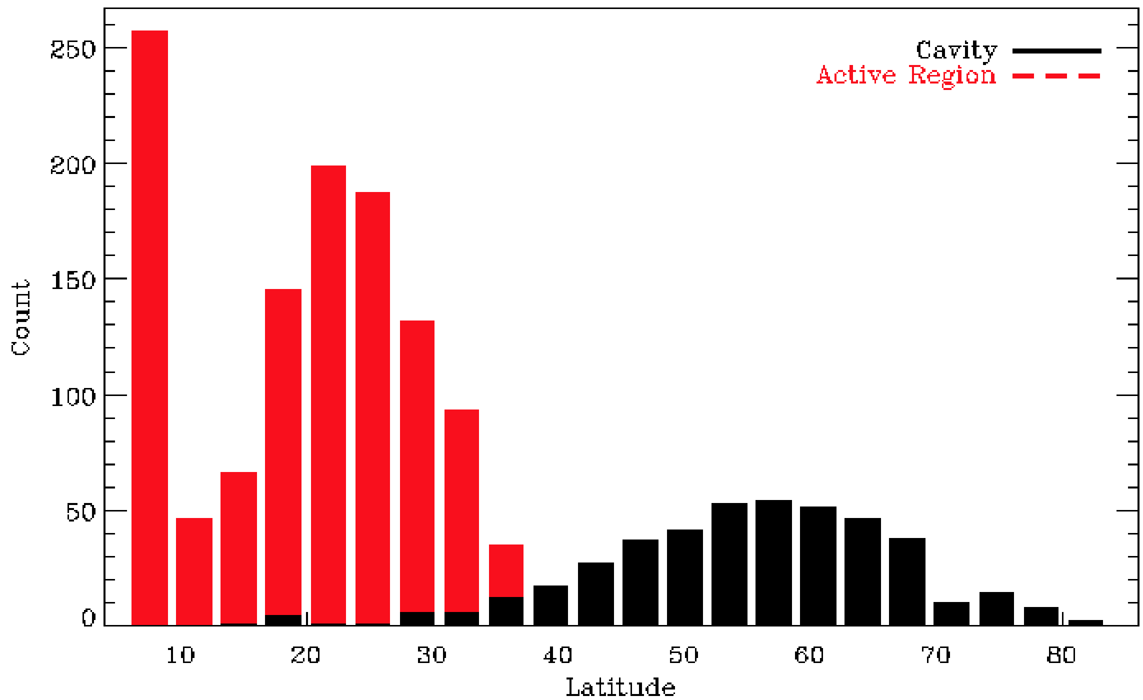

Figure 3.3: Histogram plot of Cavities and Active Regions. The red color represents an active regions and black represents cavities. The absolute latitudes are used for both Active regions and Cavities.

lengths of the cavities range from 0.06 $R_\odot$ to 2.9 $R_\odot$. One quarter of the cavities are longer than a solar radius. Cavities with length greater than 1.5 $R_\odot$ have a narrower height range (0.1–0.3 $R_\odot$), whereas cavity's length smaller than 1.5 $R_\odot$ have a wider height range (0.07–0.5 $R_\odot$). The two red lines are estimated boundary lines that show how, with increasing cavity length, the height range decreases. This result implies that high-lying long cavities are unstable and subject to eruption. We find that the overall 3-D topology of long, stable cavities as a long tube with an elliptical cross-section. We also notice that the circular and oblate cavities are more common in long cavities and infer that they are more stable than prolate shape cavities. In Figure 3.5 we also notice that the prolate cavities on average have a higher height compared to the other shapes. The shorter length and higher height of prolate cavities implies that prolate cavities are more likely to eruption.

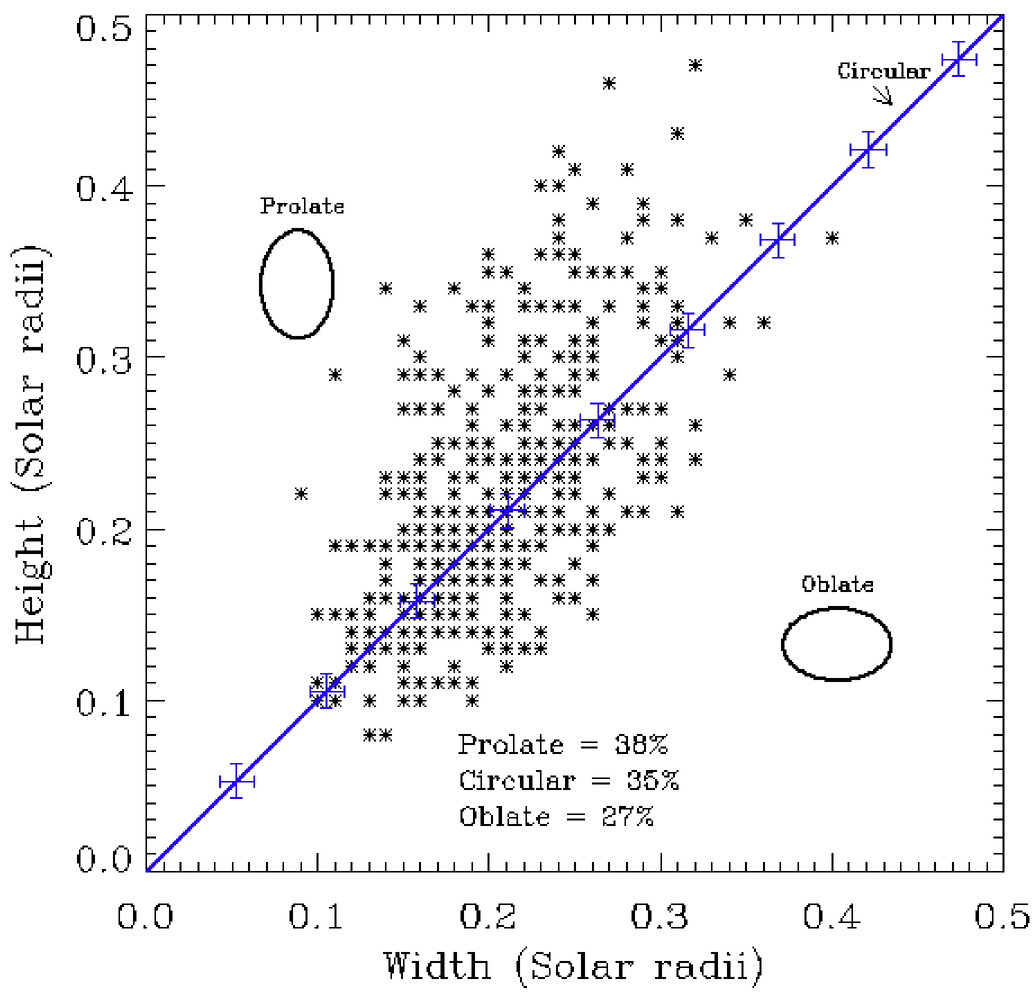

Figure 3.4: Height Versus Width. Blue line with an error bar (10%) represents the region of circular cavities. Cavities falling above the blue line are prolate in shape and cavities falling below the blue line are oblate in shape.

Forland *et al.* (2013) conducted a survey of 19 months of data using SDO/AIA image, creating a database that noted specific characteristics of the cavities in relation to their eruption as CMEs and concluded that on average eruptive cavities are narrow, high-centered, and high-bottomed. Moreover, they concluded that fitted ellipses are taller than

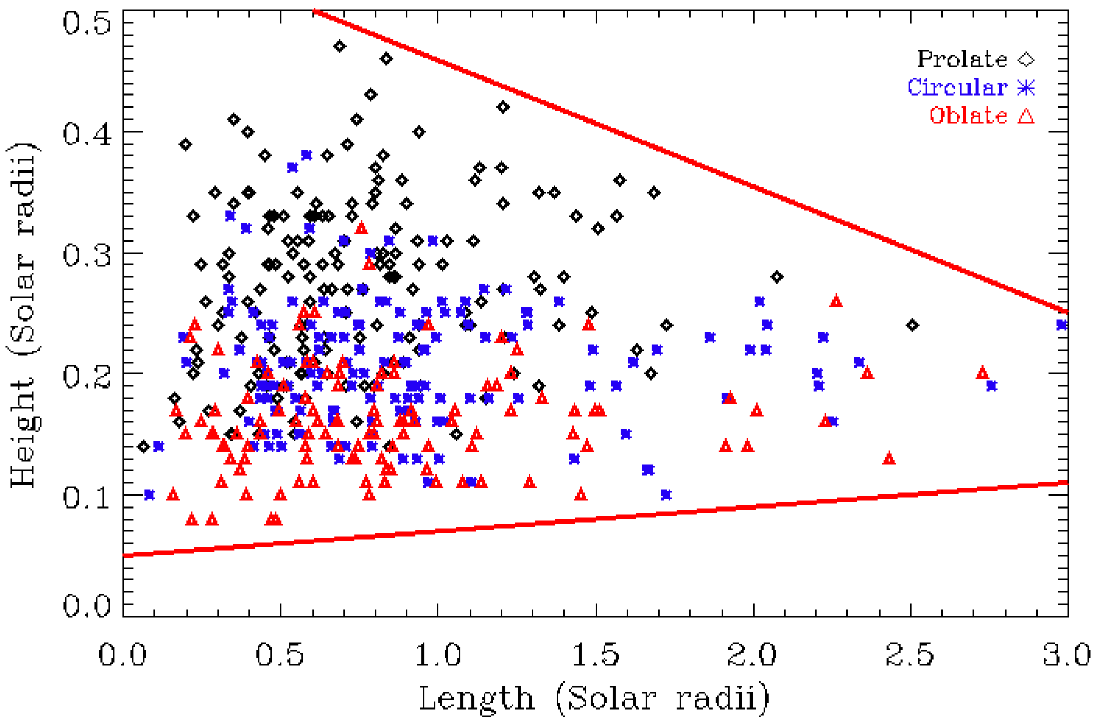

Figure 3.5: Height Versus Length. The black diamonds, blue asterisks and red triangles represent the prolate, circular and oblate shape of the cavities. The two red lines are the boundary of a region that shows how the height range narrows with increasing cavity length.

they are wide for almost all cavities whereas we find a larger fraction of cavities as oblate (Section 3.3.1). The difference in the result may be due to difference in fitting an ellipse to the cavity data. We measure the height of all cavities with an ellipse above the solar limb, where as in Forland *et al.* (2013) fit a semicircle by extrapolating ellipse below the solar limb. Moreover, we measured height and width at the middle of cavity evolution and classified it if it was prolate, near circular or oblate. Whereas, in their cases if a cavity was first observed as a semicircle and later changed to ellipse they classified it as ellipse. The last shape whatever cavity takes before eruption or disappearance was recored as the shape of a cavity.

3.3.2 Cavities evolution with Solar Cycle: Discovery of cavity belt

We plot each cavity's average latitude with time over the SDO/HMI magnetic butterfly diagram as seen in Figure 3.6. A magnetic butterfly diagram is produced by averaging the radial magnetic fields from HMI synoptic maps (Liu *et al.*, 2012) over longitude for each solar rotation described by Karna, Hess Webber, and Pesnell (2014).

In Figure 3.6, we notice that cavities form a belt moving toward the polar regions in both hemispheres; we call this the 'cavity belt'. The evolution of cavity locations apparently depends on the sunspot cycle. Sunspots start each new cycle by emerging at relatively high latitudes and emerge at progressively lower latitudes as the cycle progresses. In a time-latitude butterfly diagram, we can see active region field exhibiting a strong equatorward motion. Whereas, cavities progress towards the pole until the polar magnetic field reverses (as seen in the butterfly diagram when magnetic field changes sign) and then appear at more random locations as seen in northern hemisphere. While in the southern hemisphere the cavity belt is still seen in the polar latitudes (see Figure 3.6). The appearance of cavities at random locations has not been seen in this hemisphere as our data stops soon after the southern pole reversal. From the HMI data (Figure 3.6), we notice that the northern pole reversed in late 2012, while the southern polar magnetic field reversed in late 2014.

3.4 Discussion on the magnetic pole reversal and cavity belt

As shown in Section 3.3.2, the cavity drift towards the pole is apparently related to the polar reversal. By observing the cavity through surface magnetic field observations from HMI, we showed that the cavity belt was formed near the polar coronal hole boundary. The cavity belt disappeared after the polar magnetic field reversal. The HMI magnetic butterfly diagram showed that the northern pole reversed in late 2012, however, the cavity belt disappeared several Carrington Rotations later. On the other hand, southern pole reversed polarity in late 2014 (see Figure 3.6). We compared our magnetic butterfly diagram with Hathaway's magnetic butterfly diagram (Figure 17 of Hathaway (2015)) and in both, we

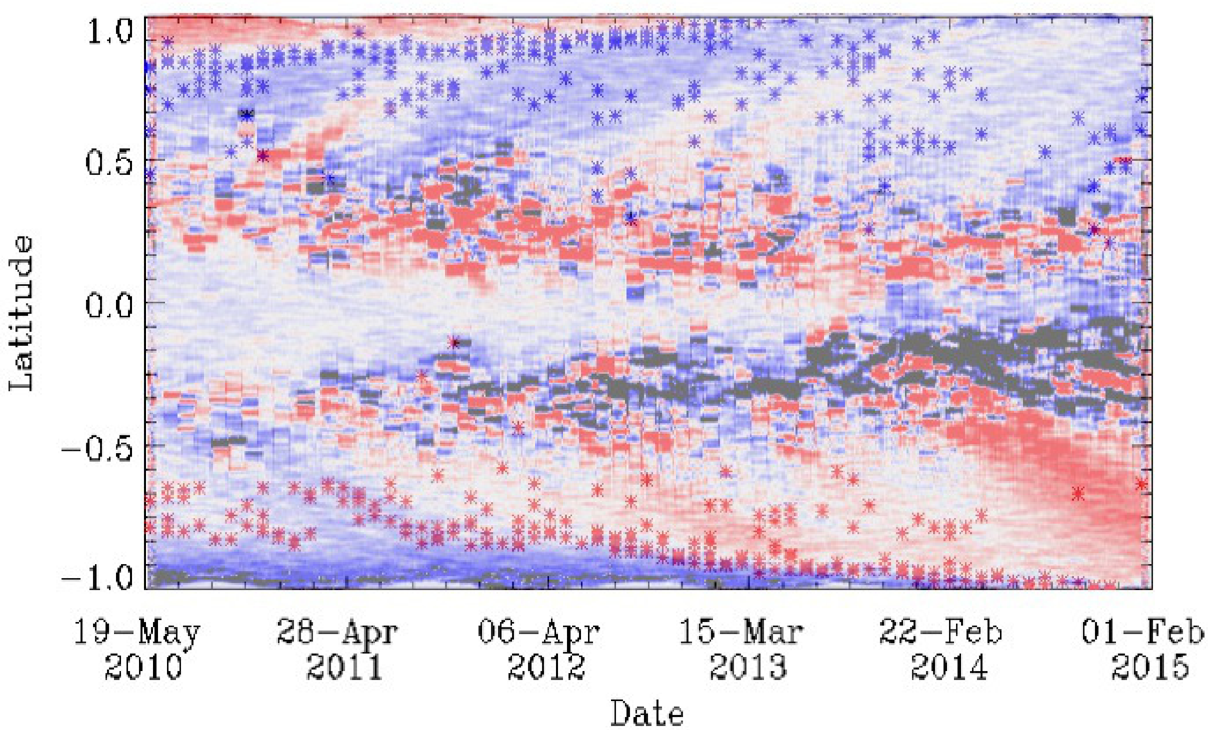

Figure 3.6: Time-latitude Butterfly diagram. The blue and red asterisks are cavities average latitude positions obtained from the limb synoptic map appeared in northern and southern hemisphere. Red regions have negative polarity, and blue regions have positive polarity.

noticed that southern magnetic field reversed in late 2014. However, the results from the solar polar fields strengths measured by the *Wilcox Solar Observatory* (WSO), show that the northern polar field changed its polarity first in June 2012 but fluctuated around zero magnitude from March 2014 till late in 2014, while the southern polar field reversed in July 2013 (see Figure 3.7).

Our HMI results for the timing of the polar field reversal in the northern hemisphere (Figure 3.6) differs by six months with the filtered WSO data. HMI data shows that the southern polar magnetic field reversed in late 2014 which is 1.5 years difference after

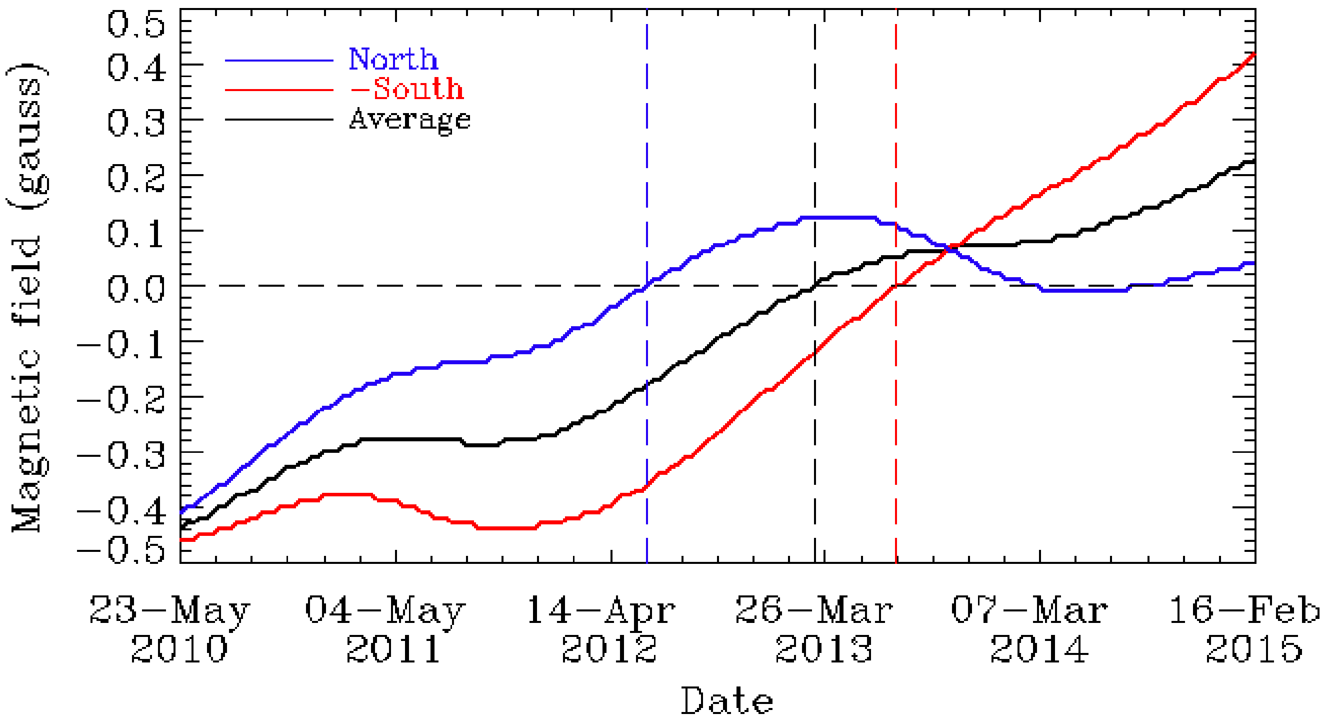

Figure 3.7: Solar polar magnetic strength data from the *Wilcox Solar Observatory*, filtered by a 20 nHz lowpass filter. The blue, red and black lines represent the magnetic field strength at the North pole, South pole and their Average. Vertical lines represent the estimated time of the magnetic field reversals.

the WSO reversal at mid 2013. Moreover, the cavity belt disappeared from the Northern hemisphere within few rotations, and the cavity belt disappeared in the southern pole just around the time of HMI reversal. Our cavity belt disappearance timing agrees more with the HMI data reversal timing.

The monthly Sunspot Number (Figure 3.8) peaked in late 2011, primarily due to activity in northern hemisphere, whereas activity in the southern hemisphere peaked in Feburary 2014. Comparing Figure 3.6 and Figure 3.8, it shows that northern pole reversed one year after sunspot maximum while southern sunspot number peaked 9 months earlier than southern pole reversal.

The key question is what causes cavity belt to exist? For this we measured the poleward

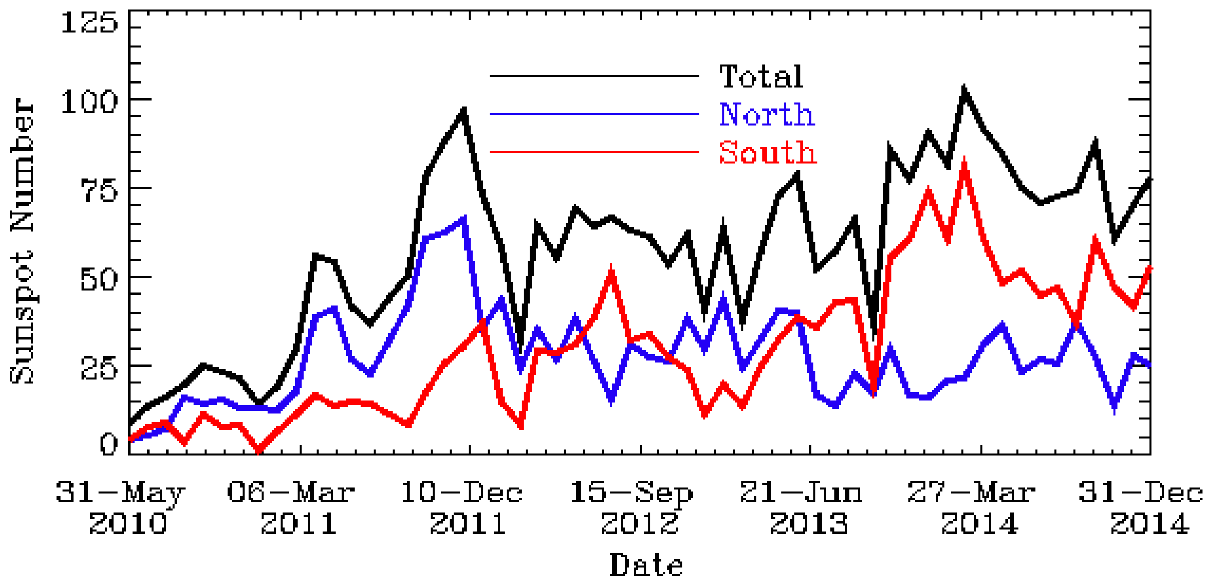

Figure 3.8: Monthly Sunspot Average. Blue and red represents the northern and southern hemispheric sunspot number. Black line represents the total sunspot number.

velocity of the cavity belt by fitting our cavities latitude linearly and calculated that the cavity belt migration speed. The cavity belt migration speeds in the northern and southern hemisphere were 5.0 m/s and 3.7 m/s. Two things we can notice from our result. First, our result is consistent with the meridional flow speed of 5.0 ± 2 m/s at 75° latitude from Hathaway and Rightmire (2010) based on the magnetic features from May 1996 to June 2009 observed by the *Michelson Doppler Imager* (MDI) onboard the *Solar and Heliospheric Observatory* (SOHO). Our results suggest that the cavity drift towards the pole to form the cavity belt is due to meridional flow. Second, cavity belt drift is slower in the southern hemisphere. The late reversal in the southern pole may be due to slower meridional flow in the southern hemisphere. Moreover, we also noticed that from time to time cavities following surges in both hemisphere.

The migration of prominences towards the poles during the ascending phase of the solar cycle has been reported by (Li *et al.*, 2008; Makarov and Sivaraman, 1989; Mouradian and Soru-Escaut, 1994; Shimojo, 2013; Shimojo *et al.*, 2006; Topka *et al.*, 1982). As an example, Shimojo *et al.* (2006) compared prominence activity data from July 1992 to December 2004 from *Nobeyama Radioheliograph* (NoRH) with butterfly diagrams obtained from synoptic Carrington maps of *Kitt Peak National Observatory* magnetograms. They concluded that the drift of the prominences follows the poleward motion of the magnetic flux until the reversal of the polar polarity; after reversal filaments slowly migrates towards the equator. A similar result was obtained by Li *et al.* (2008) from the latitudinal migration of filament activity over the full solar disc using the Carte Synoptique solar filament archive. Our results agree that before the pole reversal cavity belt moves toward higher latitudes. From Figure 3.6 we can see right after reversal in the northern hemisphere cavity belt disappeared, and later cavities appeared at random latitudes.

Topka *et al.* (1982) used Hα synoptic charts from 1964 to 1980 and calculated a poleward drift velocity of about 10 m/s, which is twice our meridional flow speed in the northern hemisphere. This differences may come from looking at two different solar cycles. Shimojo (2013) extended the NoRH prominence data until March 2013 and calculated the migration velocities in the northern hemisphere to be 5.2 m/s for Solar Cycle 24 and concluded that a poleward motion of prominences was an indicator of the meridional flow. In the southern hemisphere only two prominence activities occurred at over $-65°$ latitude after 2009 therefore poleward expansion was not measured. Our cavity belt drift speed from the northern hemisphere agrees with that from Shimojo (2013).

Moreover, we tried to find the temporal trend of oblate cavities as a function of solar cycle (by plotting fraction of oblate cavities with time) but we find no correlation with solar cycle.

3.5 Summary and Conclusion

We present a survey of 429 coronal prominence cavities found between May 2010–Feb 2015 using SDO/AIA limb synoptic maps. Our findings showed that

- 68 % of cavities lied above 50°. 40% of cavities are above 50° and 58% of cavities lied between 50° and 70°.

- 38% of cavities are prolate, 27% oblate and 35% circular in shape.

- Cavities longer than 1.5 $R_\odot$ have a narrower height range (0.1–0.3 $R_\odot$), whereas cavities shorter than 1.5 $R_\odot$ have a wider height range (0.07–0.5 $R_\odot$).

- The overall 3-D topology of the long stable cavities can be characterized as a long tube with an elliptical cross section.

- Circular and oblate cavities have longer length than prolate cavities.

- Early in a sunspot cycle cavities form a belt moving toward the polar region with time; we call this the cavity belt.

- Cavity belt migrated towards higher latitude with time and the cavity belt disappeared after the polar magnetic field reversal.

- The HMI magnetic butterfly diagram showed that the northern pole reversed in late 2012, however, the northern cavity belt disappeared several Carrington Rotations later. While southern pole reversed polarity in late 2014 and cavity belt disappeared exactly at the time of southern pole reversal.

- The HMI magnetic field diagram northern polar field reversal timing (late 2012) differs by six months with the filtered WSO data (mid 2012), and the HMI results (late 2014) from the southern hemisphere is one and half year delay in comparison to WSO data (mid 2013). In the WSO data the northern hemisphere returned to near zero in 2014 and only recently appears to have reversal.

- Cavity belt migration speeds in the northern and southern hemisphere were 5.0 m/s and 3.7 m/s, implying cavity belt migration is due to meridional flow.

- The late reversal in the southern pole may be due to slower meridional flow in the southern hemisphere.

We have undertaken the largest catalog of EUV coronal cavities (429 cavities between May 19, 2010 to Feb 1, 2015) and have made the catalog publically available. Our analysis shows that the cavity belt migrates towards higher latitudes at the time of magnetic field reversal and could be used to establish the time of polar magnetic field reversal. Our result gave us new insight to look at the global magnetic field. This study shows that the cavity evolution provides another dimension of information of solar cycle.

Chapter 4: How is circum-polar cavity formed?

4.1 Introduction

This chapter focuses on the evolution of the photospheric magnetic field near a circumpolar crown cavity that lasted for several rotations. This is the first study of how cavity's underlying polarity inversion line (PIL) formed. It is very important to understand the magnetic configuration wherein cavity polar crown cavity forms. The distribution of solar activity over the Sun's surface changes over the course of the 11-year solar cycle. Solar cycles are correlated with emergence and decay of the active regions (ARs). ARs emanate from localized concentrated magnetic fields emerging from the solar interior at the mid-latitudes at the beginning of the cycle (Parker, 1955b). As the cycle progresses, the emergence of newer ARs shifts from mid-latitudes toward the equator at the end. The poleward migration of decayed trailing polarity flux leads to the polar magnetic field reversal, which is an important phenomena for our understanding of solar cycles (Babcock, 1961; Wang, Nash, and Sheeley, 1989). Coronal cavities are solar feature providing insight into the detailed process of the polar reversal. Coronal cavities are large scale structures in the Sun's corona that are closely related with the long term evolution of the magnetic field in the photosphere as well as solar activity such as coronal mass ejections and filament eruptions. The locations of cavities at high latitudes can be used to establish the time of polar magnetic field reversal (Karna, Pesnell, and Zhang, 2015). Coronal cavities are dark, roughly elliptical regions of low density relative to the surrounding corona (Gibson *et al.*, 2010) that surround prominences when viewed off a limb in EUV and white light coronal images. A cavity often contains a prominence and/or filament underneath. We will use the both words interchangeably.

The formation mechanism of polarity inversion line (PIL), which separates negative and positive polarity, underneath the prominence, and thus the cavity, has always been an important topic of research in solar physics. Tang (1987) classified prominence formation mechanism into two categories according to the nature of PIL formation. In the first type the filaments formed over a PIL lying within the same bipolar region called “a bipolar region filament”. In the second type PIL formed between two separate bipolar region classified as “a between bipolar region filament”. Later, Tandberg-Hanssen (1995) described these two categories as Type A and Type B, respectively. Mackay, Gaizauskas, and Yeates (2008) renamed Type A and Type B as Internal Bipolar Region (IBR) and External Bipolar region (EBR) and added two more categories. The third category he added is referred as “Internal/External Bipolar Regions (I/EBR) filaments”, where PIL lies above both the internal PIL of a bipole and the external PIL surrounding the bipole. The fourth category he added is classified as “Diffuse Bipolar Distributions (DBR)”, where the polarities defining the bipole did not emerge at the same time, and these distributions are formed through multiple flux emergence. The diffuse region can no longer be associated with any single bipole emergence.

Figure 4.1 taken from Mackay, Gaizauskas, and Yeates (2008) demonstrates the four PIL classes. In the Figure 4.1(a): PIL formed between single bipole classified as IBR. Figure 4.1(b): PIL formed between external bipoles or between bipoles and unipolar regions of flux are classified as EBR. Figure 4.1(c): filaments that lie above the internal PIL within a bipole and the external PIL outside the bipoles are classified as I/EBR. Figure 4.1(d): PIL line formed at the diffuse bipolar distribution classified as DBR.

In this chapter, we investigate the PIL formation mechanism of a polar crown cavity that was observed in year 2013 in the both limbs in the southern hemisphere associated with a polar crown filament with great detail. From here we call the cavity circumpolar cavity. We find that this is the longest lasting cavity in the maximum phase of Solar Cycle 24 which was observed for a year in 2013. However, for our study we made eight month (from March 21, 2013, till October 31, 2013) detailed observation of circumpolar cavity using high temporal cadence and spatial resolution observations from the Atmospheric Imaging Assembly (AIA, Lemen *et al.* (2012)) and the Helioseismic Magnetic Imager (HMI, Hoeksema *et al.* (2014)) instruments on board the *Solar Dynamics Observatory* (SDO, Pesnell, Thompson, and Chamberlin (2012)). The Chapter is organized as follows. In Section 2, we describe observations. In Section 3, we describe the formation mechanism of circumpolar cavity. In Section 4 we discuss about our results and in Section 5 we present our conclusions.

4.2 Continuous observation of cavities over several Carrington Rotation

We examined a circumpolar crown filament cavity from March 21, 2013, till October 31, 2013, on the southern limb associated with the polar crown filament. However, the cavity was observed on the limb for more than a year. We used both AIA snapshot images and AIA limb synoptic maps (Karna *et al.*, 2015) described in Chapter 2 to examine the evolution of the cavity. Most of the time, the cavity was visible on both the eastern and western limbs shown in Figure 4.2. During the observation period, the cavity sometimes erupted and reformed within a few hours. Even after an eruption, the cavity was sometimes visible at the same location. We also observed bodily eruption of the cavity as a CME (June 17, 2013). Table 4.1 and Table 4.2 are the list of times that prominence erupted, and we also checked if prominence eruptions were associated with CMEs or not. Altogether, we found 19 eruptions in which 17 eruptions were associated with CMEs. We also observed vertically oriented fine plasma thread. We also observed flows in the cavity. The flows were sometimes swirling motions in the plane of sky. Sometimes, the cavity appeared very dark due to the nearby presence of coronal holes and sometimes bright due to nearby active regions impinge cavity density was mostly effected by the ambient environment. The goal of this chapter is to study the underlying magnetic field of such a long cavity, not a detailed study on

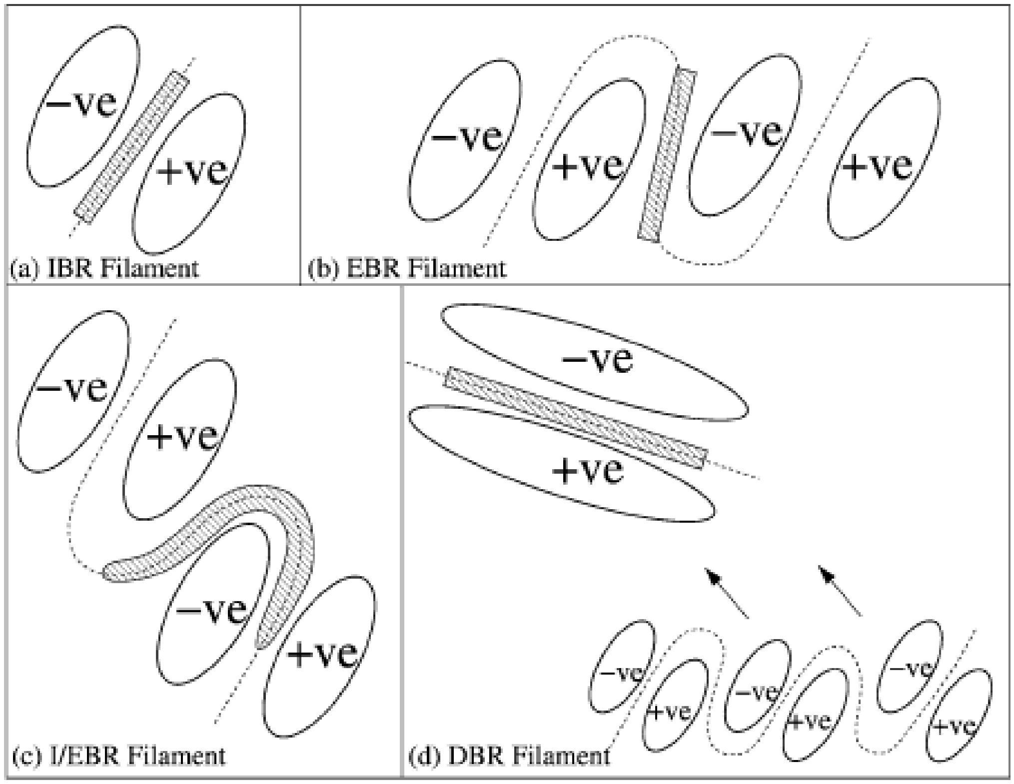

Figure 4.1: Classification schemes for solar filaments. Categories (a) and (b) were based on Tang (1987) and (Tandberg-Hanssen, 1995). Mackay, Gaizauskas, and Yeates (2008) added categories (c) and (d). (a) Internal Bipolar Region (IBR): filaments forming above the internal PIL of a single bipole. (b) External Bipolar Region (EBR): filaments forming on the external PIL between bipoles or between bipoles and unipolar regions. (c) Internal/External Bipolar regions (I/EBR): filaments lying above the both internal bipole and the external PIL outside the bipoles. (d) Diffused Bipolar Region (DBR): filaments lying above PIL that formed over diffuse bipolar distributions. Adapted from Mackay, Gaizauskas, and Yeates (2008).

eruptions and flow motions.

To understand the magnetic configuration underlying the cavity we constructed magnetic synoptic maps (Karna *et al.*, 2015) from CR 2135 to CR 2142 (March 21, 2015 - October 25, 2015) using 720-second line-of-sight (LOS) magnetograms from HMI/SDO. The maps are 3600 pixels with longitude in degree along the x-axis and latitude in degrees along the y-axis. The scaling range of the magnetic synoptic map field strength is between

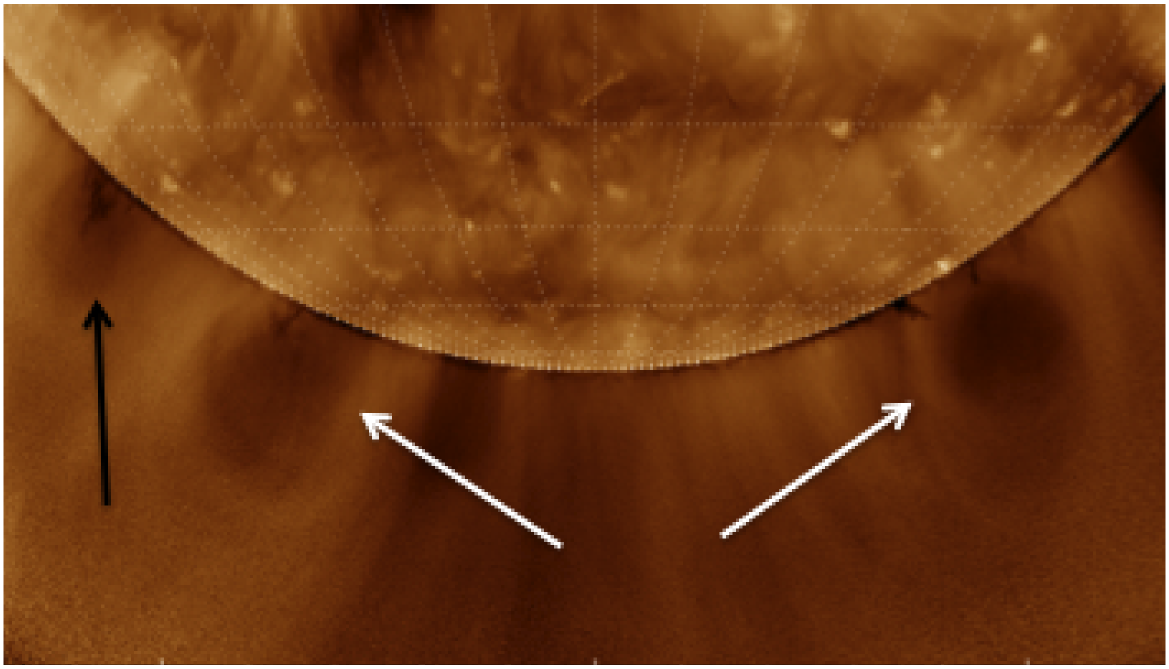

Figure 4.2: Three cavities observed on May 29, 2013 in AIA 193 Å (pointed by one black and two white arrows). Cavity closest to the pole on the eastern limb and the cavity observed on the western limb (pointed by two white arrows) are associated with the same PIL.

± 3 G. Details about constructing the HMI synoptic maps are described in appendix A.

Table 4.1: Eastern Limb Events

Date	Prominence Eruption	CME
23 April 2013	1:30-5:30 UT (latitude)	yes
28 April 2013	18:00 UT (latitude)	yes
25 may 2013	22:14 UT	yes
02 June 2013	14:30 UT	yes
17 June 2013	16:30 UT	yes (cme with cavity)
03 July 2013	06:30 UT (small)	no
29 August 2013	06:30 UT	yes
13 September 2013	18:30 UT	yes
23 October 2013	19:30 UT	yes

Table 4.2: Western Limb Events

Date	Prominence Eruption	CME
21 March 2013	08:15-09:30 UT (latitude)	yes
28 March 2013	22:14 UT (latitude)	yes
18 April 2013	07:15 UT	yes
07 May 2013	11:45 UT	yes (cme with cavity)
17 May 2013	05:30 UT	no
15 June 2013	22:59 UT	yes (fast)
09 July 2013	12:30 UT	yes
15 August 2013	14:30 UT	yes
04 October 2013	14:36 UT	yes
20 October 2013	23:24 UT	yes

4.3 Interaction between decayed active region and polar coronal hole

Figure 4.3 shows the location of the cavity observed in AIA 193 Å (top), AIA 304 Å (middle) HMI LOS (bottom) Eastern Carrington maps for Carrington Rotation 2136.AIA 193 Å and AIA 304 Å eastern limb syncopic maps are constructed from annuli above the solar eastern limb. The boundary is drawn using the AIA 193 Å map as the cavity's depleted center, boundary, and outer bright streamer is most clearly defined in AIA 193 Å passband (top). The cavity boundary fits well the edge of the prominence in the AIA 304 Å passband (middle). The HMI LOS Eastern Carrington map (bottom) is constructed by concatenating strips of equal width in longitude, centered on the central-meridian longitude of each solar disk. Blue represents the positive flux and red represents the negative flux. We note that the eastern limb data rotates to the central meridian data after one week. HMI LOS data at the limbs are less useful due to the projection effect in the photosphere. So, to be consistent with the measured cavity location, we used HMI LOS data from one week later than the AIA data i.e., the eastern limb data rotates to the central meridian data after one week. In the HMI LOS Eastern Carrington map, we have blue (positive field) on both the poles at this period of time because the Northern hemisphere had already changed its polarity, whereas Southern hemisphere has not yet changed. The center of the cavity boundary lies almost between the trailing polarity of diffused bipolar region (red) and the unipolar magnetic field present in the southern hemisphere. Mostly the boundary center towards the unipolar field and it might be due to the geometrical effect as we are plotting coronal feature location on top of the photospheric magnetic field.

Similarly, figure 4.4 shows the location of the cavity observed in AIA 193 Å, AIA 304 Å and HMI LOS in Western limb for same Carrington Rotation 2136. The boundary is drawn using the AIA 193 Å. Western Limb HMI LOS synoptic map is constructed using HMI data from one week earlier than the AIA data, as it takes one week for features to rotate from disk center to the western limb. In western limb also notice that the center of the cavity boundary lies between the trailing polarity (red) and the unipolar magnetic field present in the southern hemisphere.

In Figure 4.5(a-f), the cavity boundary is determined from the 193 Å on the eastern limb are over plotted on the HMI LOS eastern limb magnetograms (from CR 2135−CR 2140). In every plots, the cavity boundary lies between the trailing polarity (red) and the unipolar magnetic field (blue) present in the southern hemisphere.

Figure 4.6(a)-(h) Carrington maps shows the flux transport from multiple active regions. The Carrington maps are not projected to eastern or western limb. Each synoptic magnetograms (Figure 4.6(a)-(h)) show the distribution of the radial field. The y-axis of this maps represent the latitude, and the x-axis represents the Carrington longitude. Blue represents the positive flux and red represent the negative flux. The boxes are drawn on top of the maps showing trailing polarity (red) flux transport towards the pole. Over the period of eight months, a significant number of new active regions emerged at the active region latitude. While, no flux emergence at higher latitude close to the PIL that we used for our study. Fluxes are continuously transported from different emerged active regions towards the higher latitude. We measured the time for trailing flux to get transported from active region latitude (around 30°) towards the pole (around 60°) with the average speed of around 10m s^{-1} including both meridional flow and diffusion and counted the number of active regions contribution in the flux transport. It took around 9−10 month for a trailing flux from around 30° to reach around 60°. We found that 28−75 active regions were contributing to the flux transfer from CR 2124 to CR 2131. The lower limit of the active regions number is based on the observation when we observed the comma structure of trailing flux connected with active regions between the pole and the active region latitude, while the upper limit of active regions number is the total number of active regions emerged in the southern hemisphere within eight month period. In the lower limit, the comma structure may be a combination of more than one active region.

4.4 Discussion on flux cancellation due to multiple decayed active regions

From the observations (Figure 4.5 and Figure 4.6), it can be clearly seen that the polar crown filament is formed in the magnetic configurations involving multiple diffused bipole interactions between the trailing part of decayed active regions and the unipolar magnetic field in the pole. The trailing fluxes were coming from multiple decayed active regions emerged at different time period. The unipolar field may have formed in the previous solar cycle. If we classify in terms of Mackay, Gaizauskas, and Yeates (2008) classification, our PIL lay over trailing polarity of diffused bipolar region and the unipolar field, but the flux was transported from multiple decayed active regions. So, we added a new category called "Diffused bipole and polar coronal hole interaction region". Continuous transport of flux makes cavity stable for a long period of time. From Figure 4.6, it is seen that polar crown cavities may show solar cycle dependency. As more bipoles emerge on the Sun, there is more chance of strong, active region diffuse and hence more flux transport by surface motion to the higher latitude making polar crown cavities more common during the time of solar maximum.

The mechanism acting on the formation of the circumpolar cavity in the southern hemisphere is illustrated by a conceptual model shown in Figure 4.7. At first, multiple active regions emerges (P1N1, P2N2) at the mid-latitude shown in Figure 4.7(a) with the Joys law bipole tilt, i.e., the leading polarity closer to the equator than the trailing polarity. Next, leading polarity (N1 and N2) migrates toward the equator, while trailing polarity of active regions (P1 and P2) migrates towards the pole (Figure 4.7(b)). During the migration the multiple diffused trailing polarity merges (Figure 4.7(c)). Three kinds of mechanism are acting in the active regions: diffusion, differential rotation and meridional flow. The active regions flux are diffused in both directions latitudinally (north-south) and longitudinally (east-west), differential rotation shears the active region in east-west direction while meridional flow carries the trailing flux towards the pole (Wang, Nash, and Sheeley, 1989). Meridional flows and diffusion have a contribution in transporting the following polarity fields towards the pole. The differential rotation makes the trailing flux tilt. The effect of diffusion in carrying flux towards the pole is very small. The meridional flow plays a major role in carrying trailing flux towards the pole. As the trailing polarity reaches the coronal hole boundary, a new PIL is formed where the polar crown cavity is formed. However, in between the diffused opposite fluxes PILs are also formed where cavities can form. Besides these processes, there is also on going flux cancellation (Mackay, Gaizauskas, and Yeates, 2008) through collisions of opposite polarities as trailing polarity is climbing towards the pole. Flux cancellation at the neutral line of sheared magnetic field leads to the formation of helical field lines, which supports cavity and prominence plasma (van Ballegooijen and Martens, 1989). If flux cancellation keeps on continuing, it may lead to the polar field reversal. However, we were not able to observe flux cancellation in the photosphere as the magnetic field strength was very low.

We will use the van Ballegooijen and Martens (1989) flux cancellation model to explain the process. We have briefly described flux cancellation model in Chapter 1, however, we will now go into the details of the model as it applies to the polar crown filament. According to this model, flux cancellation happens at the neutral line of sheared magnetic field that lead to formation of helical field lines. These field lines support the cavity and the prominence plasma. The magnetic structure is found to be stable. If flux cancellation continued, it subjects to an eruption. Figure 4.8 outlines the formation of helical field lines driven by flux cancellation process in a sheared magnetic field. Figure 4.8(a) is an initial potential field i.e., field lines are perpendicular to the PIL. Figure 4.8(b) shows sheared magnetic field produced due to the plasma flows along the PIL. The magnetic field is increasingly sheared in Figure 4.8(c) due to flows towards the neutral line. AB and CD are marked as two sheared loops. Later in Figure 4.8(d) shows how reconnection can happen between AB and CD producing one long loop AD and a short loop CB. The small loop CB submerges into the solar surface due to its small radius of curvature and stronger tension force. Moreover, as overlying loops EF and GH come closer to the neutral line (Figure 4.8(e)) they can reconnect producing one helical loop EH wrapping around the AD loop that supports the prominence plasma and a shorter loop GF that submerges into the solar surface (Figure 4.8(f)).

During the eight-month period of data, we observed nineteen eruptive events associated with the circumpolar cavity. On average two events were, at least, six days apart from each other. The destabilization was observed in connection with several phenomena, including photospheric motions with magnetic flux transport, remote flares that initiates wave disturbances, and neighbor cavity/prominence eruption. Out of nineteen, three eruptions were caused by the neighbor (cavity/prominence) eruption. One eruption was due to a wave initiated by active region eruption. The majority of eruption may have happened due to the adding of magnetic flux by photospheric motion near the PIL. The flux transport causes flux cancellation perturbing the existing magnetic field, and the changes result in the source of eruption (Parenti, 2014).

4.5 Conclusion

For the first time, we studied the formation mechanism of the long lasting circumpolar cavity. The studied cavity is the longest cavity of the maximum phase of Solar Cycle 24 and was observed in the year 2013. Our observation suggests two necessary conditions to form long stable polar crown cavities: 1) the underlying polarity inversion line should be formed between the trailing part of the strong active region which has been decayed for a long time and the unipolar magnetic field (polar coronal hole). There is ongoing flux cancellation between trailing flux of multiple decayed active regions and the unipolar magnetic field. 2) The long lasting polar crown cavity is sustained by the flux from the multiple newly transported active regions. Therefore, we added a new category called “Diffused bipole and polar coronal hole interaction region” in the Mackay, Gaizauskas, and Yeates (2008) classification. Moreover, the trailing polarity fluxes are associated with active regions associated with the current solar cycle, while dominant polarity flux (unipolar) flux are associated with the previous solar cycle. This is a very dynamic process that changes greatly over the course of the solar cycle. This result also suggests that special attention should be taken when interpreting the contribution of a number of ARs, which requires coupling between diffused magnetic field strength and meridional flow.

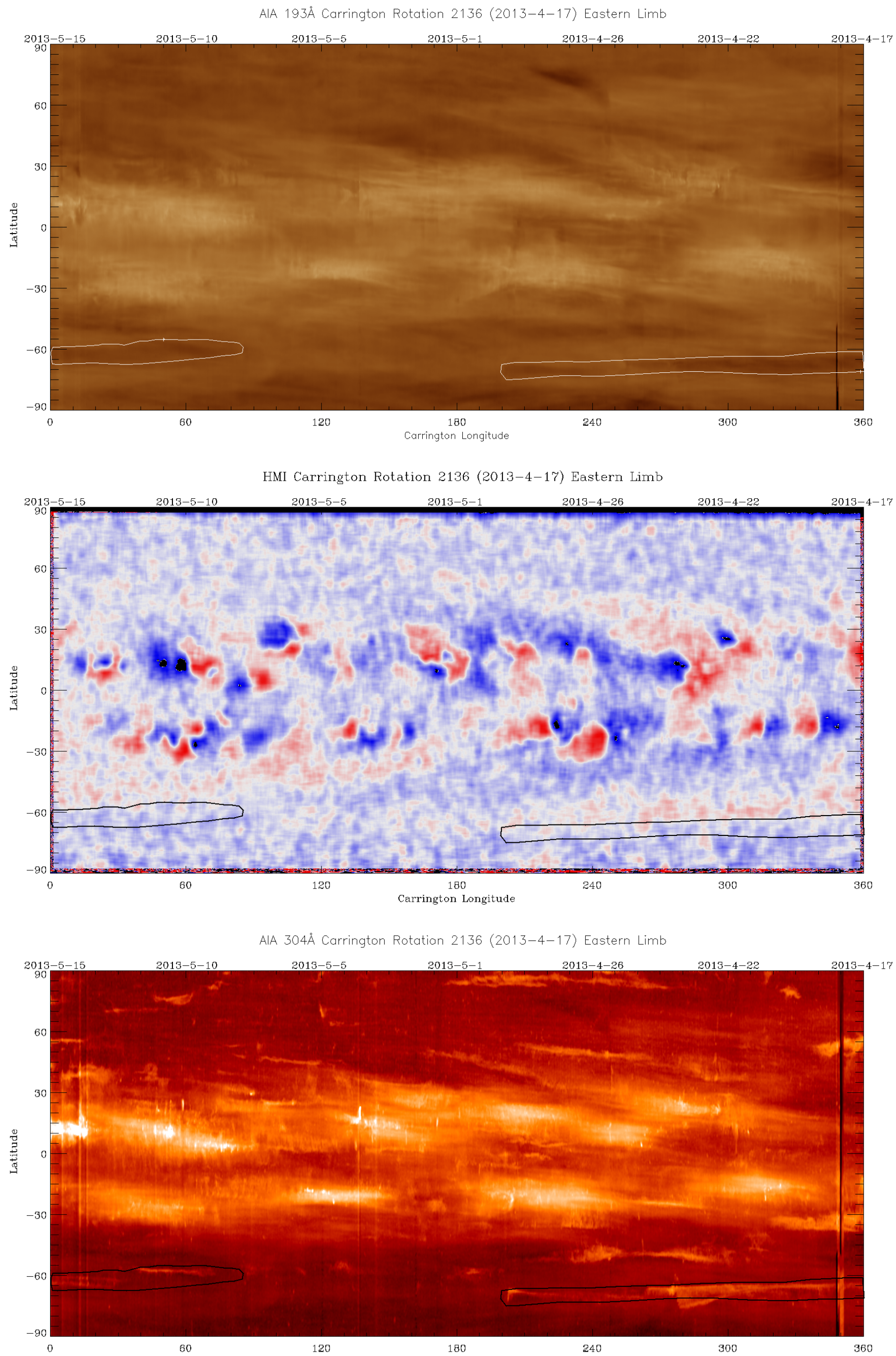

Figure 4.3: AIA 193 Å, AIA 304 Å and HMI LOS Eastern Carrington maps for Carrington rotation 2136. The solid black contour drawn on top of all three maps shows the position of the cavity. The location is based on the observation made from AIA 193 Å (top panel). The cavity's depleted center, boundary, and the outer bright streamer is clearly defined in AIA 193 Å passband. The AIA 304 Å synotic map (middle panel) shows the prominence associated with the cavity. In the HMI magnetogram (bottom panel), blue regions have positive polarity and red regions have negative polarity and image has a cutoff field magnitude of ±3 gauss.

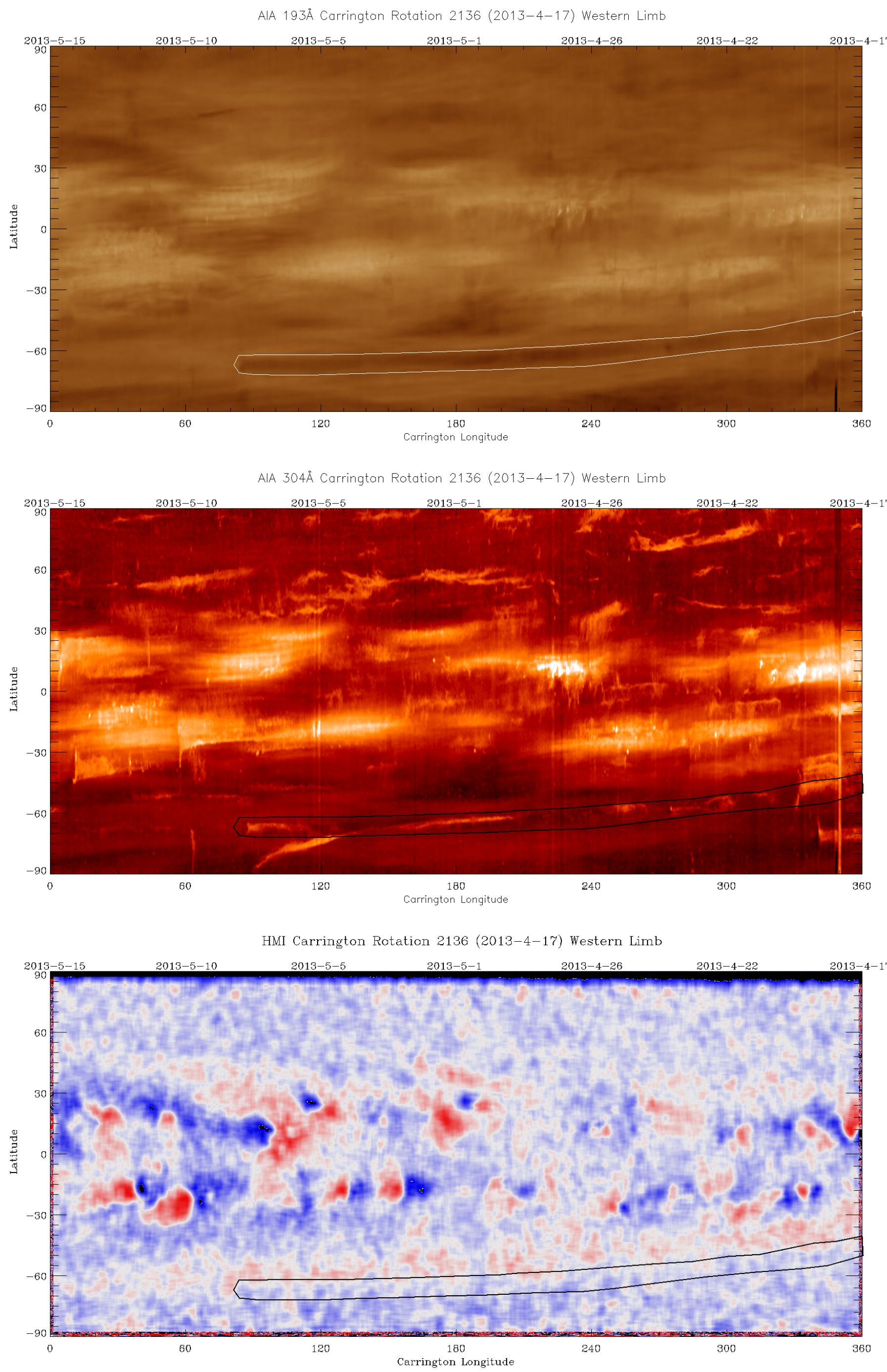

Figure 4.4: AIA 193 Å, AIA 304 Å and HMI LOS Western Carrington maps for Carrington rotation 2136. The solid black contour drawn on top of all three maps shows the position of the cavity. The location is based on the observation made from AIA 193 Å (top panel). The cavity's depleted center, boundary, and the outer bright streamer is clearly defined in AIA 193 Å passband. The AIA 304 Å synotic map (middle panel) shows the prominence associated with the cavity. In the HMI magnetogram (bottom panel), blue regions have positive polarity and red regions have negative polarity and image has a cutoff field magnitude of ±3 gauss.

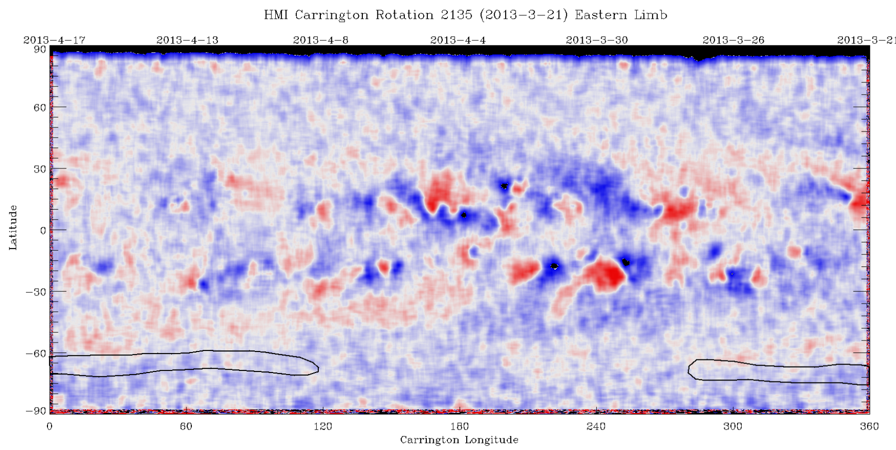
HMI Carrington Rotation 2135 (2013−3−21) Eastern Limb
2013−4−17
2013−4−13
2013−4−8
2013−4−4
2013−3−30
2013−3−26
2013−3−21
Latitude
Carrington Longitude

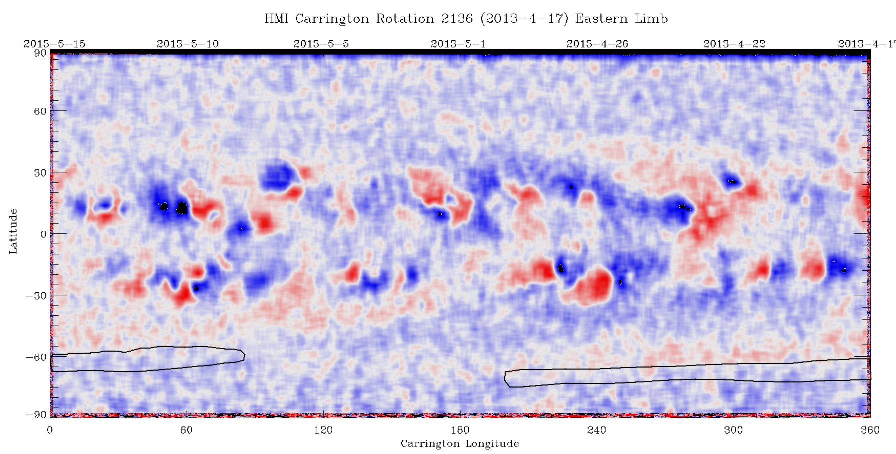
HMI Carrington Rotation 2136 (2013−4−17) Eastern Limb
2013−5−15
2013−5−10
2013−5−5
2013−5−1
2013−4−26
2013−4−22
2013−4−17
Latitude
Carrington Longitude

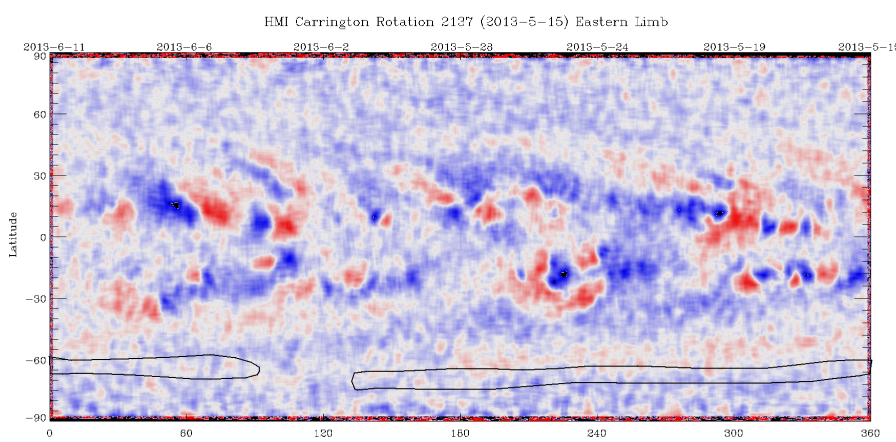
HMI Carrington Rotation 2137 (2013−5−15) Eastern Limb
2013−6−11
2013−6−6
2013−6−2
2013−5−28
2013−5−24
2013−5−19
2013−5−15
Latitude
Carrington Longitude

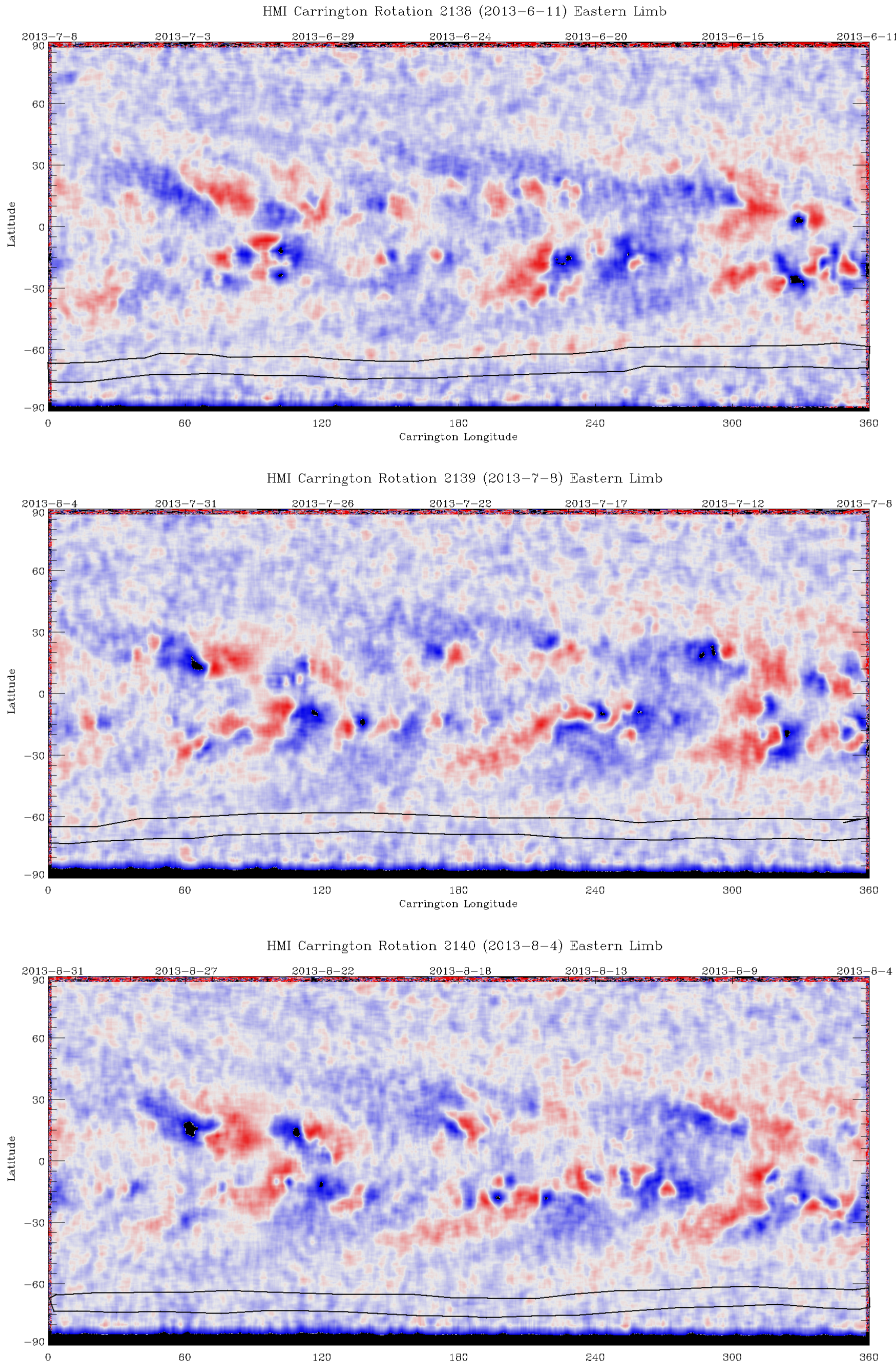

Figure 4.5: HMI Carrington maps from CR 2135 to CR 2140 (March 21, 2013 - August 31, 2013). Blue regions have positive polarity and red regions have negative polarity. In all the maps we see both the poles have blue sign as during this time period northern pole has already changed its polarity while southern pole have yet to change. The black fillings at the north or south pole are due to the B_0-angle that shifts the poles into and out of sight. This image has a cutoff field magnitude of ± 3 gauss and the solid black contour drawn on top of magnetograms the location of the cavity.

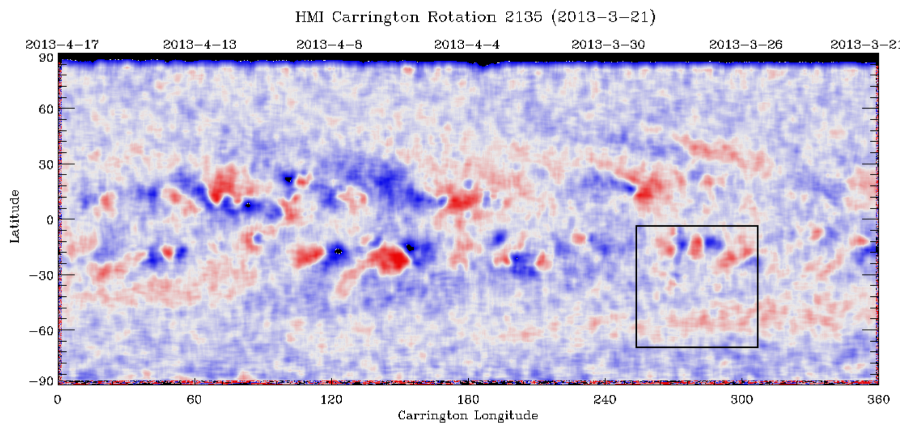
HMI Carrington Rotation 2135 (2013-3-21)
2013-4-17
2013-4-13
2013-4-8
2013-4-4
2013-3-30
2013-3-26
2013-3-21
Latitude
Carrington Longitude

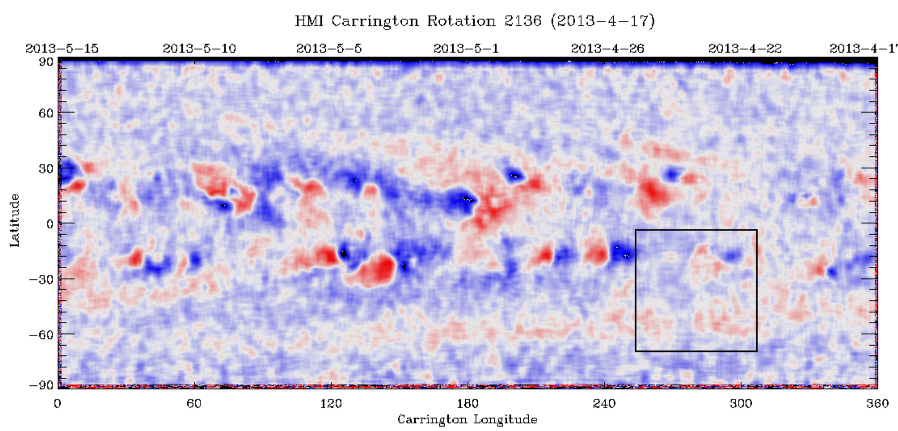
HMI Carrington Rotation 2136 (2013-4-17)
2013-5-15
2013-5-10
2013-5-5
2013-5-1
2013-4-26
2013-4-22
2013-4-17
Latitude
Carrington Longitude

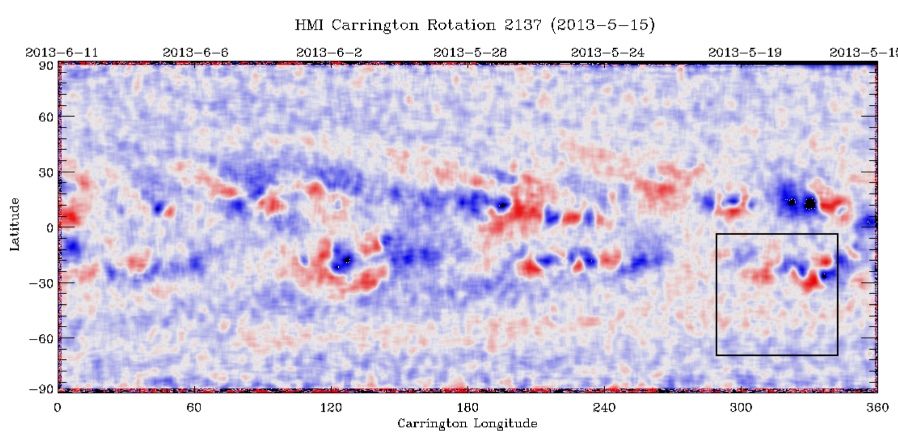
HMI Carrington Rotation 2137 (2013-5-15)
2013-6-11
2013-6-6
2013-6-2
2013-5-28
2013-5-24
2013-5-19
2013-5-15
Latitude
Carrington Longitude

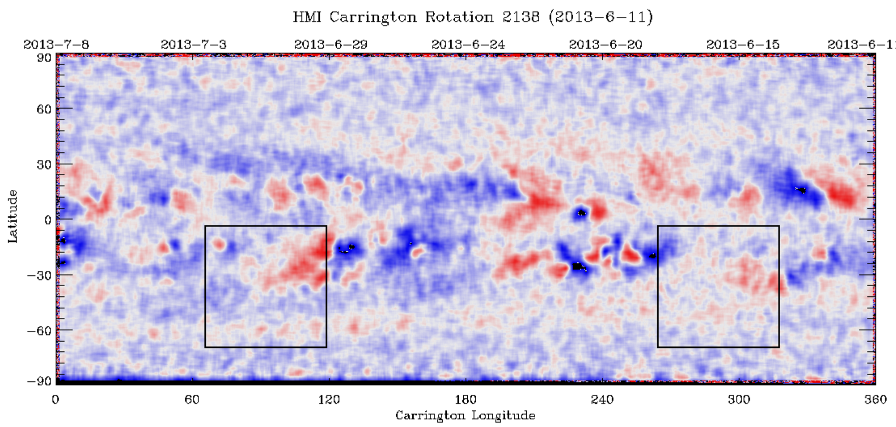
HMI Carrington Rotation 2138 (2013-6-11)
2013-7-8
2013-7-3
2013-6-29
2013-6-24
2013-6-20
2013-6-15
2013-6-11
Latitude
Carrington Longitude

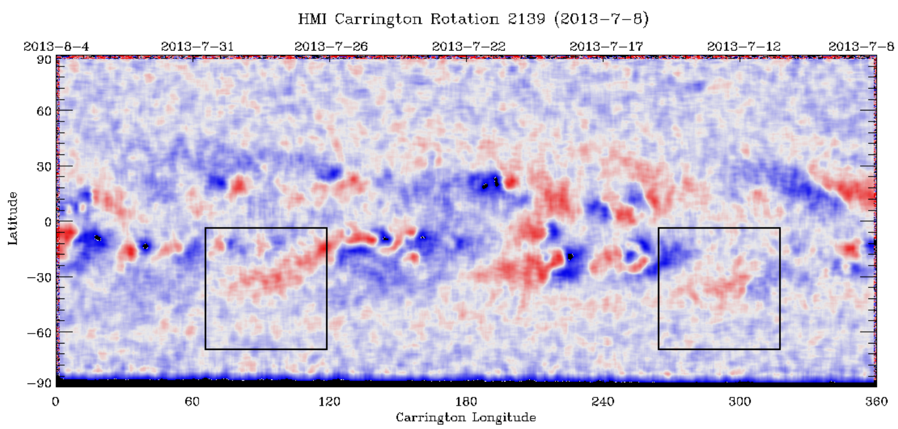
HMI Carrington Rotation 2139 (2013-7-8)
2013-8-4
2013-7-31
2013-7-26
2013-7-22
2013-7-17
2013-7-12
2013-7-8
Latitude
Carrington Longitude

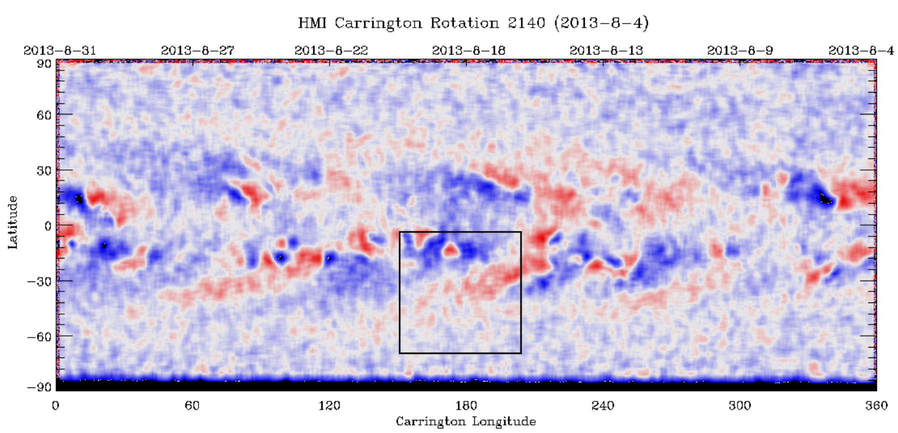
HMI Carrington Rotation 2140 (2013-8-4)
2013-8-31
2013-8-27
2013-8-22
2013-8-18
2013-8-13
2013-8-9
2013-8-4
Latitude
Carrington Longitude

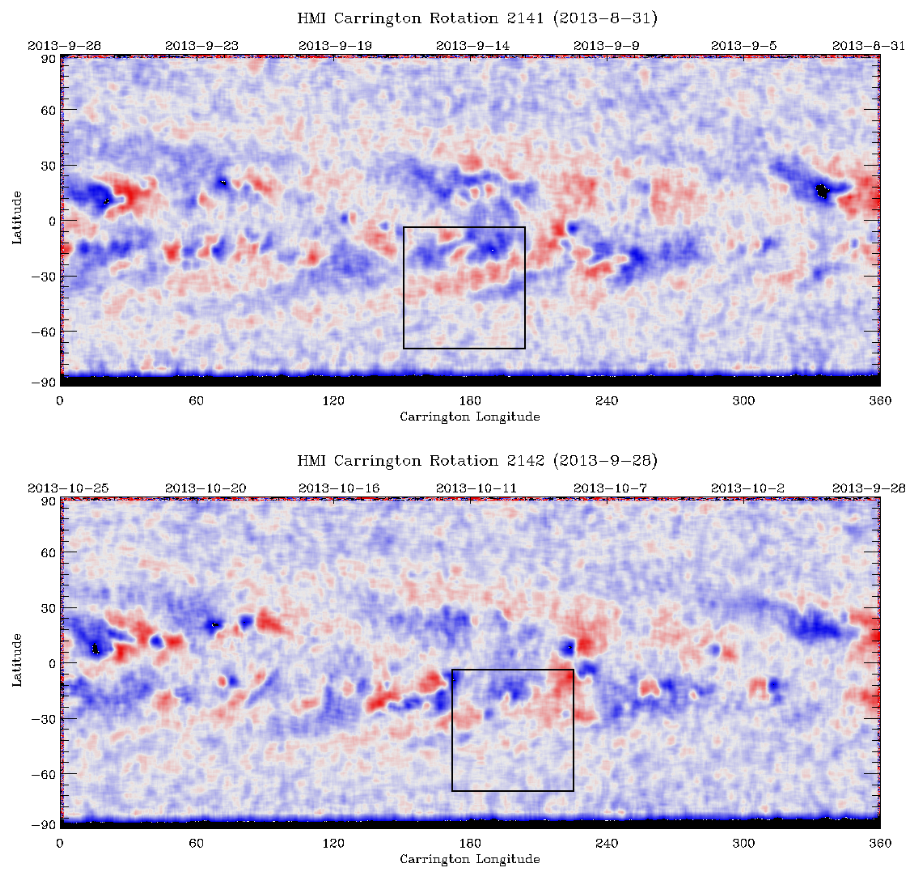

Figure 4.6: HMI Carrington maps from CR 2135 to CR 2142 (March 21, 2013 - October 25, 2013). Blue regions have positive polarity and red regions have negative polarity. In all the maps we see both the poles have blue sign as during this time period northern pole has already changed its polarity while southern pole have yet to change. The black fillings at the north or south pole are due to the B_0-angle that shifts the poles into and out of sight. This image has a cutoff field magnitude of ± 3 gauss and the rectangle boxes shows the region of flux transport.

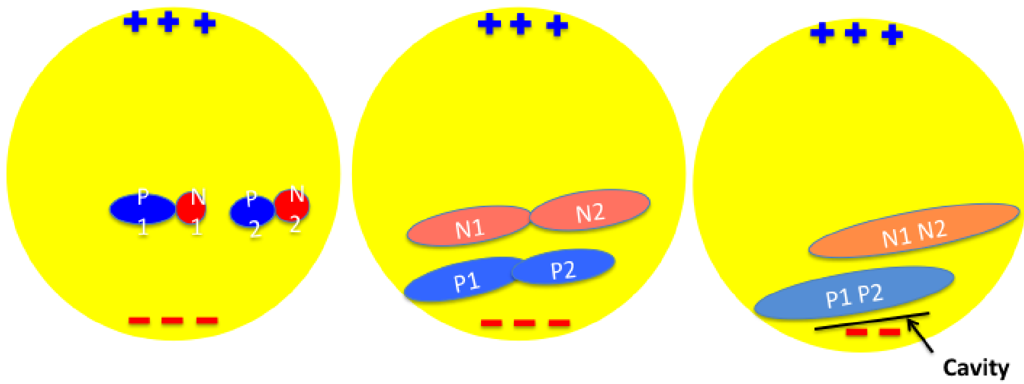

Figure 4.7: Polar crown cavity formation model. a) Multiple active region emerges. b) Trailing polarity of active region diffuses and migrates towards the pole. c) Multiple diffused trailing polarity merge together and migrates towards the pole, flus cancellation continuously happens and PIL formed between trailing flux of multiple decayed active regions and the unipolar magnetic field (polar coronal hole). Red and Blue color represent the positive and negative polarity. The fading of color represents active region getting diffused.

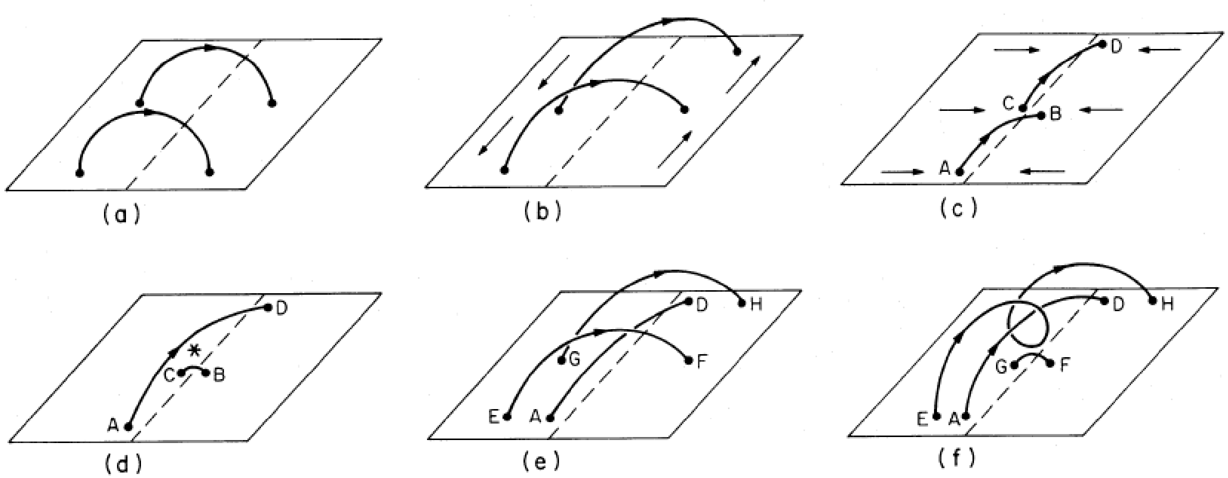

Figure 4.8: Flux cancellation filament model. The flux cancellation happens in a sheared magnetic field. Solar photosphere is represented by the rectangle, and the dashed line is the polarity inversion line separating two opposite magnetic polarity region. Adapted from van Ballegooijen and Martens (1989).

Chapter 5: Comparing models with observations

5.1 Introduction

The previous chapters address the structure, evolution and formation mechanism of cavities. This chapter focuses on the local magnetic structure of the coronal cavities by comparing several existing models with the observations. It is now generally accepted that cavities are flux rope like structures. The relation between the three-part structure of CMEs and the CME eruption has been described by the twisted flux rope topology. While, some of the authors treat the prominence alone as flux rope (Amari *et al.*, 1999; Aulanier and Demoulin, 1998; Priest, Hood, and Anzer, 1989; Rust and Kumar, 1994), others treat the entire three-part structure as the flux rope (Chen, 1996; Gibson and Low, 1998; Guo and Wu, 1998; Low and Hundhausen, 1995). Figure 5.1 shows a sketch, based on observation and modeling of the prominence and cavity, that the cavity magnetic field is a rope of twisted magnetic flux (Low, 1994; Low and Hundhausen, 1995; Wu and Guo, 1997; Wu, Guo, and Wang, 1995). The prominence and cavity are assumed to be two parts of the same magnetic structure and the streamers show the outer boundary of magnetic flux rope model (Gibson and Fan, 2006).

For the present discussion of this chapter we will use the cylindrical flux rope and the spheromac flux rope models to study the magnetic feature of the cavities:

5.2 Flux rope models

5.2.1 Cylindrical flux rope

Fan and Gibson (2006) described the 2.5D axisymmetric isothermal cylindrical flux rope model for the long filament channel. In this model, the twisted toroidal flux tube emerges

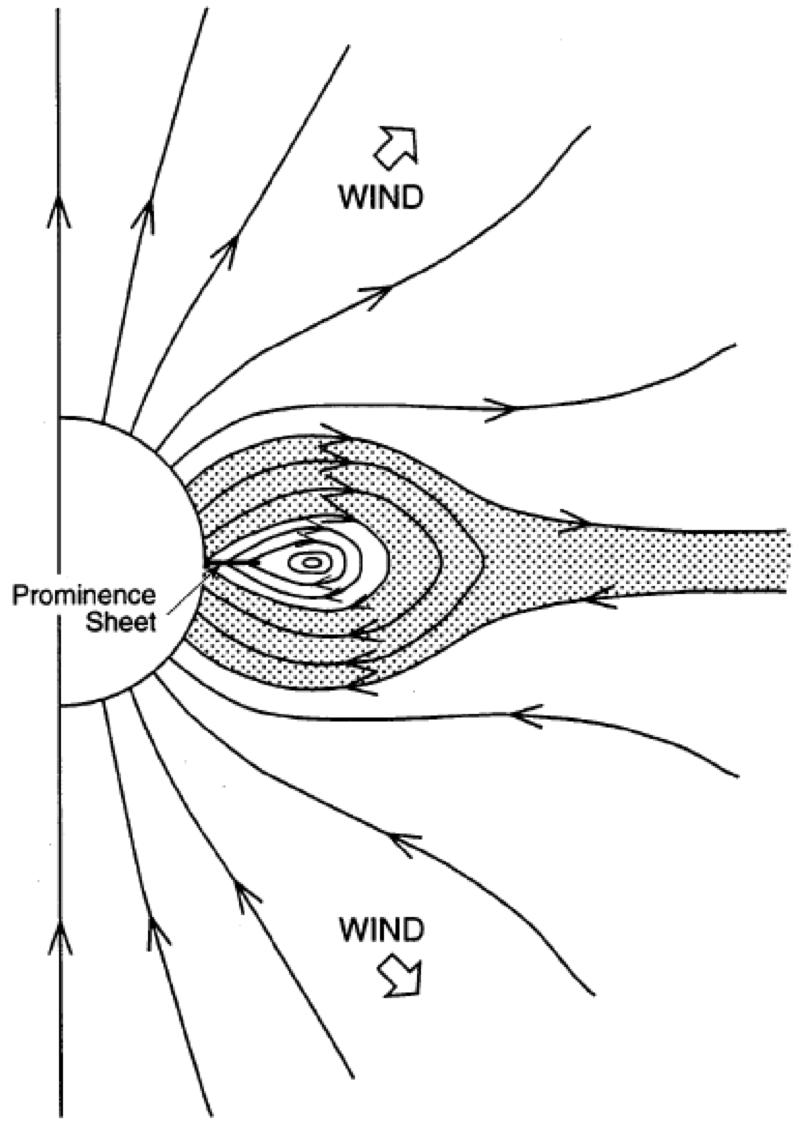

Figure 5.1: Sketch showing prominence and cavity magnetic field in the solar corona. Closed field lines is twisted magnetic flux rope enclosing cavity and a sheet of material suspended inside the flux rope is modeled as prominence. Adapted from Low and Hundhausen (1995).

from the lower boundary into the preexisting potential arcade field seen in Figure 5.2. During the quasi-static stage, a cavity and a central prominence are developed at the volume occupied by the flux rope. Flux rope expands due to its toroidal or axial magnetic field resulting in the development of cavity. The structure also includes still-anchored sheared

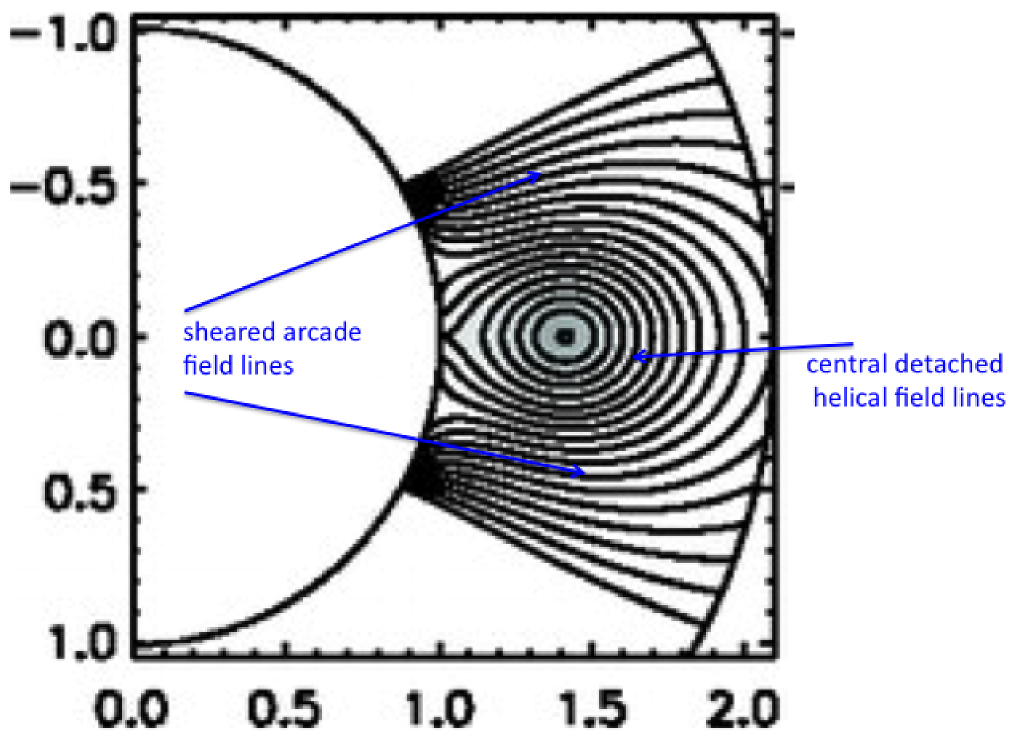

Figure 5.2: Quasi static stage showing still-anchored sheared arcade field lines with a strong axial component along with central detached helical field lines. Adapted from Fan and Gibson (2006).

arcade field lines with a strong axial component along with central detached helical field lines as shown in Figure 5.3. With an extreme twist, there is a loss of equilibrium which leads to an expulsion of the flux rope (Fan and Gibson, 2006; Rachmeler *et al.*, 2013).

Flux rope model as MHD phenomenon is described by the following equations (Fan and Gibson, 2006) .

1) Conservation of momentum:

$$\rho\left[\frac{\partial \mathbf{v}}{\partial t} + (\mathbf{v}\cdot\nabla)\mathbf{v}\right] = \frac{1}{4\pi}(\nabla\times\mathbf{B})\times\mathbf{B} - \nabla p - \rho\frac{GM}{r^2}\hat{r} \tag{5.1}$$

2) Mass conservation:

$$\frac{\partial \rho}{\partial t} + \nabla \cdot (\rho \mathbf{v}) = 0 \tag{5.2}$$

3) Induction Equation:

$$\frac{\partial \mathbf{B}}{\partial t} = \nabla \times (\mathbf{v} \times \mathbf{B}) \tag{5.3}$$

4) Gauss's law of magnetism:

$$\nabla \cdot \mathbf{B} = 0 \tag{5.4}$$

5) Energy Equation:

$$\frac{\partial}{\partial t}(p\rho^{-\gamma}) + (\mathbf{v} \cdot \nabla)(p\rho^{-\gamma}) = 0 \tag{5.5}$$

The isothermal equation of state from Fan (2010) is given below:

$$p = {a_s}^2 \rho, \tag{5.6}$$

The isothermal corona temperature is assumed to be $T_0 = 2$ MK, and thus the isothermal sound speed to be $a_s = 128$ km s^{-1}.

Initially, a hydrostatic isothermal atmosphere is assumed with the density and pressure given by

$$\rho = \rho_0 exp\left(\frac{-R_\odot}{H_{p0}}\left(1 - \frac{R_\odot}{r}\right)\right) \tag{5.7}$$

$$p = \frac{RT_0\rho}{\mu} \tag{5.8}$$

The base of corona H_{p0}=60 Mm and the base density $\rho_0 = 8.365 \times 10^{-16}$ g cm^{-1}. A pre-existing potential arcade field is present in the initial atmosphere, whose normal field $B_r(0, \theta, \phi)$ at the lower boundary is given by

$$B_r(0,\theta,\phi) = \frac{1}{R_\odot^2 \sin\theta} \frac{dA_s(\theta)}{d\theta}, \tag{5.9}$$

where,

$$A_s(\theta) = \begin{cases} 0, & \frac{5}{12}\pi < \theta < \frac{\pi}{2} - \theta_t - \theta_a. \\ -\frac{\theta_a}{\pi} \sin\theta_p B_0 R_\odot^2 \left[1 - \cos\left[\frac{\pi}{\theta_a}\left[\theta - \left(\frac{\pi}{2} - \theta_a - \theta_t\right)\right]\right]\right], & \frac{\pi}{2} - \theta_t - \theta_a < \theta < \frac{\pi}{2} - \theta_t. \\ -\frac{2\theta_a}{\pi} \sin\theta_p B_0 R_\odot^2 & \frac{\pi}{2} - \theta_t < \theta < \frac{\pi}{2} + \theta_t. \\ -\frac{\theta_a}{\pi} \sin\theta_p B_0 R_\odot^2 \left[1 + \cos\left[\frac{\pi}{\theta_a}\left[\theta - \left(\frac{\pi}{2} + \theta_t\right)\right]\right]\right], & \frac{\pi}{2} + \theta_t < \theta < \frac{\pi}{2} + \theta_t + \theta_a. \\ 0, & \frac{\pi}{2} + \theta_t + \theta_a < \theta < \frac{7}{12}\pi. \end{cases} \tag{5.10}$$

in which θ_a=0.05 rad, θ_t=0.0432 rad, $\theta_p = \frac{\pi}{2} - \theta_t - \frac{\theta_a}{2}$ and peak arcade field strength B_0=20 G. Thus, the peak Alfvén speed at an arcade field footpoint is $v_{A0} = \frac{B_0}{\sqrt{4\pi\rho_0}}$=1951 km s^{-1}, which is factor of 10 times greater than the isothermal sound speed a_s = 128 km s^{-1}.

At the domain's lower boundary $r = 1\ R_\odot$, a twisted toroidal flux tube $\mathbf{B_{tube}}$ whose toroidal axis lies in the equatorial plane is kinematically transported into the domain by specifying at the $r = 1\ R_\odot$ boundary a time dependent transverse electric field $\mathbf{E}_\perp|_{r=R_\odot}$ corresponding to the upward advection of the flux tube at a velocity $\mathbf{v}_0$ is given by

$$\mathbf{E}_\perp|_{r=R_\odot} = \hat{r} \times \left[\left(-\frac{1}{c} v_0 \times \mathbf{B_{tube}}(R_\odot, \theta, t)\right) \times \hat{r}\right] \tag{5.11}$$

v_0 is constant over the area through which the emerging tube intersects the lower boundary and at other places in the lower boundary it is zero.

This model $\mathbf{B_{tube}}$ of specifies $\mathbf{E}_{\perp}|_{r=R_{\odot}}$ as an axixymmetric torus defined by its own local spherical polar coordinate system (r', θ', ϕ').

$$\mathbf{B_{tube}} = \nabla \times \left(\frac{A\left(r', \theta'\right)}{r' \sin\theta'} \hat{\phi}' \right) + B_{\phi'}\left(r', \theta'\right) \hat{\phi}' \tag{5.12}$$

where,

$$A\left(r', \theta'\right) = \frac{1}{2} q a^2 B_t \exp\left(-\frac{\bar{w}^2\left(r', \theta'\right)}{a^2} \right) \tag{5.13}$$

$$B_{\phi'}\left(r', \theta'\right) = \frac{a B_t}{r' \sin\theta'} \exp\left(-\frac{\bar{w}^2\left(r', \theta'\right)}{a^2} \right) \tag{5.14}$$

Here, (r', θ', ϕ') is the origin of the local coordinate system located at $\mathbf{r} = \mathbf{r}_0 = (r_0, \theta_0, \phi_0)$. a is the minor radius of the tube and $\bar{w}$ is the distance to the curved axis of the torus. $\mathbf{B_{tube}}$ used for specifying $\mathbf{E}_{\perp}|_{r=R_{\odot}}$ is the solution of the induction equation $\frac{\partial \mathbf{B_{tube}}}{\partial t} = \nabla \times (\mathbf{v} \times \mathbf{B_{tube}})$ with the initial $\mathbf{B_{tube}}(r, \theta, t = 0)$ given above. Moreover, the mass flux $\rho_0 v \sin\theta$ inflows through the lower boundary to the area where emerging tube intersects the boundary. The side boundaries are perfectly conducting walls and outward-extrapolating boundary condition is used in the outer radial boundary that allows plasma and magnetic field to flow through Fan and Gibson (2006).

Figure 5.3 is a 2.5D axisymmetric cylindrical flux rope isothermal model described in Fan and Gibson (2006). The system is in quasi-static until time $t = \frac{114 R_{\odot}}{v_{A0}}$. After which, if the flux rope emergence is continued then it leads to an eruption.

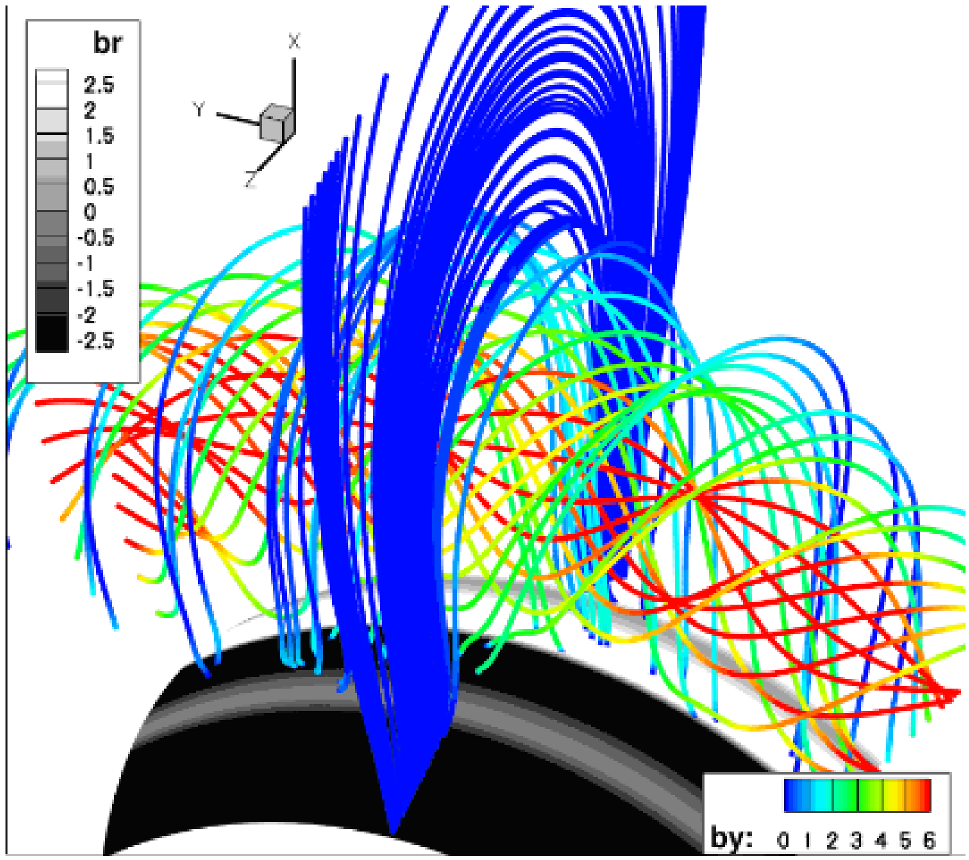

Figure 5.3: 2.5 D axisymmetric cylindrical flux rope. Adapted from Rachmeler *et al.* (2013).

5.2.2 Spheromac flux rope

The second model that I used is the spheromac model. The spheromak magnetic flux rope model is based on solutions to the MHD equations in full magnetostatic equilibrium (Gibson and Low, 1998). This Gibson-Low model describes the three-part structure as due to a CME magnetic field containing a flux rope of helical fields in the CME cavity. This model explains that the cavity arises from strong internal magnetic pressure and twisted field lines winding about an axial field line that is partially detached from the photosphere (Low, 1996). The prominence is supported in the dips of the magnetic field, and the front or helmet streamer is the interface between the flux rope system and surrounding, more simply sheared arcade field (Low, 1996; Low and Hundhausen, 1995).

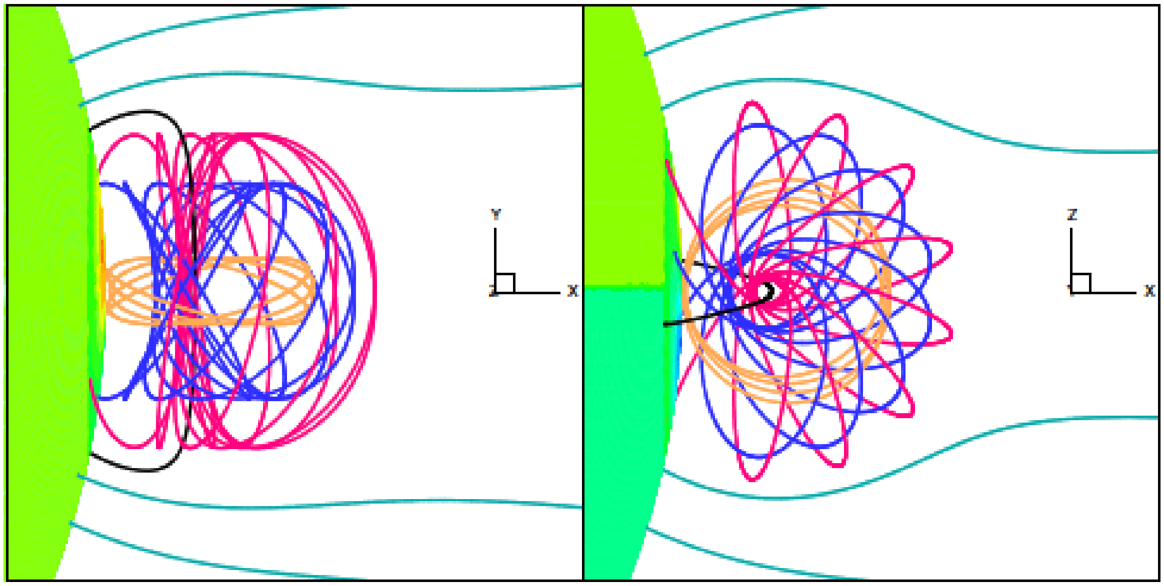

Figure 5.4: GibsonLow spheromak magnetic flux rope model. Red, purple, orange and black field lines traces the model. The top two panels are (a) View perpendicular to the rope axis, and (b) view along the rope axis. Black thick line traces the flux rope axis in the dips of magnetic field and prominence material sits below it. Adapted from Dove *et al.* (2011).

A spheromak is a toroidal rope of twisted flux encircling the axis of symmetry. It looks more like doughnut shape. The spheromak is the spherical limit of doughnut hole collapsed onto a point along the axis of symmetry (Dove *et al.*, 2011; Gibson and Low, 1998). Spheromak magnetic topology describes the magnetic properties of both quiescent prominences and their cavities.

5.3 Results

5.3.1 Interpreting flux rope model with CoMP

The information about the magnetic field can be obtained by studying linear and circular polarization signals of appropriate infrared coronal emission lines. I used data from the Coronal Multi-Channel Polarimeter (CoMP, Tomczyk *et al.* (2008)) installed at the Mauna Loa Solar Observatory (MLSO) in Hawaii on October 2010, that makes daily observations of the lower corona with a field of view in the lower corona from 1.04 to 1.4 solar radii. It is also designed to obtain information about the plasma density and motion. The CoMP instrument is a combination of a polarimeter and a narrowband tunable filter capable of measuring the Doppler shift and complete polarization state (characterized by the Stokes parameters I, Q, U, V) of the Fe XIII 1074.7 and 1079.8 nm infrared coronal emission lines and the chromospheric 1083 nm He I line.

The strength of the total linear polarization ($L = \sqrt{Q^2 + U^2}$) is dependent on θ, the angle between the line of sight (LOS) and the direction of the local magnetic field, i.e., $L \propto \sin^2\theta$. Linear polarization signal is strongest when $\theta = 90°$, i.e., when the magnetic field is in the perpendicular to the line of sight, or in the plane of sky (POS). Linear polarization signal is weakest when $\theta = 0°$ or $180°$, i.e., when the magnetic field is parallel to the line of sight (Rachmeler, Casini, and Gibson (2012) and references therein).

In addition, to CoMP data, we used EUV images from the Atmospheric Imaging Assembly (AIA) instruments on board the Solar Dynamics Observatory (SDO). In AIA 193 Å cavities are clearly visible. The cavity's depleted center, boundary, and the outer bright streamer are clearly defined in this passband (see Figure 1 in Chapter 2).

Cylindrical flux rope

Figure 5.5 consists of flux rope model (top left), LOS-integrated Stokes L/I for forward-calculated 3D flux-rope model with the contours showing the current density in the simulations (top right), cavity observed in AIA 193Å (bottom left), and LOS-integrated L/I for CoMP observations. Diamond shape is the center of the cavity. We can notice that cavity observed in AIA 193 Å when observed in CoMP instrument have a characteristic Fe XIII linear polarization signature (bottom right). This signature can be explained as arising from an arched magnetic flux rope with an axis oriented along the line of sight (shown here in POS, top left image). When integrated along the line of sight, the flux rope magnetic field at the van Vleck angle, i.e., around 54.7° with respect to a solar radial, the light becomes

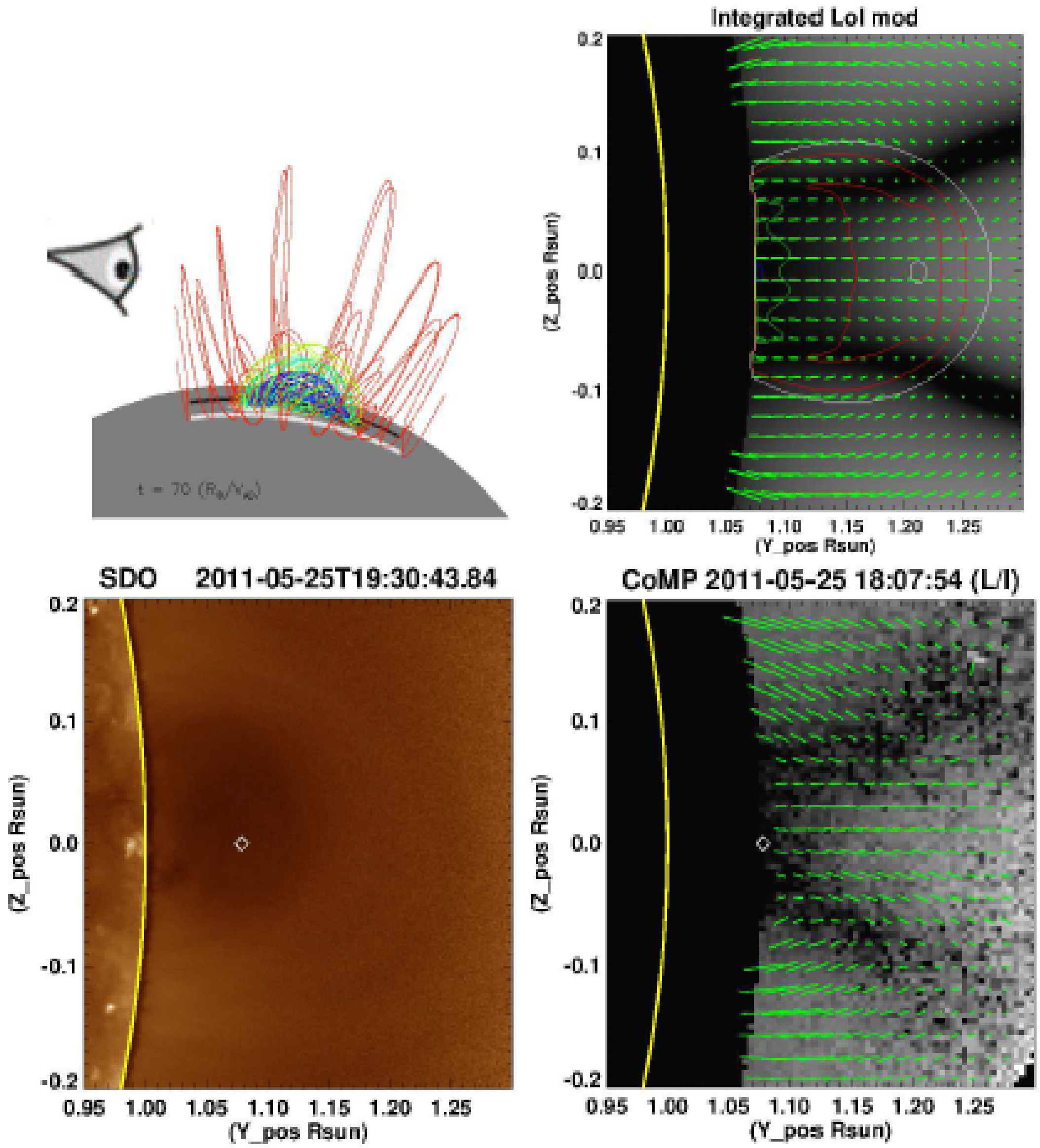

Figure 5.5: Cylindrical Flux rope model. Top left: Flux rope field lines. Top right: linear polarization model integrated along the line of sight. Bottom left: SDO AIA 193 Å observation. Bottom right: linear polarization observation in CoMP. White diamond is the cavity center in different types of observation. Adapted from Bąk-Stęślicka *et al.* (2013).

unpolarized, and linear polarization becomes null (or goes to zero). Figure 5.5 top right panel is forward-modeled linear polarization from cylindrical flux rope isothermal model simulation. The dark V-shaped in the Figure 5.5 both right panel figure (forward model and observation) are due to the van Vleck effect. The darker central region in L/I is due to the stronger LOS field in this region, reducing the linear polarization signal (Rachmeler *et al.*, 2013).

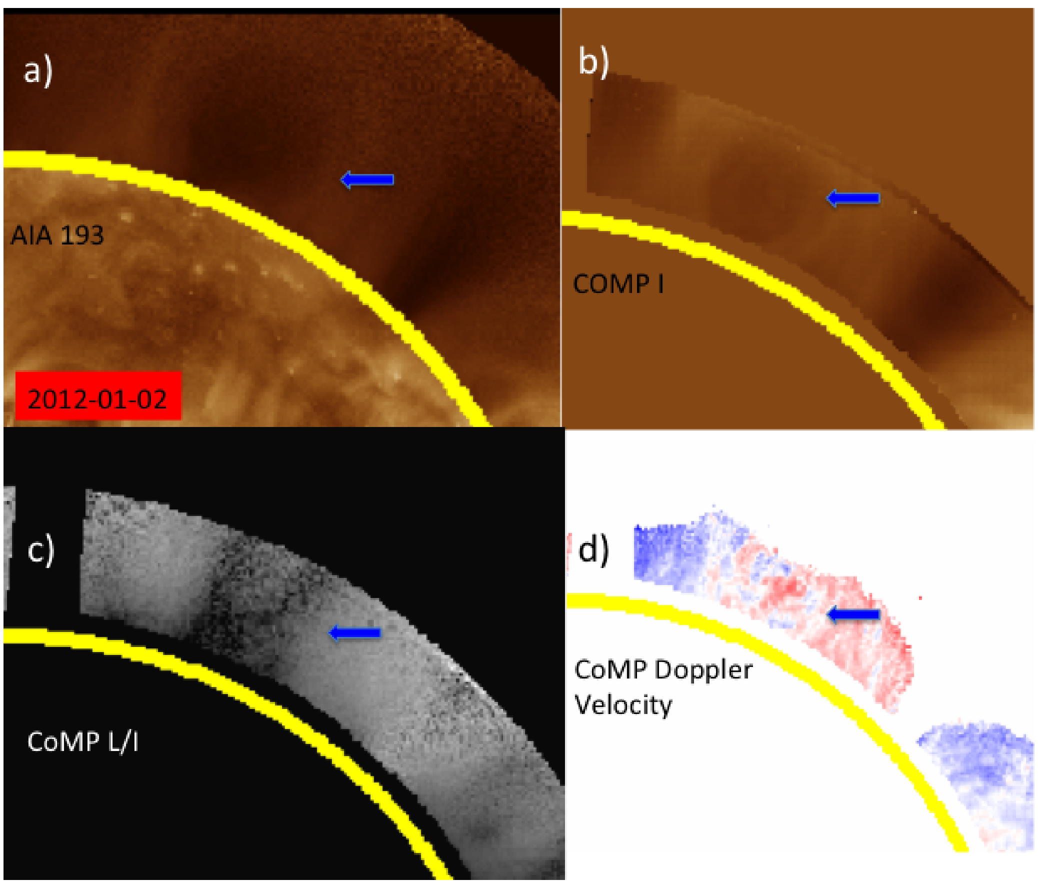

Figure 5.6: AIA and CoMP observation of cavity appeared on January 02, 2012 in the north-western limb. (a) AIA 193 Å (b) CoMP Intensity (c) CoMP observed linear polarization (L/I) and (d) Doppler velocity from CoMP observation.

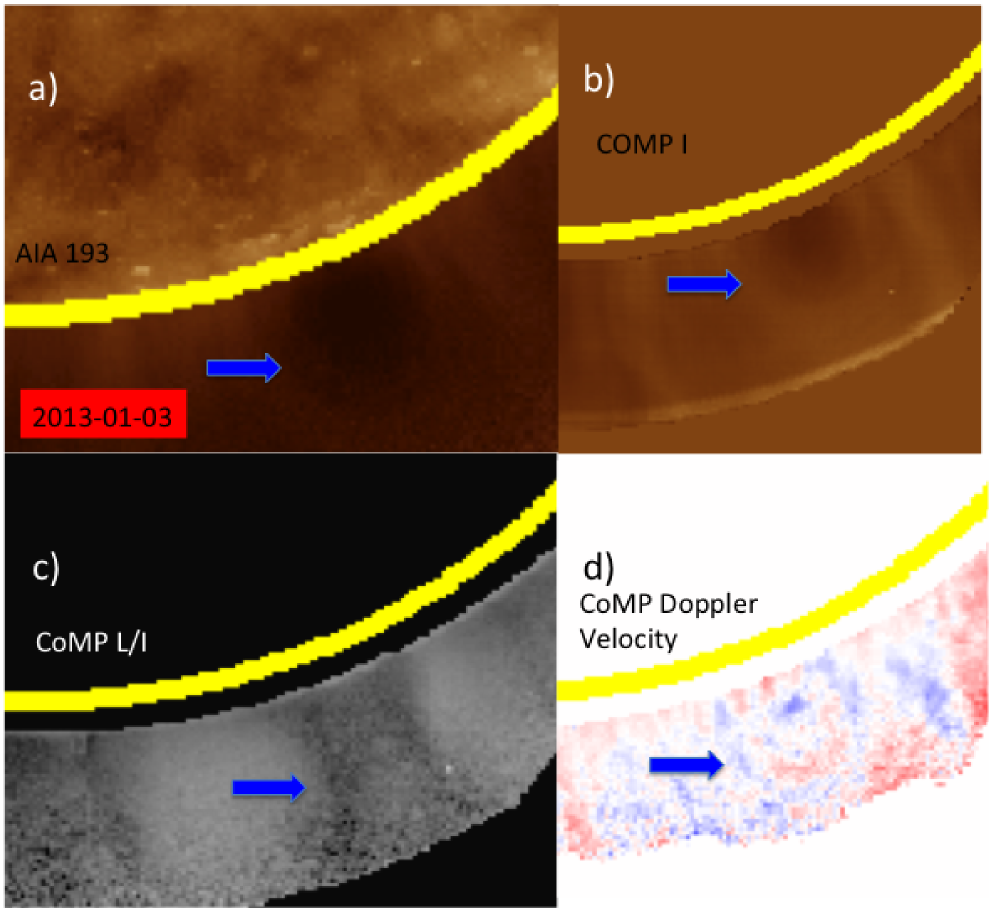

Figure 5.7: AIA and CoMP observation of cavity appeared on January 03, 2013 in the south-western limb. (a) AIA 193 Å (b) CoMP Intensity (c) CoMP observed linear polarization (L/I) and (d) Doppler velocity from CoMP observation.

I took a sample of three random cavities that were observed in CoMP observation. The purpose was to validate which flux rope model best fits the observation. Figures 5.6, Figure 5.7, and Figure 5.8 are three cavities (pointed by blue arrow) selected for our study. The four panels of each figure are (a) cavity observed in AIA 193 Å wavelength (b) CoMP Intensity (c) CoMP observed linear polarization (L/I) and (d) Doppler Velocity from CoMP observation. The dark core in the middle of cavity observed in linear polarization (L/I) (see Figures 5.6c, Figure 5.7c, and Figure 5.8c) is due to the flux-rope axis being oriented along the LOS, combined with Van Vleck inversions in the flux rope lower part. The V or U-shape

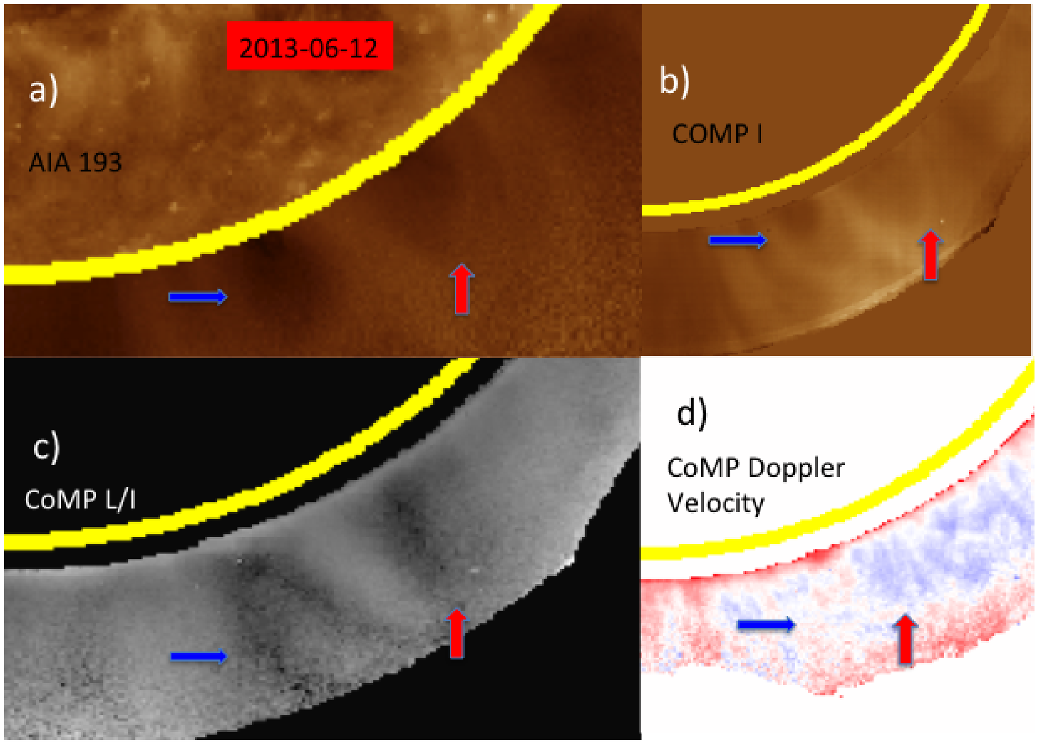

Figure 5.8: AIA and CoMP observation of cavity appeared on June 12, 2013 in the south-western limb. (a) AIA 193 Å (b) CoMP Intensity (c) CoMP observed linear polarization (L/I) and (d) Doppler velocity from CoMP observation.

in linear polarization structure is formed due to the Van Vleck effect in the surrounding arcade and top of the flux rope (Bąk-Stęślicka *et al.*, 2013). If the cavity is observed in higher then flux rope axis is also at a higher height. Due to this extended feature is not observed in CoMP field of view, making the structure look like U-shape. In Figure 5.6 (c) and Figure 5.7 (c), an almost U-shape structure is observed with central dark core. The flux rope may have a high axis and due to small CoMP field of view, the extended structure is not observed. Whereas in Figure 5.8 (c) a nice V-shape structure is observed indicating flux rope has a low axis, implying cavity has lower center or smaller in size.

A bulls-eye pattern with concentric circles is only seen in Figure 5.7 (d) and Figure 5.8 (d). The red arrow pointing to the cavity in Figure 5.8 does not have a clear linear polarization signature nor a signature in Doppler velocity. A Bulls-eye pattern is more common in larger cavities which do not have a V-shape pattern in the linear polarization due to the small field of view of CoMP (Bąk-Stęślicka *et al.*, 2013). Figure 5.8 (d) does not show any concentric circle signature as the cavity size is smaller or the cavity center lies below the CoMP chronograph occulter. The signatures observed from CoMP are consistent with a flux rope topology supporting that the cavities are a flux rope structure.

Spheromac flux rope

Figure 5.4 is a model generated by Dove *et al.* (2011) from analytic MHD models of spheromak-type magnetic flux ropes. Figure 5.4 (a) shows the side view of the model of twisted field lines with the axis parallel and Figure 5.4 (b) with that axis perpendicular to the plane of the figure. Prominence is the relatively weak twisted field running parallel to the solar surface (black line). The central orange line about thick black line is the poloidal winding about its axis, and the outer red line winding about the orange and blue lines are the toroidal winding about a ring encircling the central axis.

The linear polarization is sensitive to POS magnetic field, so when the magnetic field winds around a central line-of-sight-oriented axis a polarization ring may occur. Early CoMP observations of a prominence cavity made by Dove *et al.* (2011) showed such a structure. A dark core is clearly visible at the location of the flux-rope axis in Figure 5.9 (a) and (b) and it is dark due to the LOS field associated with the axis. The bright ring surrounding the axis is due to the plane of sky field in the flux rope. A darker ring (fainter than axis as B is only aligned with the LOS in a relatively narrow volume of space) at the edge of the spheromak bubble. In our studies, the ring structure were not observed in the CoMP data.

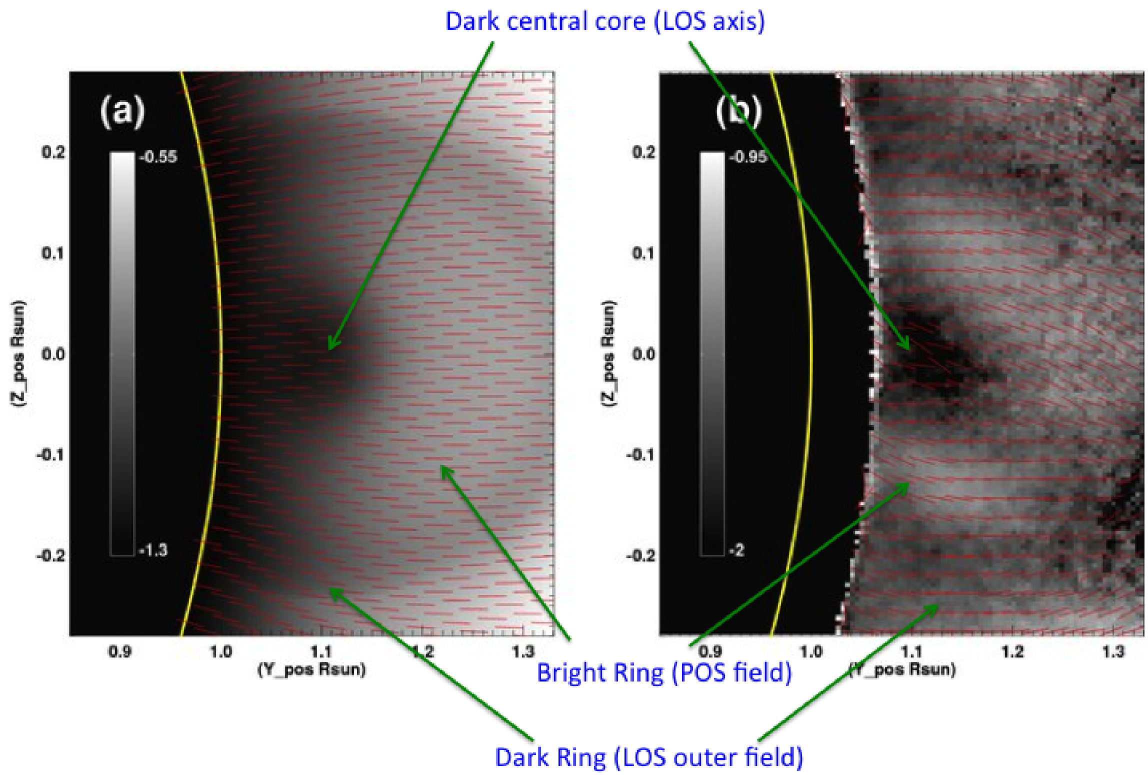

Figure 5.9: The two panels are the (a) LOS-integrated Stokes P/I forward-modeled configuration and, (b) CoMP observations of 2005 April 21 cavity that appeared on the southwest limb. Adapted from Dove *et al.* (2011).

5.3.2 AIA observation and Forward modeling

The FORWARD model incorporates a set of MHD models. Forward modeling is a process by which a model-defined 3D distribution of coronal plasma properties (density, temperature, velocity, and magnetic field) is calculated, and line-of-sight integrations specific to a given coronal observable are performed (Fuller and Gibson, 2009; Gibson *et al.*, 2010; Schmit and Gibson, 2011). Forward modeling enables solar observations to be interpreted based on observable properties of specific magnetic models topologies (Dove *et al.*, 2011). We used existing the Forward model presented in Bąk-Stęślicka *et al.* (2013) to interpret the cavities on CoMP observations. I also used a publicly available FORWARD model to model one cavity (Cavity C211347177N) in AIA 193Å presented in Chapter 2.

I used the Cavmorph module to model cavity C211347177N. Cavmorph is a morphological model of a solar streamer and cavity that specifies the 3D distribution of density and temperature that can be fit to observations. The geometric measurements of C211347177N used as input to the model are listed in Table 5.3.2, along with the Cavmorph variable name. We assumed an isothermal corona of 1.6 MK, however, we used the cavity temperature of 2.8 MK calculated from the DEM in Chapter 2. We used the model default density value which is a scaling factor times a radial profile of the streamer (defined by Gibson *et al.* (1999)) and a coronal hole density defined by Guhathakurta *et al.* (1999). In this model, we made the streamer sufficiently large so that the cavity dominates the volume of interest. Figure 5.11 is the output of the Cavmorph model after entering all the inputs listed in Table 5.3.2. The dark feature is the modeled cavity, and two green vertical lines define the boundary of the cavity. Figure 5.11 shows our best-fit forward-modeled AIA emission for the west limb and looked similar in the shape with the observation in Figure 5.10, implying that cavity may be a flux rope structure.

Table 5.1: Cavmorph Geometrical Parameters for the Cavity and Streamer

Parameter	Value
Cavity and streamer central colatitude (THCS and CAVTOP-TH)	47°
Streamer central longitude (PHCS)	177°
Angle the streamer neutral line makes to equator (MANG)	−8°
Streamer half length at photosphere (PHOTOLENGTH)[1]	1000°
Streamer half width at photosphere (PHOTOWIDTH)[1]	1000°
Streamer half width at streamer top (CSWIDTH)	3°
Streamer current sheet height (CSHEIGHT)	1.27 $R_\odot$
Cavity half length (CAVLENGTH)	85°
Cavity width (CAVWIDTH)	0.18 $R_\odot$
Cavity top radius (CAVTOP-R)	1.27 $R_\odot$
Cavity height (CAVHEIGHT)	0.27 $R_\odot$

[1]Value set to push streamer out of volume of interest.

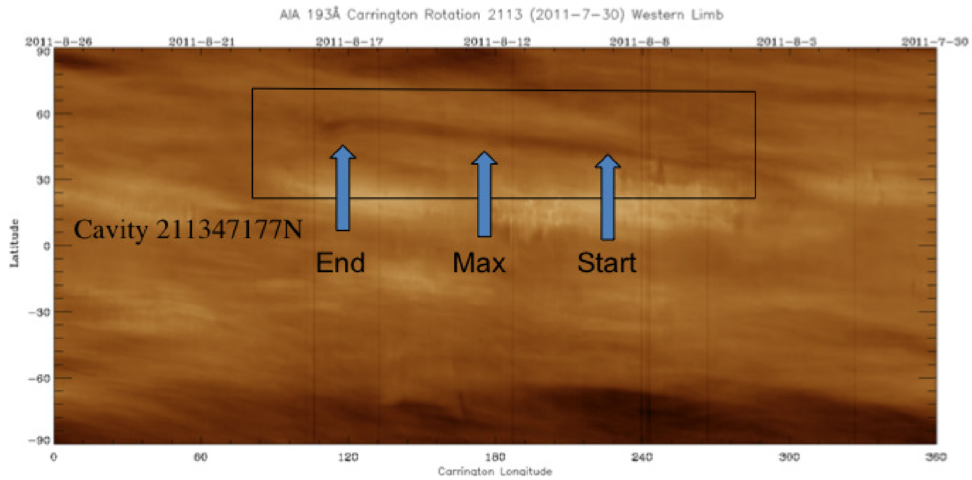

Figure 5.10: Cavity C211347177N displayed in AIA 193 Å western limb-synoptic map. The box encloses the cavity. The three arrows indicate the three positions of cavity: the fully developed starting location, its maximum width, and just before disappearing.

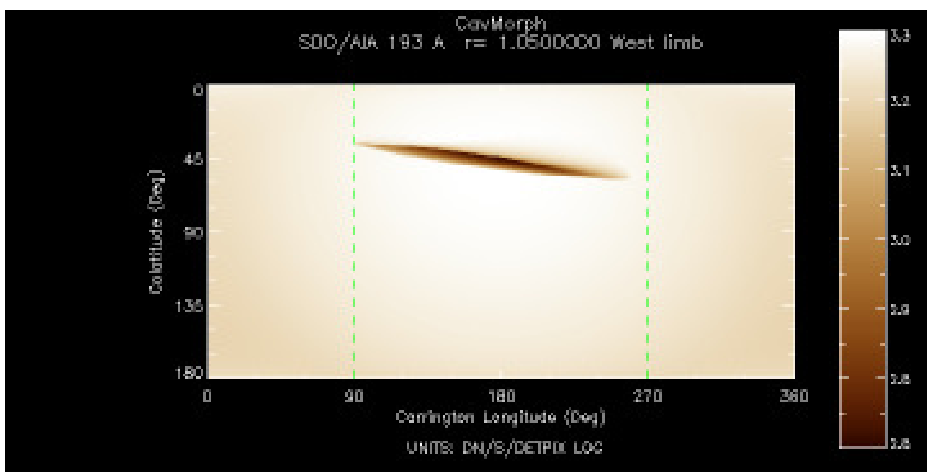

Figure 5.11: Forward-modeled line-of-sight AIA 193 Å Carrington map from west limb viewpoint at 1.05 $R_{\odot}$. The dark thread like structure is the cavity.

5.4 Conclusion and Discussion

Using a FORWARD model we were able to reproduce the AIA observations, implying that this cavity is a flux rope structure. Moreover, measurements of the prominence cavity obtained by the CoMP instrument indicate characteristic signals in linear polarization consistent with twisted magnetic flux ropes. None of the three observations showed the"polarization ring" structure. In two cases, an almost U-shape structure with the central dark core is observed in the linear polarization of CoMP data and a bulls-eye pattern in LOS velocity is observed. The U-shape structure may observe when flux rope may have a high axis and due to small CoMP field of view the extended structure is not observed. Whereas, in one case a V-shape is observed with no bulls-eye patterns in LOS velocity indicating the cavity is smaller in size. These signature are well-explained by the Fan and Gibson (2006) cylindrical flux rope model. Bąk-Stęślicka *et al.* (2013) interpreted similar observations using forward modeling to calculate synthetic CoMP-like data and explained that such signatures are well-explained by a flux rope topology. They conclude that the arched cylindrical magnetic flux rope is an appropriate model for most polar crown prominence cavities.

In the Fan and Gibson (2006) cylindrical flux rope model, a twisted toroidal flux tube emerges from the lower boundary of the preexisting potential arcade field. However, our study in Chapter 4 shows that the flux rope is formed by the flux cancellation. There was no flux rope emergence. Our result disagrees regarding how flux rope formed from Fan and Gibson (2006). However, we agree that the cavity is a flux rope.

Chapter 6: Summary and Future plan

This research has produced new and important results in our understanding of the global structure of coronal cavities. Four topics were covered in this thesis. The first topic was the detection and measurement of the coronal cavities using limb synoptic maps. The second topic covers statistical studies of the geometric structure and underlying source regions using a surface magnetic field. The third topic was the study of the formation of the polarity inversion line of a circumpolar crown cavity, which lasted for several Carrington Rotations. The final topic was the description of an existing model of the cavities, which was used to compare with the observations. The main result of each topic is summarized in as follows.

1) In Chapter 2, I described the development of a limb synoptic map method, a new approach to identify coronal cavities and further study their properties. Limb synoptic maps are a convenient way to identify a cavity. More important, the length can be measured in terms of both days and solar radii. Coronal cavity C211347177N was used in this chapter to illustrate such a study. The overall 3-D topology of cavity C211347177N is a long tube with an elliptical cross-section. Moreover, an elongated diffuse bipolar region is observed underneath the cavity in the photosphere. The polarity inversion line is consistent with the axis of the cavity.

2) In Chapter 3, I present a survey of 429 coronal cavities found between May 2010–Feb 2015 using SDO/AIA limb synoptic maps. The largest number of EUV coronal cavities have been found using the same technique. The catalog is published in a public website. Correlations between the height, width and length of the cavities were examined. The result showed that around 38% of cavities were prolate, 27% oblate and 35% circular in shape. The lengths of the cavities ranged from 0.06-2.9 $R_{\odot}$. When a cavity is longer than 1.5 $R_{\odot}$ it has a narrower height range (0.1-0.3 $R_{\odot}$), whereas when the cavity was shorter than 1.5 $R_{\odot}$, it has a wider height range (0.07-0.5 $R_{\odot}$). The overall 3-D topology of long stable cavities

can be characterized as a long tube with an elliptical cross-section. It was also noticed that the circular and oblate cavities are longer in length than prolate cavities. I also studied the physical mechanisms behind the cavity drift towards the pole and found it to be tied to the meridional flow. Finally, by observing the underlying source regions using SDO/HMI surface magnetic field observations, a clear cavity belt was noticed, defined by the location of polar crown filament/cavity and evolving with the solar cycle. I showed that the cavity belt migrated towards higher latitude with time and the cavity belt disappeared after the polar magnetic field reversal. This result shows that cavity evolution provides new insight into the solar cycle.

3) In Chapter 4, I studied the underlying magnetic field of the circum-polar crown cavity (March 21, 2013- October 25, 2013), which lasted for several Carrington Rotations. This kind of study is done for the first time for coronal cavities. The result suggests two necessary conditions to form long stable polar crown cavities: 1) The underlying polarity inversion line of cavities should be formed between the trailing part of decayed active regions and the unipolar magnetic field in the pole. 2) The long life of cavities was due to adding of trailing flux from the multiple newly transported active region.

4) In the last Chapter 5, I described the exciting model of cavities. Several proposed mechanisms have been to model the cavity magnetic structure and evolution, with several models and numerical MHD simulations and solar observations to support theories. It is also now generally accepted by the community that cavities are flux- rope-like structures. The information about the magnetic field can be obtained by studying linear and circular polarization signals of certain infrared coronal emission lines. I used CoMP data and analyzed linear and circular polarization signals using existing forward data to distinguish characteristics of flux rope models. Moreover, I used publicly available FORWARD model to model the observations presented in Chapter 2. The result from the AIA model, and the signatures observed from CoMP data for three case study are consistent with a flux rope topology supporting the idea that the cavities are flux rope structure.

This thesis has addressed three important scientific questions in solar physics. (1) What is the 3-D structure of coronal cavities? (2) Can the cavities act as a probe to study the polar magnetic field reversal at solar maximum? (3) How are polar crown cavities formed and what determines their stability? However, there are still so many questions unanswered such as: (i) How do cavities and magnetic field evolve over time, and can cavity properties be used to predict eruptions? (ii) How are cavities shaped by the local magnetic field? (iii) Why do the prominences that follow the pole reversal have cavities more often and can cavity observations be used to predict the solar cycle?

Future work will be to address above several important scientific questions. To address those issues, I propose to perform the following activities:

1) Extend our cavity catalog back to 1996 using SOHO/EIT data. An extended catalog will give us an access to a database containing nearly 1000 cavities spanning two 11−year sunspot cycles. A major part will be to develop an automated method to detect cavities that will replace the current time-consuming manual detection. The automated detection will detect the boundary of cavity over the limb synoptic map taking advantage of the prominence map (AIA 304 Å) which confirms the dark region that we see in the AIA 193 Å is a cavity rather than a coronal hole region. From the catalog, we will obtain information (i.e. length, width, heigh, shape) of each cavity. Then we will correlate these information with eruptions to discern any patterns that will help predict those eruptions in the future. The study of the evolution of cavities will connect to the release of the magnetic energy they store in CMEs and will help to understand cavity properties better.

2) Extend the work described in Chapter 3. The results in Chapter 3 showed that the length of the cavity is related to its lifetime, so longer cavities are also longer-lived. With increasing cavity length, the height range decreases. This result may imply that high-lying long cavities are unstable and subject to eruption. So, several questions arise from these results: Why do long cavities tend to be smaller in height and what makes it stable for so long? Is it related to the structure of the magnetic field? Does it mean that long cavities do not have enough magnetic shear to erupt? Do long stable cavities have low magnetic

flux? Understanding the stability/instability mechanism of the cavity and prominence is one major future work. It is, therefore, important to study the magnetic configuration as well as the physical mechanisms that lead to eruptions.

In the corona, the magnetic pressure is higher than the plasma pressure, i.e., the magnetic pressure parameter $\beta < 1$ and the resulting magnetic field is force free. Direct observations of the coronal magnetic field are difficult to obtain and are still rare. The vector field measurements are made in the photosphere where magnetic field is not force free, therefore, we will rely on model extrapolations of photospheric magnetic field measurements (Mackay and Yeates, 2012). There are several techniques that have been developed to model the coronal field of active regions such as the Potential Field Source Surface (PFSS) Model, the Linear Force Free field (LFFF), and the NonLinear Force Free Field (NLFFF). The goal is to understand the magnetic structure of the cavity and for this I propose to use an NLFFF model in which the electric current density is parallel to the magnetic field. There are several methods for numerically computing nonlinear force free fields such as the flux rope insertion method by van Ballegooijen (2004), optimization method by Wiegelmann *et al.* (2007), or the force-free electrodynamics method by Contopoulos, Kalapotharakos, and Georgoulis (2011). I propose to use van Ballegooijen (2004) "flux insertion" method for calculating NLFFF model to extrapolate the coronal magnetic field over selected coronal cavities. This method involves inserting a magnetic flux rope into a NLFFF model, where axial flux ϕ_{axi} and poloidal flux F_{pol} are used as free parameters (Su *et al.*, 2009). The goal is to model several different cases of cavities such as i) equatorial vs polar, ii) erupting vs non erupting, iii) short lived vs long lived, and iv) at different times in the solar cycle (starting, maximum, declining, minimum). From the magnetic field model we will be able to calculate electric current, helicity, free energy and more importantly decay index which measures the rate at which the overlying magnetic field falls off. This study will provide crucial information for determining which cavities are magnetically stable and which are likely to erupt.

3) Perform a comprehensive study of the solar cycle evolution of coronal cavities studied

in Chapter 3. Li *et al.* (2008) studied full-disk activity cycle and separated filaments into two groups: high latitude (above 60°) and low latitude (below 40°) and concluded that there were three kinds of latitudinal migration: (1) a poleward drift of high latitude filaments when solar activity begins to increase from solar minimum, (2) an equatorward drift of low latitude filaments at the same time, and (3) after the polar reversal an equatorward drift from poles to middle latitudes (about 50°). So the question is: Do we see the same signature in the cavities we have studied? Chapter 3 results showed a remarkable correlation between the latitude of the cavity belt and migration of the magnetic field to the poles (see Figure 3.6). We only see a poleward drift of cavities at high latitude, but there is not yet any sign of equatorward drift at low latitudes nor equatorward drift away from the poles after the polar reversal. However, we need at least a complete solar cycle of cavity data in order to fully understand the relationship of the cavity belt to the solar cycle. Understanding the cavity belt evolution with solar cycle is one major objective of this future study. I propose to use cavity data that we will gather over two solar cycles to fully understand the relationship between the cavity belt and the solar cycle.

Sometimes cavities are observed without prominences, and sometimes prominences are observed without cavities, so by combining location information about both cavities and prominences and comparing with the magnetic field, we will get a comprehensive view of the solar cycle progression. For this, we will compare extended cavity catalog data with the prominence catalog provided by the Heliophysics Events Knowledgebase (HEK) system. One advantage of this work will be determining when cavities and prominences are associated as a function of solar cycle. We will categorize prominences associated with cavities and prominences not associated with cavities and then examine the length and the tilt of the prominences. Analyzing prominence data such as length and tilt will help determine when a prominence is likely to form a cavity. This study will help to determine the correlation between the cavity, prominence, and global magnetic field distribution, ultimately resulting in better predictions of upcoming solar cycles.

Appendix A: HMI central meridian Synoptic map

The method to construct HMI central meridian synoptic map used in Chapter 2 and Chapter 4 is explained below. First, the HMI images converted from helioprojective coordinates (HC) to Stonyhurst heliographic coordinates (SHC) system then to heliocentric earth equatorial coordinates (HEEQ), and finally to heliocentric cartesian coordinate (HCC) as seen from earth using the formulas in Thompson (2006). The detailed formulae used in the conversion from image coordinates to HCC are given below.

Helioprojective coordinates to Stonyhurst heliographic coordinates

The latitude Θ and longitude Φ are in degrees. Θ increases towards solar North, and Φ increases towards the solar West limb and r is equal to one solar radius.

Stonyhurst heliographic coordinates to heliocentric earth equatorial coordinates

$$X_{HEEQ} = r \cos\Theta \cos\Phi \tag{A.1}$$

$$Y_{HEEQ} = r \cos\Theta \sin\Phi \tag{A.2}$$

$$Z_{HEEQ} = r \sin\Theta \tag{A.3}$$

Heliocentric earth equatorial coordinates to heliocentric cartesian coordinates

$$x = Y_{HEEQ} \tag{A.4}$$

$$y = Z_{HEEQ} \cos B_0 - X_{HEEQ} \sin B_0 \tag{A.5}$$

$$z = Z_{HEEQ} \sin B_0 + X_{HEEQ} \cos B_0 \tag{A.6}$$

After the coordinate transformation, HMI synoptic maps are generated using longitudinal stripes of 13.6°, centered at the central meridian running from latitude -90° to 90°. Four images per day, corresponds to a six hour cadence. Each stripe is 3/4 overlapped over the other. The stripes were accumulated from right to left for 27.27 days. The total stripes are then divided by the number of overlapping pixels to get the average value at each pixel of the synoptic map. The constructed synoptic map has 1080 pixels in latitude and 3600 pixels in longitude (Figure A.1).

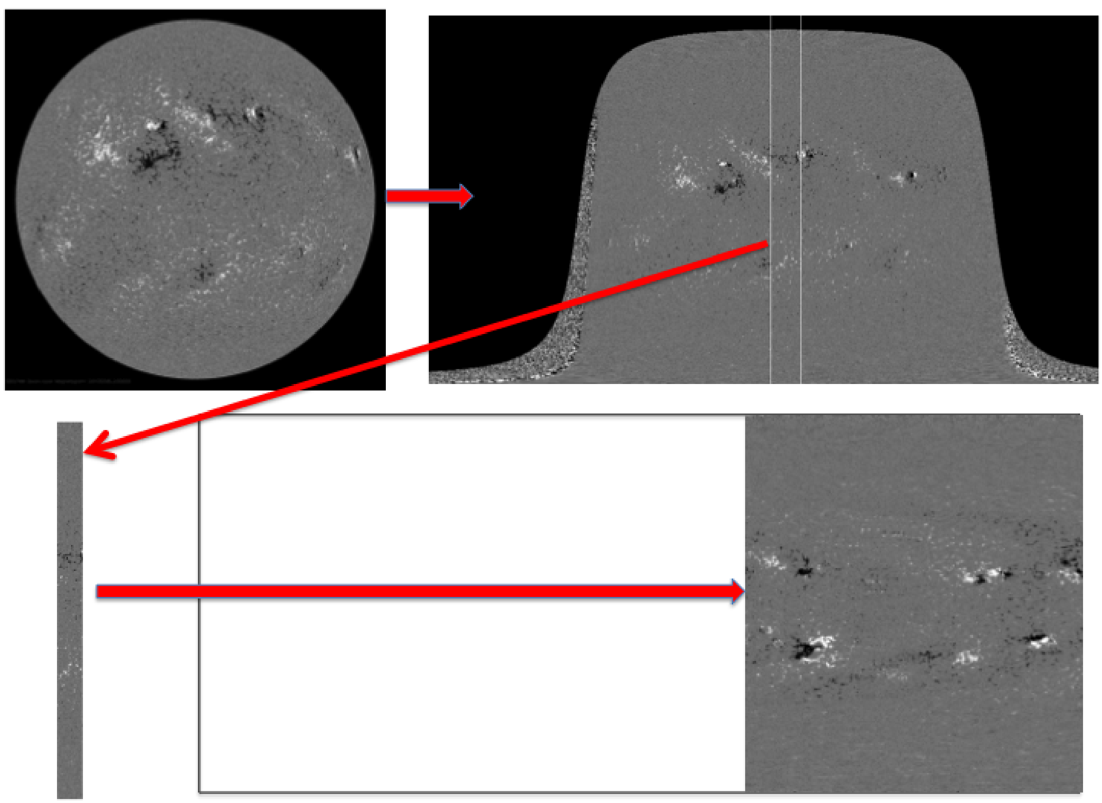

Figure A.1: HMI central meridian synoptic map constructed from 4 images per day for 27.27 days.

Appendix B: Measurements

B.1 Length Measurements using synoptic map

Positions along the path of the cavity are recorded as N latitudes (θ_i) and longitudes (ϕ_i) for $i = 1, \ldots, N$. The length (S) of the cavity is then a sum over the differential lengths along the path of the cavity:

$$S = R_\odot \sum_{i=1}^{N-1} \sqrt{(\theta_{i+1} - \theta_i)^2 + \cos^2 \bar{\theta}_i (\phi_{i+1} - \phi_i)^2}, \tag{B.1}$$

where $\bar{\theta}_i = (\theta_{i+1} + \theta_i)/2$ and $R_\odot = 6.95 \times 10^5$ km is the radius of the Sun.

B.2 Width Measurements using synoptic map

The width (ΔW) of the cavity is the distance between the bounding latitudes measured along a meridian ($\Delta\phi = 0$), or

$$\Delta W = R_\odot |\theta_+ - \theta_-|, \tag{B.2}$$

where θ_+ and θ_- are the measured poleward and equatorward heliographic latitudes of the respective edges.

B.3 Height and Width Measurements using snapshot image

In order to measure the height and width of the cavity, we fitted the ellipse based on cavity shape.

The height is the maximum radial distance of the fit.

$$h = R_2 - R_1, \tag{B.3}$$

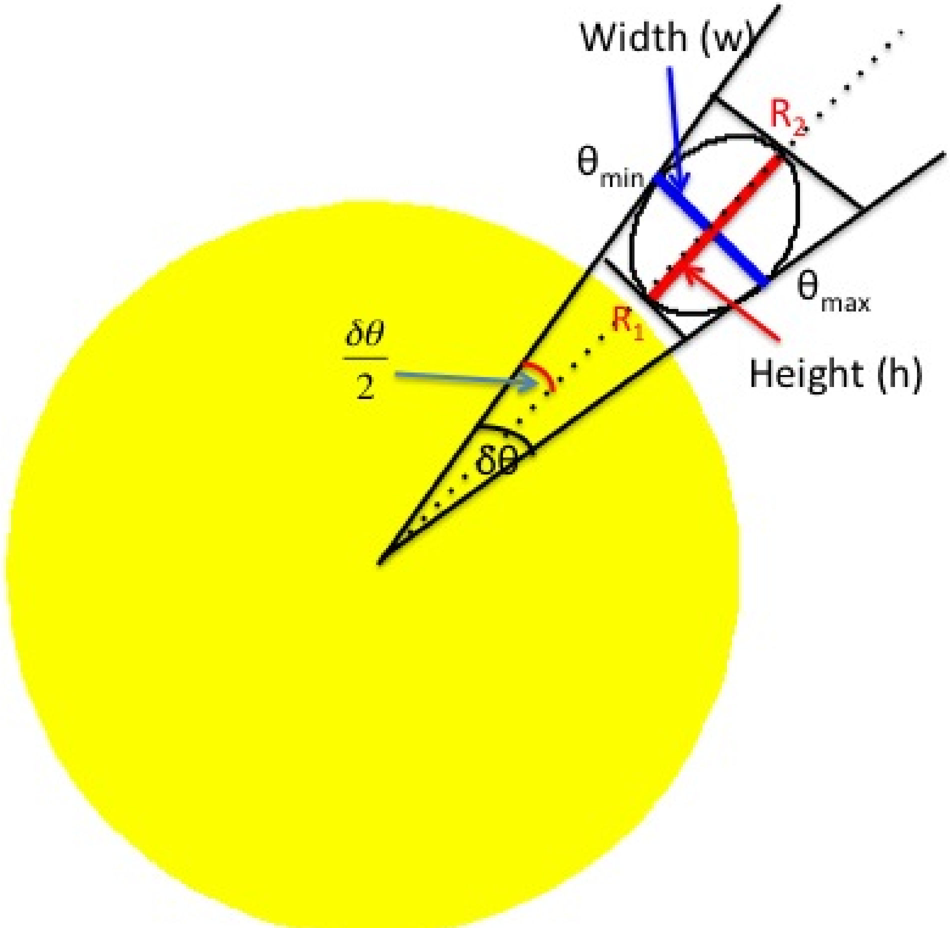

Figure B.1: Schematic illustrating the height and width measurements of a Cavity.

where, $R_1 \geq R_\odot$

The width (w) of the cavity is the maximum separation distance between the bounding latitudes ($\theta_{\max}, \theta_{\min}$).

$$w = 2R'_\odot \sin\left(\frac{\theta_{\max} - \theta_{\min}}{2}\right), \tag{B.4}$$

where $R'_\odot = \max[R_{\theta_{\max}}, R_{\theta_{\min}}]$, $R_{\theta_{\max}}$ and $R_{\theta_{\min}}$ are the distances from the center of the Sun to the maximum ($\theta_{\max}$) and minimum ($\theta_{\min}$) bounding colatitudes positions of the ellipse fit.

Appendix C: Cavity Catalog

The limb synoptic maps are available at George Mason University (GMU) Space Weather Lab. The online cavity catalog lists the number of cavities seen in each Carrington Rotation from CR 2097 to CR 2159 (May 20, 2010–February 1, 2015), along with the length, height, width, the heliographic longitudes, and latitudes of the appearance and disappearance of the cavity. Figure C.1 is a screenshot of the synoptic map catalog. Limb synoptic maps are available in seven passbands: 304 Å (He II), 171 Å (Fe IX), 193 Å (Fe XII, XXIV), 211 Å (Fe XIV), 335 Å (Fe XVI), 94 Å (Fe XVIII), and 131 Å (Fe VIII, XX, XXIII). All the measurements are done using AIA 193 Å synoptic maps and snapshot images.

We observed 429 cavities in four and half years of data. Table C.1 to Table C.6 lists the number of cavities appeared in the eastern limb and Table C.7 to Table C.11 lists the number of cavities appeared on the western limb. The column starts with the cavity Id, starting latitude, starting longitude, ending latitude, ending longitude, length, tilt angle, date (the particular date on which ellipse was fitted to measure the height and width of the cavities), height, and the last column is the width.

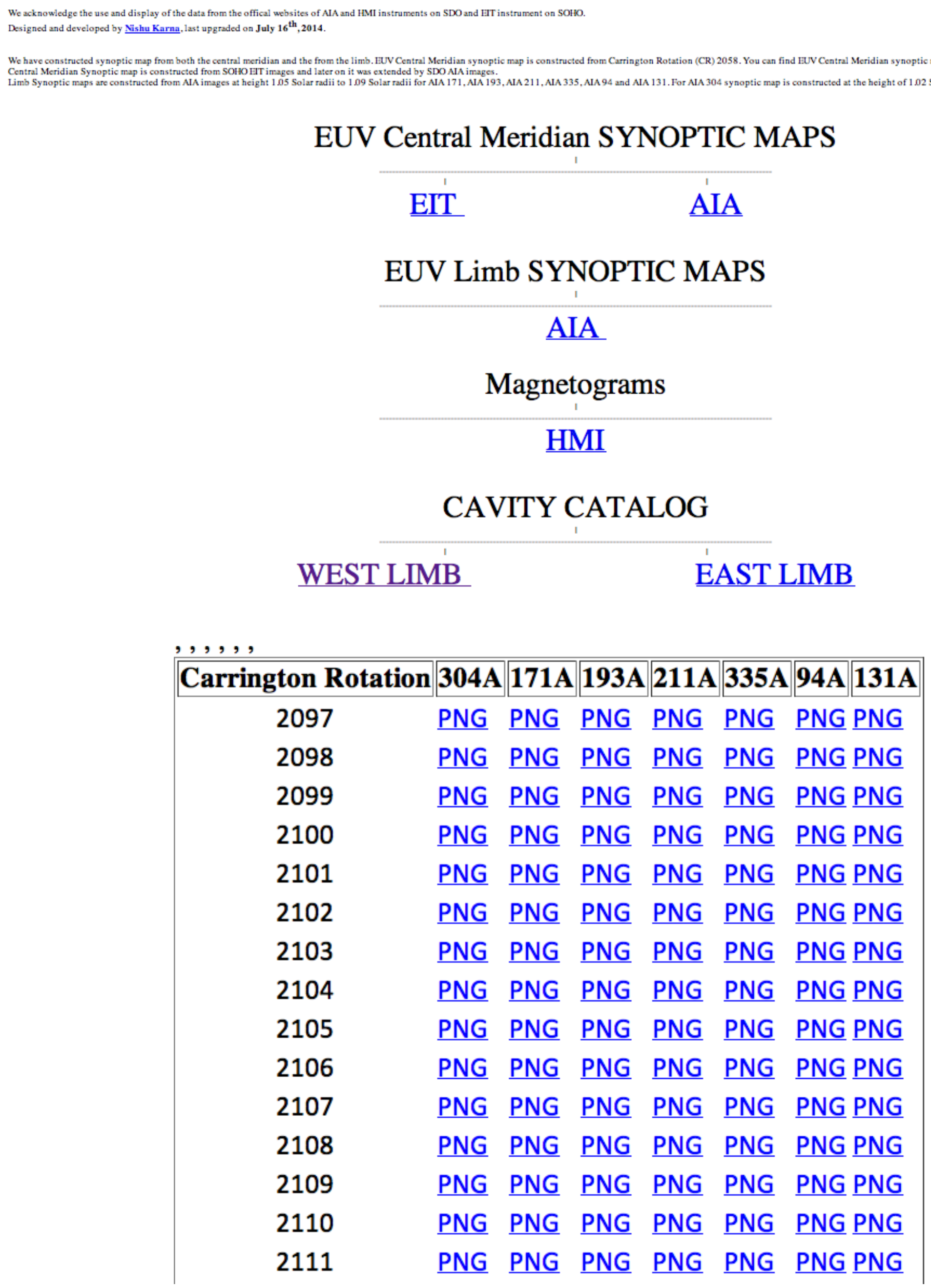

We acknowledge the use and display of the data from the offical websites of AIA and HMI instruments on SDO and EIT instrument on SOHO.
Designed and developed by Nishu Karna, last upgraded on **July 16th, 2014**.

We have constructed synoptic map from both the central meridian and the from the limb. EUV Central Meridian synoptic map is constructed from Carrington Rotation (CR) 2058. You can find EUV Central Meridian synoptic map from CR 1911 to CR 2055 from Stanford .
Central Meridian Synoptic map is constructed from SOHO EIT images and later on it was extended by SDO AIA images.
Limb Synoptic maps are constructed from AIA images at height 1.05 Solar radii to 1.09 Solar radii for AIA 171, AIA 193, AIA 211, AIA 335, AIA 94 and AIA 131. For AIA 304 synoptic map is constructed at the height of 1.02 Solar radii to 1.06 Solar radii.

EUV Central Meridian SYNOPTIC MAPS

EIT AIA

EUV Limb SYNOPTIC MAPS

AIA

Magnetograms

HMI

CAVITY CATALOG

WEST LIMB EAST LIMB

, , , , , ,

Carrington Rotation	304A	171A	193A	211A	335A	94A	131A
2097	PNG	PNG	PNG	PNG	PNG	PNG	PNG
2098	PNG	PNG	PNG	PNG	PNG	PNG	PNG
2099	PNG	PNG	PNG	PNG	PNG	PNG	PNG
2100	PNG	PNG	PNG	PNG	PNG	PNG	PNG
2101	PNG	PNG	PNG	PNG	PNG	PNG	PNG
2102	PNG	PNG	PNG	PNG	PNG	PNG	PNG
2103	PNG	PNG	PNG	PNG	PNG	PNG	PNG
2104	PNG	PNG	PNG	PNG	PNG	PNG	PNG
2105	PNG	PNG	PNG	PNG	PNG	PNG	PNG
2106	PNG	PNG	PNG	PNG	PNG	PNG	PNG
2107	PNG	PNG	PNG	PNG	PNG	PNG	PNG
2108	PNG	PNG	PNG	PNG	PNG	PNG	PNG
2109	PNG	PNG	PNG	PNG	PNG	PNG	PNG
2110	PNG	PNG	PNG	PNG	PNG	PNG	PNG
2111	PNG	PNG	PNG	PNG	PNG	PNG	PNG

Figure C.1: Screen shot of the synoptic map catalog

Table C.1: Eastern Limb Cavities (CR 2097- CR 2106)

ID	S. Lat	S.Lon	E. Lat	E. Lon	Len	Tilt	Date	Height	Width
C20972797N	27.5	120.6	30.75	78.525	447.9	4.4	20100608	0.22	0.086
C20975228S	51.75	47.475	53.75	15.3	237.6	3.6	20100613	0.148	0.123
C209737169N	36	185.85	38	157.5	275.9	4	20100603	0.401	0.227
C209748206N	43	245.7	52.75	172.125	610.6	7.5	20100531	0.245	0.245
C20975680N	57.25	163.575	50.5	0	1173.5	2.4	20100609	0.353	0.269
C209752300S	57.75	360	51	247.05	802.8	3.4	20100524	0.19	0.23
C20984916S	46	38.475	56.25	0	318.4	14.9	20100711	0.204	0.26
C20984067S	36.5	92.025	42.5	50.625	394.6	8.2	20100708	0.196	0.16
C20985790N	57.5	173.025	63.5	0	1036.8	2	20100709	0.217	0.217
C209865317N	66	360	63	272.25	460	2	20100620	0.228	0.231
C209852314S	49.75	360	54.75	255.375	779.9	2.7	20100618	0.151	0.213
C20994321S	41.5	45.9	52.25	0	402.6	13.2	20100807	0.18	0.139
C20995752N	60.25	104.85	63.5	0	601.3	1.8	20100805	0.324	0.295
C209948143N	46.75	202.95	48.75	90.45	918.5	1	20100728	0.188	0.133
C20994191S	38.25	123.075	43.5	67.05	518.2	5.4	20100802	0.137	0.187
C209953300S	56	360	59.5	229.95	843.5	1.5	20100715	0.275	0.266
C210060327N	66	360	56.25	288	438.3	7.7	20100812	0.199	0.209
C210051333S	52.25	360	60.75	307.575	366.1	9.2	20100811	0.205	0.16
C210048166N	50.75	205.875	45.75	125.55	652.1	3.6	20100824	0.402	0.237
C21005280N	55.25	109.8	52.25	51.075	423.1	2.9	20100829	0.211	0.194
C21004021S	34.5	47.025	40.5	0	458.7	7.3	20100903	0.142	0.152
C210162310N	60.25	360	57.25	233.325	798.5	1.4	20100910	0.271	0.303
C21015730N	67.5	69.525	55	0	433.4	10.2	20101001	0.222	0.224
C210156210S	51.75	247.95	63.5	182.25	450.2	10.1	20100915	0.385	0.313
C21024885S	45.5	105.525	48	69.75	299.1	4	20101023	0.202	0.149
C21025614S	53	32.175	62.25	0	237.4	16	20101029	0.13	0.161
C210341196N	42.25	222.975	41.25	170.55	474.9	1.1	20101112	0.136	0.181
C210357299N	51.25	360	58	228.825	925.5	2.9	20101103	0.179	0.245
C210350101N	53.25	144.9	51	63.45	607.6	1.6	20101118	0.227	0.239
C21043170N	29	96.525	33.5	47.025	516.6	5.2	20101218	0.157	0.125
C21044817S	46.5	40.05	52.25	0	324.1	8.2	20101222	0.136	0.133
C210453335S	56	360	56	309.825	340.6	0	20101128	0.146	0.152
C210440241S	37.75	272.25	38	220.725	493.7	0.3	20101205	0.394	0.287
C210452133S	46	196.2	60.75	76.05	888.3	7	20101213	0.248	0.244
C210458266N	54.5	360	60.5	147.825	1385.8	1.6	20101204	0.219	0.22
C210449136N	46.75	171.9	50.75	114.3	463.6	4	20101212	0.164	0.15
C210559258N	58.5	292.05	59.75	228.15	398.3	1.1	20110101	0.247	0.276
C210558133N	57.25	215.1	62	34.425	1110.5	1.5	20110110	0.154	0.164
C21055491S	55	118.35	51.5	70.425	350.7	4.2	20110113	0.145	0.135
C21065640S	61.25	80.325	49.25	0	574.5	8.5	20110213	0.203	0.149
C21065970N	61	136.8	58.75	0	833.9	0.9	20110211	0.23	0.287
C210659216N	55.5	249.75	64.5	184.05	413.5	7.8	20110131	0.322	0.342

Table C.2: Eastern Limb Cavities (CR 2107- CR 2117)

ID	S. Lat	S.Lon	E. Lat	E. Lon	Len	Tilt	Date	Height	Width
C21076019N	59.75	44.55	65.75	0	258.1	7.7	20110314	0.223	0.201
C210743114S	51.25	165.15	40	67.725	838.3	6.6	20110306	0.422	0.242
C210754343S	51	360	55.5	322.2	279.9	6.8	20110217	0.192	0.159
C210864321N	59	360	67.5	272.925	486.8	5.6	20110318	0.307	0.306
C210861109N	58.5	156.375	63.75	59.85	569.4	3.1	20110404	0.201	0.232
C210826327N	21.75	360	25	290.925	770.7	2.7	20110317	0.112	0.109
C21083965S	41	105.3	33.25	32.625	709.6	6.1	20110406	0.25	0.245
C21096436N	63.75	81	70.75	0	389.6	4.9	20110506	0.154	0.152
C210944183S	45.25	223.2	45.25	150.75	619.1	0	20110424	0.153	0.179
C210964302N	63.75	325.8	64.75	274.5	270.8	1.1	20110416	0.099	0.153
C210947262N	42.25	292.5	49.75	235.35	490.4	7.5	20110420	0.19	0.144
C211061288N	62.25	360	62.75	222.075	773.1	0.2	20110515	0.307	0.261
C21105386N	52.75	126	54.5	54.45	515.5	1.4	20110528	0.413	0.254
C21104325S	42.25	58.05	39.75	0	532.7	2.5	20110603	0.186	0.149
C211049176S	49	208.8	51	148.725	469.4	1.9	20110523	0.162	0.246
C211164296N	59.75	360	65.25	243.9	654.2	2.7	20110610	0.237	0.198
C211159171N	61.75	206.325	57.75	144.225	382.8	3.7	20110620	0.309	0.228
C211257343N	51.75	360	56	321.975	277	6.4	20110704	0.161	0.151
C211243164S	39.5	201.375	42	133.2	627.7	2.1	20110717	0.185	0.178
C211244260N	42.25	280.125	44.25	245.025	311.3	3.3	20110710	0.147	0.16
C211263230N	64.75	304.2	68.5	148.725	750.2	1.4	20110713	0.112	0.145
C21134518N	45.75	40.5	50	0	333.8	6	20110824	0.328	0.271
C211363147N	62.25	198.45	64.25	108.45	492.3	1.3	20110814	0.253	0.172
C211351189S	44.5	230.4	50.75	146.7	689	4.3	20110811	0.227	0.239
C211460143N	60	196.425	59.5	101.7	579.3	0.3	20110912	0.458	0.265
C211457144S	52.5	193.5	59.25	103.725	616.8	4.3	20110911	0.211	0.175
C21141517S	9	40.95	21.75	0	503.7	17.3	20110920	0.194	0.205
C211452288N	56.25	322.425	53.25	259.2	444.4	2.7	20110831	0.268	0.191
C211548316N	50	348.525	48.75	276.75	567.5	1	20110926	0.255	0.273
C211560110N	63.25	142.65	58.25	86.175	340.4	5.1	20111010	0.168	0.165
C211555128S	49.5	176.4	58	91.35	619.1	5.7	20111009	0.156	0.207
C21153732S	32.25	52.65	40.75	15.3	378.8	12.8	20111016	0.164	0.143
C21166251N	63.75	102.6	69	0	503.2	2.9	20111112	0.335	0.233
C21164830N	44.25	56.925	49.5	12.6	373.3	6.8	20111113	0.371	0.401
C211650305N	56.25	346.95	47.75	264.825	622.4	5.9	20111024	0.212	0.212
C21165499S	48.75	168.075	58.25	31.5	992.8	4	20111108	0.154	0.215
C21175843S	57.75	81.45	62.75	0	494.4	3.5	20111211	0.211	0.223
C211750126S	51	153.675	51	103.275	385	0	20111203	0.348	0.301
C21176072N	56	121.5	68	27.45	555.4	7.3	20111208	0.367	0.243
C211760295N	57.25	360	59	224.55	868.5	0.7	20111119	0.223	0.273

Table C.3: Eastern Limb Cavities (CR 2118- CR 2125)

ID	S. Lat	S.Lon	E. Lat	E. Lon	Len	Tilt	Date	Height	Width
C21185434N	51.5	78.525	61	0	542	6.9	20120107	0.101	0.161
C211866306N	61	360	69.25	241.875	611.4	4	20111217	0.175	0.162
C211846320S	54.5	360	47	277.875	637.3	5.2	20111216	0.193	0.198
C21185439S	52.75	78.075	49.5	0	596.1	2.4	20120106	0.201	0.255
C211935344S	38.75	360	34.5	320.4	389.2	6.1	20120109	0.109	0.184
C211967209N	65.75	265.275	68.5	163.125	483.2	1.5	20120120	0.211	0.307
C21195675N	51	101.7	60.5	54.225	344.2	11.3	20120129	0.172	0.263
C21195715S	57.5	30.6	60.5	0	194.7	5.6	20120204	0.15	0.215
C211957324S	66.25	360	61	286.425	401.8	4.1	20120110	0.145	0.185
C212064209N	56.75	333.225	69.25	93.6	1329.2	3	20120217	0.141	0.226
C212058303S	61.75	360	60	241.875	698.2	0.8	20120209	0.134	0.133
C21202674S	25.5	97.875	27.25	56.25	453.2	2.4	20120227	0.332	0.161
C21205309S	54.25	23.4	57.5	0	164.2	7.9	20120302	0.208	0.183
C212162227N	59	306.675	67.25	150.75	861.4	3	20120313	0.199	0.167
C21216580N	63	133.425	71	35.775	473.2	4.7	20120325	0.156	0.206
C212155298S	47.25	360	54.75	236.025	951.4	3.5	20120309	0.348	0.249
C212144112N	39.5	140.625	47.25	87.75	475.9	8.3	20120322	0.199	0.241
C212139110S	39	142.425	42.5	89.325	490.1	3.8	20120323	0.144	0.154
C21226357N	61.75	112.5	70.5	0	562.8	4.4	20120426	0.355	0.228
C21224850S	50	84.15	47	21.6	504.4	2.7	20120422	0.339	0.305
C212263203N	61.5	248.4	64.75	152.325	528.7	1.9	20120412	0.273	0.283
C212246231N	44.75	247.95	48.25	219.825	238.8	7.1	20120410	0.145	0.097
C212253289S	47.25	360	54.25	212.625	1135.1	2.7	20120406	0.217	0.158
C21236423N	65.25	53.325	60.5	0	300.7	5.1	20120523	0.269	0.17
C212366335N	61.5	360	65.5	302.4	315.7	4	20120430	0.188	0.186
C212366114N	68.25	146.025	66.75	87.075	274.4	1.5	20120514	0.346	0.251
C212352277N	51	306.45	53.5	255.375	380.8	2.8	20120502	0.157	0.177
C212355224S	55	325.575	56.25	96.975	1566.8	0.3	20120510	0.164	0.162
C21235026S	47.75	58.5	56.75	0	448.3	8.7	20120523	0.204	0.253
C212468334N	71.25	360	69	302.4	239.3	2.2	20120526	0.258	0.262
C21246725N	70.5	58.275	70.75	0	234.7	0.2	20120619	0.27	0.29
C212457203S	51.5	282.15	56	135.9	1051.2	1.8	20120606	0.174	0.203
C212564303N	62	360	65.25	256.5	559.5	1.8	20120625	0.238	0.212
C212554216S	42.5	319.725	62.5	113.175	1545.5	5.5	20120630	0.231	0.251
C212566144N	67.75	177.075	69.5	114.75	276.6	1.6	20120705	0.348	0.255

Table C.4: Eastern Limb Cavities (CR 2126- CR 2134)

ID	S. Lat	S.Lon	E. Lat	E. Lon	Len	Tilt	Date	Height	Width
C212668319N	66.25	360	67.5	275.4	403.6	0.8	20120721	0.21	0.243
C212665124N	68	161.1	64.75	95.175	323.1	2.8	20120804	0.227	0.212
C21266085S	51.25	150.75	60.75	25.65	857	4.3	20120807	0.199	0.238
C212655277S	50.5	360	59	192.6	1177.3	2.9	20120727	0.216	0.245
C212767125N	76.25	250.875	64.75	0	1026.1	2.6	20120904	0.244	0.295
C212756247S	50.75	281.25	59.25	218.7	447.6	7.7	20120823	0.154	0.257
C21274423S	41.5	47.925	51.5	0	418.4	11.8	20120909	0.169	0.2
C21276050S	57.25	112.725	65	0	667.4	3.9	20120907	0.187	0.208
C21283838S	28.5	82.125	39.25	0	837.9	7.5	20121005	0.34	0.22
C21285964S	47.5	126.45	72.5	0	825.3	11.2	20121004	0.188	0.233
C212851314S	43.75	349.875	59.25	281.475	550	12.8	20120914	0.338	0.176
C212871150N	73.5	190.575	69.75	119.475	275.9	3	20120927	0.14	0.174
C212963167N	68.25	222.525	62.25	113.175	560.5	3.1	20121023	0.158	0.21
C21295746S	49.25	97.875	57.5	0	715.8	4.8	20121101	0.314	0.203
C213044251N	47.25	284.625	45	219.6	547.8	2	20121112	0.138	0.135
C21307429N	75	63.675	72.5	0	218.4	2.2	20121130	0.143	0.157
C213071295N	73	325.35	70.5	269.1	216	2.5	20121111	0.109	0.162
C213063213S	60.25	288.675	63	152.1	788.6	1.2	20121115	0.112	0.194
C213165149S	60	253.125	64.75	70.2	1031.2	1.5	20121215	0.189	0.205
C213168160N	69.25	232.875	64.25	101.925	630.4	2.2	20121216	0.231	0.186
C213177314N	82	360	77	262.35	224.4	2.9	20121205	0.195	0.194
C213146342N	50.25	360	40.5	322.875	338	14.7	20121203	0.175	0.164
C213276167N	78.25	198	77.75	143.775	137	0.5	20130113	0.148	0.222
C21327234N	72.5	70.425	70.75	0	270.3	1.4	20130121	0.324	0.315
C213263181N	59	256.275	72.5	125.325	673.1	5.9	20130111	0.113	0.101
C213266112S	64	217.35	66.25	28.8	963.1	0.7	20130116	0.259	0.245
C213255331S	53.25	360	59.5	294.075	449.6	5.4	20121231	0.197	0.166
C213241180N	41.5	210.375	41.75	153.9	512.5	0.3	20130110	0.131	0.211
C21337416N	71.5	40.5	82.25	0	171.7	14.9	20130221	0.295	0.16
C213365115N	64.25	162.675	72.25	75.375	404.5	5.2	20130213	0.127	0.219
C213380142N	79	204.525	84.25	85.5	219.9	2.5	20130212	0.247	0.176
C213336334S	35.25	360	36.5	303.3	557.9	1.3	20130128	0.35	0.213
C213345321S	46.75	348.525	43.75	298.575	428.4	3.4	20130127	0.195	0.184
C213366106S	60.5	237.375	72.5	0.225	1157.1	2.9	20130214	0.116	0.133
C213444213N	41	238.05	48	192.825	400.7	8.8	20130305	0.179	0.251
C213454214N	54	232.65	58	198.9	234.2	6.8	20130304	0.296	0.161
C213465346S	69.25	360	67.25	326.7	151.7	3.4	20130224	0.084	0.137
C21344430N	42.5	65.025	50.75	0	551.3	7.2	20130318	0.195	0.116
C21346383S	62.5	168.075	66.5	23.85	755.3	1.6	20130314	0.262	0.254

Table C.5: Eastern Limb Cavities (CR 2135- CR 2146)

ID	S. Lat	S.Lon	E. Lat	E. Lon	Len	Tilt	Date	Height	Width
C213571318S	78.75	360	69	263.7	345.6	5.8	20130325	0.103	0.19
C213548325S	51.25	360	46.5	281.475	629.6	3.5	20130322	0.167	0.166
C213560240N	52	279	67.5	189.675	577.7	9.8	20130330	0.206	0.203
C21355223N	51.25	55.35	57.5	0	398.6	6.4	20130415	0.218	0.149
C21356451S	66.75	117.9	70.75	0	521	1.9	20130413	0.235	0.136
C213647249N	36.25	308.925	53.25	195.75	997.2	8.5	20130425	0.134	0.142
C21366139S	57.75	82.35	59.5	0	520.9	1.2	20130512	0.236	0.243
C213669284S	73.5	360	69.75	199.575	615.6	1.3	20130423	0.36	0.249
C213650241S	50.25	294.3	48	198	765.5	1.3	20130424	0.176	0.18
C213768244S	72.75	360	69	132.3	906.7	0.9	20130524	0.277	0.22
C213749218S	44.5	306	58.5	125.1	1377.5	4.4	20130526	0.143	0.167
C21376358S	57.5	110.925	65.5	0	649.8	4.1	20130606	0.133	0.143
C213752208N	54	237.825	52.25	189.225	354.6	2.1	20130526	0.328	0.238
C213868177S	68.25	360	66.25	0	1690.1	0.3	20130624	0.126	0.197
C213866323N	61.75	360	67.75	288.9	375.3	4.8	20130612	0.258	0.236
C213968168S	60.75	360	67.25	0	1917.3	1	20130723	0.19	0.205
C213947194S	45.25	244.575	51.75	149.4	769.6	3.9	20130720	0.136	0.211
C213954337N	54.25	360	57	303.525	388.5	2.8	20130710	0.149	0.158
C214069166S	63.5	360	65	0	1898.6	0.2	20130819	0.202	0.272
C214036315S	29.75	360	46.75	254.925	1022.7	9.2	20130808	0.144	0.21
C214066301N	73	360	60.25	231.3	638.9	5.7	20130811	0.272	0.16
C214168229S	66	320.4	69	168.975	704.4	1.1	20130908	0.293	0.211
C214138236S	38	267.075	43.5	205.65	568.8	5.1	20130909	0.13	0.228
C21415262S	45	100.35	62.25	29.925	548.5	13.8	20130922	0.156	0.162
C214156264N	50.5	319.725	64.75	218.025	683.3	8	20130905	0.311	0.31
C214269167S	56.25	360	67.25	0	2072.7	1.8	20131012	0.236	0.262
C214256243N	58.5	302.85	52.5	194.85	746.1	3.2	20131006	0.254	0.239
C214259182N	61.5	212.625	59.25	153.675	354.8	2.2	20131011	0.192	0.227
C214233344N	36.25	360	31.75	323.55	370.9	7	20130930	0.208	0.201
C214215243N	15.75	266.175	12.25	225	486.8	4.9	20131007	0.309	0.153
C214368130S	60.25	282.375	66.5	0	1538	1.3	20131110	0.19	0.192
C214362165N	71	276.75	58.5	61.2	1126.4	3.3	20131112	0.208	0.226
C214471314S	67	360	74.75	258.975	412.6	4.4	20131125	0.258	0.219
C21446766S	65.75	137.7	65.25	0.45	690.9	0.2	20131213	0.111	0.182
C214454323S	49.5	360	56	287.1	541.4	5.1	20131124	0.152	0.176
C214571327S	64.25	360	73.25	280.8	365.2	6.5	20131221	0.282	0.253
C214549312S	50.25	360	50	265.95	731.9	0.2	20131222	0.168	0.229
C214575148S	76.5	231.525	69.75	66.6	586.9	2.3	20140104	0.315	0.297
C21455343N	46.25	86.175	57.75	12.825	565.7	8.9	20140111	0.29	0.155
C214676152S	70.75	360	67	0	1575.6	0.6	20140202	0.26	0.322
C214652284S	46.5	329.625	54.75	250.425	618.1	5.9	20140121	0.135	0.117
C21464646N	35.75	100.8	49.25	0	916.9	7.6	20140206	0.345	0.281
C214634243N	30	286.65	40.75	211.275	757.4	8.1	20140123	0.245	0.193

Table C.6: Eastern Limb Cavities (CR 2147- CR 2159)

ID	S. Lat	S.Lon	E. Lat	E. Lon	Len	Tilt	Date	Height	Width
C214776107S	76.5	213.75	77.5	32.4	495.3	0.3	20140301	0.27	0.194
C214770309S	78.75	360	70.5	260.325	336.1	4.7	20140214	0.287	0.232
C214751292S	52.25	327.825	50	261	509.8	1.9	20140216	0.201	0.194
C21473399N	25	137.475	35.75	71.775	700.3	9.3	20140302	0.184	0.194
C214754345N	49.25	360	56	324.45	274.5	10.8	20140211	0.258	0.193
C21485213S	55.25	27.675	45	0	248.7	20.3	20140406	0.149	0.182
C214876244S	84.25	336.6	75.25	159.3	398.2	2.9	20140320	0.289	0.19
C214853283N	50.5	299.7	57.75	271.35	220	14.3	20140316	0.288	0.226
C214947126N	46.25	137.475	51.75	116.325	181.2	14.6	20140424	0.264	0.209
C214976286S	80.75	360	80.5	207.9	300.8	0.1	20140413	0.21	0.176
C214948344S	53.5	360	47.75	320.4	312.8	8.3	20140408	0.384	0.295
C215072290S	75.25	360	77.25	220.05	404.5	0.8	20140510	0.379	0.354
C215176171S	72.5	241.2	78	111.825	405.4	2.4	20140615	0.244	0.168
C215280316S	79.75	360	79.25	270.9	197.2	0.3	20140701	0.146	0.167
C215380313S	75.25	360	78	277.65	233.6	1.9	20140728	0.281	0.222
C215477141S	74.5	222.75	78.5	75.6	419.8	1.6	20140907	0.106	0.172
C215579258S	79	288.9	80.75	235.75	115.4	1.9	20140924	0.173	0.23
C21554224S	38.5	50.4	43.5	0	465.7	5.7	20141012	0.302	0.264
C21561523N	16.25	55.35	12.25	0	653	4.1	20141109	0.285	0.263
C21568631S	84.25	63.9	84.25	0	77.7	0	20141107	0.139	0.138
C215783178S	82	216.225	83.5	143.1	113.5	1.2	20141124	0.178	0.136
C215736196N	35	212.175	36.75	184.275	275.2	3.6	20141123	0.14	0.176
C215728290N	23.25	313.875	33.25	263.925	547.7	11.3	20141116	0.184	0.191
C215829285N	27.25	297.45	32.75	269.325	303.1	11.1	20141214	0.184	0.177
C215937194S	30.5	222.75	44.5	167.4	559.5	14.2	20150117	0.3	0.236

Table C.7: Western Limb Cavities (CR 2097- CR 2110)

ID	S. Lat	S.Lon	E. Lat	E. Lon	Len	Tilt	Date	Height	Width
C209755304N	52.25	360	59.5	229.5	893	3.2	20100523	0.236	0.222
C209744339S	47.5	360	45.75	312.975	392.6	2.1	20100520	0.174	0.174
C20984425N	40	53.775	50.5	0	476.9	11	20100711	0.13	0.135
C20985399S	55.75	127.125	54.5	68.175	409.4	1.2	20100706	0.146	0.169
C209858246N	59	327.825	62.75	157.275	1008.7	1.3	20100625	0.102	0.16
C209843334S	40.5	360	46.5	311.4	434.1	7	20100618	0.229	0.237
C209957215N	55.75	291.825	58.75	126	1089.5	1	20100727	0.193	0.197
C210048329N	42.75	360	53.5	292.725	560.5	9.1	20100812	0.187	0.225
C210057193N	48.75	257.4	61.5	136.125	855.9	6	20100822	0.169	0.257
C210150307N	40.5	357.975	52	265.5	788.7	7.1	20100909	0.263	0.223
C210154223N	57.5	234.675	57.5	212.175	146.7	0	20100915	0.233	0.302
C210256144N	51.25	212.85	61.75	50.175	1097.3	3.7	20101021	0.36	0.201
C21023296N	31	115.65	37.5	75.15	414	9.1	20101023	0.197	0.202
C210348294N	46	331.65	47	253.575	652.5	0.7	20101105	0.182	0.19
C210355179N	54.25	210.825	56.75	142.2	472.8	2.1	20101113	0.251	0.231
C21035853N	57.25	108.675	61.5	0	674	2.2	20101122	0.14	0.157
C21033477N	34.25	90.225	35.75	59.4	307	2.8	20101120	0.213	0.216
C210351344S	49.75	360	52.5	320.625	301.8	4	20101031	0.148	0.215
C210345244S	43.5	265.275	45	223.2	366.3	2	20101108	0.208	0.181
C210461297N	62.5	322.425	60.75	267.3	318.7	1.8	20101201	0.182	0.202
C21045779N	57.75	140.175	57.75	10.8	838	0	20101218	0.269	0.233
C210452327S	47.75	360.45	55.25	285.075	576.8	5.7	20101228	0.11	0.175
C210558281N	63.5	353.7	59.25	195.75	920	1.5	20110101	0.273	0.228
C21056144N	65.25	88.875	61.25	0	488	2.6	20110116	0.231	0.213
C210555259S	54	290.475	57.5	228.825	423.3	3.2	20111230	0.249	0.297
C210662244N	64	306.9	57.75	188.1	706	3	20110129	0.159	0.146
C21066224N	61.75	51.075	57	0	321.1	5.3	20110214	0.291	0.228
C210640284S	40	303.975	43	271.35	298.8	5.3	20110125	0.153	0.113
C210658200S	56.25	228.825	60.5	176.85	334.8	4.7	20110201	0.083	0.125
C210760331N	64.5	360	60	303.3	325.1	4.5	20110217	0.083	0.125
C210759202N	58.5	246.825	58	153	599.3	0.3	20110302	0.209	0.262
C21074220S	38	40.725	52.5	0	390	19.6	20110315	0.196	0.171
C210863318N	67.25	360	61.75	272.25	463.4	3.6	20110319	0.174	0.169
C210861151N	60	193.275	62	99.225	554	1.2	20110401	0.15	0.186
C210840268S	35	285.75	44	255.15	306.7	16.4	20110321	0.243	0.234
C210964179N	67.5	295.425	63.75	36.675	1297.1	0.8	20110427	0.233	0.219
C210940221S	37	294.75	44.5	128.25	1533.8	2.6	20110424	0.202	0.19
C211062125N	62.5	253.575	62.5	0	1421.3	0	20110527	0.239	0.217
C21107122N	70	48.825	77.5	0	189.2	8.7	20110603	0.166	0.136
C211048192N	50.75	213.75	48	173.025	323.6	3.9	20110521	0.225	0.183
C211044132S	42	161.325	48.75	99.675	532	6.2	20110526	0.204	0.214
C21104251S	42.5	85.05	40	20.7	588.1	2.2	20110602	0.28	0.242

Table C.8: Western Limb Cavities (CR 2111- CR 2121)

ID	S. Lat	S.Lon	E. Lat	E. Lon	Len	Tilt	Date	Height	Width
C211159151N	49.75	285.975	74.75	0	1644.6	5	20110622	0.197	0.26
C211145159S	46.5	180.675	44.25	126	467	2.4	20110621	0.17	0.17
C21114848S	49.75	70.425	51.75	30.825	305.1	2.9	20110627	0.193	0.206
C211254187N	50.5	232.2	59	140.85	648.2	5.3	20110714	0.307	0.198
C21126038N	57	86.4	60	0	549.2	2	20110727	0.145	0.153
C21124260N	38.75	90.675	45.75	31.95	534.5	6.8	20110725	0.114	0.149
C211239213S	42	227.925	37.75	200.475	260.9	8.8	20110713	0.228	0.151
C21125032S	52.75	77.85	45.25	0	626.6	5.5	20110727	0.206	0.225
C211347177N	35	271.125	56.5	108	1406.2	7.5	20110812	0.265	0.271
C21135412S	52.75	18	56	0	133.2	10.2	20110825	0.225	0.206
C211344340S	41	360	44.75	320.625	353.2	5.4	20110731	0.206	0.218
C211366331N	67.5	360	70	293.175	295.6	2.1	20110801	0.214	0.28
C211463281N	59.5	348.3	65.5	217.8	735.1	2.6	20110901	0.155	0.132
C211447261N	43.25	285.75	54	230.85	459.4	11.1	20110903	0.27	0.147
C211442190N	32	269.1	52.75	98.55	1550	6.9	20110910	0.162	0.187
C211452336S	59.5	360	49.75	309.6	373.4	10.9	20110827	0.295	0.252
C211548232N	46.75	275.85	55	197.1	611.5	6	20111002	0.164	0.181
C211562231N	63	257.625	64.5	203.625	290.5	1.6	20111001	0.247	0.205
C211549103N	47.5	146.025	51.25	73.575	574.4	3	20111011	0.384	0.243
C211556329S	53.5	360	53.5	291.825	492.3	0	20110925	0.252	0.251
C21155211S	52	25.425	48.25	0	203	8.4	20111018	0.351	0.203
C211662218N	58.75	293.625	66.25	122.85	961.5	2.5	20111101	0.239	0.161
C211647214N	40.75	251.325	49.5	178.2	635.2	6.8	20111031	0.192	0.201
C211651313S	47.25	360	52.75	262.8	761.4	3.2	20111023	0.238	0.22
C21160891S	6.25	121.275	9.5	65.925	666.7	3.4	20111109	0.223	0.222
C211761296N	65	330.75	63	252.9	415	1.5	20111121	0.241	0.235
C211765165N	66.75	214.2	65.75	124.2	440.2	0.6	20111130	0.332	0.203
C211751280S	40.5	360	55.75	186.3	1419.6	5	20111123	0.216	0.198
C21174315S	43.25	41.85	47	0	361.3	5.1	20111211	0.194	0.153
C211863192N	63.25	214.2	64	175.5	208.9	1.1	20111225	0.239	0.189
C21186584N	66	130.5	68.75	29.025	475	1.6	20120103	0.286	0.253
C211857203S	55.5	260.1	60.5	156.15	671.4	2.8	20111224	0.116	0.147
C21196367N	60.75	137.025	68	0	724.7	3	20120128	0.165	0.253
C211957179S	54	217.575	58.5	143.1	505.2	3.5	20120123	0.134	0.229
C212071340N	75.75	360	72.25	315.675	154.3	4.5	20120207	0.203	0.175
C212047183N	46.75	202.275	45.5	159.075	363.8	1.7	20120219	0.187	0.181
C21206075N	63.5	157.05	66.5	0	806.5	1.1	20120228	0.176	0.191
C212050287S	47.5	326.025	53.5	255.15	552.1	4.8	20120211	0.174	0.236
C212057114S	50.25	205.875	62.5	28.575	1201	4	20120224	0.242	0.162
C21216037N	62.75	85.05	66	0	448.2	2.2	20120329	0.203	0.18
C212145269S	30.75	307.125	55.5	216.225	859.6	15.2	20120311	0.232	0.217
C212152134S	40	207.45	57.5	64.125	1166.6	7	20120321	0.201	0.184

Table C.9: Western Limb Cavities (CR 2122- CR 2130)

ID	S. Lat	S.Lon	E. Lat	E. Lon	Len	Tilt	Date	Height	Width
C212263316N	69.25	360	55.25	263.25	572.6	8.2	20120402	0.303	0.216
C212259345N	58.25	360	60.25	327.375	203.9	3.5	20120403	0.169	0.207
C212264247N	66	271.8	61	219.6	289.2	5.5	20120409	0.245	0.251
C212270213N	73.75	247.05	71.5	186.3	221.9	2.1	20120412	0.136	0.179
C21226924N	68.25	55.125	69.25	0	242.8	1	20120426	0.415	0.278
C212248247S	42	286.65	54.75	201.6	703	8.5	20120408	0.258	0.264
C21225474S	54	148.275	58.5	0	1001.4	1.7	20120422	0.328	0.275
C212567222N	65.25	277.425	68.5	155.925	580.6	1.5	20120629	0.26	0.26
C212540280N	40.25	301.5	45.5	255.825	411.3	6.6	20120626	0.332	0.248
C212528265N	26.5	282.15	31	252.225	323.1	8.6	20120628	0.291	0.111
C212522239N	19.5	266.625	28.75	208.35	655.3	9	20120630	0.194	0.107
C21254890N	42	142.875	56.75	39.825	833.9	8.1	20120712	0.365	0.327
C212556313S	66.25	360	52	267.525	601.5	8.8	20120624	0.178	0.192
C212553149S	49.5	187.2	53.75	118.125	523.1	3.5	20120707	0.218	0.197
C21255544S	56.5	98.1	54.5	0	674.9	1.2	20120714	0.242	0.291
C21254117S	42	31.725	41.75	6.975	223.7	0.6	20120716	0.139	0.201
C212666286N	71.25	360	73.75	196.875	596.2	0.9	20120722	0.281	0.183
C21267176N	74.25	137.475	74	23.625	378	0.1	20120808	0.155	0.125
C212641257N	43	275.4	43	245.25	267.7	0	20120726	0.125	0.15
C212658297S	55.25	360	55.5	230.175	895.4	0.1	20120723	0.114	0.189
C21265662S	59.5	115.875	56.75	25.425	580.8	1.7	20120810	0.116	0.182
C21276969N	65.75	161.775	67	0	787.1	0.4	20120905	0.366	0.28
C21274664N	44.25	128.7	46.75	23.85	892.6	1.4	20120903	0.25	0.226
C21275482S	53.25	130.725	56.75	46.125	590.6	2.4	20120904	0.123	0.212
C212759236S	57.5	310.05	62	179.325	801.3	2	20120824	0.228	0.213
C212717329N	14	349.425	18	313.2	425.5	6.3	20120816	0.344	0.141
C212727312N	25.25	335.25	27.75	294.75	441	3.5	20120817	0.286	0.169
C212866238N	64.75	274.05	68.75	211.725	302.6	3.7	20120920	0.16	0.183
C21286816N	67.5	34.2	64.75	0	171.3	4.6	20121007	0.16	0.239
C212860113S	72.5	167.175	57.75	69.975	527.6	8.6	20120929	0.269	0.224
C212955268S	56.75	295.2	56.25	240.75	364.9	0.5	20121015	0.306	0.224
C21296367S	65	89.325	60	49.05	233.8	7.1	20121030	0.247	0.272
C212975259N	74.75	276.3	76.5	240.3	110.6	2.8	20121015	0.102	0.127
C212971343N	72.25	360	73.25	321.3	139.8	1.5	20121009	0.211	0.217
C213074256N	69.5	360	76.75	146.925	756	1.9	20121110	0.251	0.188
C213045267N	44.25	286.65	50.5	247.725	328.8	9.1	20121111	0.243	0.232
C213062168S	59.75	197.1	62.5	135.675	361.6	2.6	20121119	0.214	0.169
C21306434S	64	81.225	62	0	448.3	1.4	20121130	0.202	0.235

Table C.10: Western Limb Cavities (CR 2131- CR 2142)

ID	S. Lat	S.Lon	E. Lat	E. Lon	Len	Tilt	Date	Height	Width
C213157183S	50.25	236.025	62.25	145.8	625.7	7.6	20121214	0.338	0.3
C213161322S	60.75	360	61.5	290.925	405	0.6	20121204	0.208	0.207
C213264294S	69.5	360	68	231.975	563.5	0.7	20130103	0.191	0.184
C213257159S	54.25	205.875	62.75	114.525	588.5	5.3	20130113	0.292	0.193
C213245145S	41.25	178.425	50.75	118.35	519.5	9	20130115	0.245	0.216
C213269276N	70.75	328.95	71.5	221.4	422.4	0.4	20130104	0.331	0.222
C213241336N	38.25	360	41	314.325	428.4	3.4	20121231	0.159	0.179
C21326113S	60.5	30.825	58	0	193.7	4.6	20130124	0.081	0.128
C213365290S	65	360	70	222.075	643.6	2.1	20130130	0.158	0.206
C213464266S	53.75	360	73.25	150.075	1161.4	5.3	20130228	0.119	0.123
C213480178N	79.75	221.85	80.25	147.6	156.6	0.4	20130307	0.244	0.298
C213565167S	58.75	324	72.75	0	1624.3	2.5	20130404	0.205	0.222
C21355371S	46.25	149.175	61	0	1088.8	5.6	20130330	0.326	0.287
C213552237N	53.75	292.95	53.75	175.725	841.4	0	20130329	0.234	0.18
C213579163N	79.5	186.975	75.75	143.325	122.3	4.9	20130405	0.159	0.126
C213658226S	50.75	360	67.25	83.25	1741.8	3.4	20130427	0.243	0.201
C213647115S	47.75	141.3	49.75	99	339.4	2.7	20130505	0.177	0.158
C213656169N	55	199.35	52.25	141.525	417.6	2.7	20130502	0.213	0.286
C213762127S	57	255.6	67.75	0	1444.6	2.4	20130601	0.281	0.237
C213746110S	45.25	175.05	46.5	60.075	971.8	0.6	20130603	0.278	0.204
C213781222N	89.75	267.525	74.5	180.45	235	9.9	20130526	0.329	0.308
C213867329S	72	360	68.5	298.35	256.4	3.2	20130613	0.168	0.141
C213866149S	70.5	232.65	64.75	93.6	646.3	2.4	20130627	0.192	0.203
C213940252N	41.5	294.975	41.25	222.075	664	0.2	20130716	0.238	0.247
C21397076S	71.25	144	62.5	0	694.7	3.5	20130730	0.163	0.172
C214065339S	64.25	360	66	319.05	210.2	2.4	20130806	0.221	0.249
C214068109S	73.25	161.1	66.25	69.975	392.2	4.4	20130823	0.242	0.213
C21405798N	49.25	146.7	67	51.3	648.4	10.5	20130824	0.236	0.249
C214041252N	40	279.9	47.25	230.4	443.8	8.3	20130812	0.256	0.241
C214163330N	59.5	360	65	305.1	317.4	5.7	20130903	0.203	0.214
C214151305N	50	325.35	51.5	281.925	334	2	20130904	0.218	0.14
C214169328S	68.5	360	71	283.275	323.8	1.9	20130902	0.328	0.291
C21415765N	58.5	125.325	60	0	778	0.7	20130921	0.358	0.236
C21417069S	70.5	124.425	73	0	474	1.2	20130923	0.192	0.262
C21424519S	47.5	41.175	47	0	339.3	0.7	20131023	0.167	0.185
C21423635N	33.5	64.575	38.25	9.45	545.3	4.9	20131022	0.431	0.31
C214269344N	70.25	360	75.25	325.575	138	8.3	20130929	0.391	0.265
C214245329N	40.5	360	46.25	293.175	593.7	4.9	20131001	0.207	0.169
C214231165N	18.75	213.975	44	117.225	1048.5	14.6	20131012	0.315	0.197
C21425753N	60	105.525	59.5	0	645.3	0.3	20131021	0.158	0.148
C214268205S	66.25	360	69.5	54.225	1398.5	0.6	20131009	0.173	0.199

Table C.11: Western Limb Cavities (CR 2143- CR 2159)

ID	S. Lat	S.Lon	E. Lat	E. Lon	Len	Tilt	Date	Height	Width
C214361304N	59	360	72.5	243.675	602.7	6.6	20131027	0.181	0.198
C214346307N	46.25	347.4	46.75	267.075	671.2	0.4	20131028	0.247	0.228
C214324183N	23.25	215.1	27.75	155.7	653.1	4.3	20131108	0.216	0.179
C214339126N	39	159.75	40.75	95.175	601.9	1.6	20131113	0.279	0.234
C21433346N	30	78.3	35	20.025	599.7	4.9	20131118	0.303	0.247
C21436454S	63.25	103.05	60.25	0	593.2	1.7	20131119	0.14	0.157
C214470193S	69.5	360	75	0	1333.9	0.9	20131204	0.18	0.176
C21443441N	34	70.875	35.25	16.425	544.1	1.3	20131116	0.292	0.336
C214570189S	65.75	360	78.75	0	1341.6	2.1	20131231	0.18	0.209
C21453367N	32	115.65	35.75	13.275	1032.8	2.1	20140109	0.246	0.219
C214565287N	68	322.875	62	263.025	315.6	5.7	20131225	0.193	0.172
C214536159N	41.75	186.975	34.5	137.925	476.6	8.4	20140102	0.471	0.319
C21467134S	66.5	81.45	68.25	0	380.9	1.2	20140208	0.175	0.186
C214671204S	67.75	248.175	73.5	153.225	388.7	3.5	20140126	0.237	0.317
C214668278N	76.25	330.075	63.5	209.7	526	6	20140123	0.322	0.356
C214777291S	70	360	84.75	221.625	408.5	6.1	20140218	0.306	0.247
C214750190N	46.25	236.7	52.25	140.625	764.7	3.6	20140224	0.237	0.207
C21475485S	50.5	107.775	60	68.4	295.8	13.6	20140303	0.208	0.235
C21476519S	61.25	43.65	69.25	0	242.2	10.4	20140309	0.336	0.288
C214869322S	68.5	360	70.25	285.3	320.1	1.3	20140314	0.317	0.263
C214936247N	38.25	268.2	33.5	228.6	393.8	6.8	20140415	0.228	0.141
C214974153S	72	283.275	78.75	0	872.1	1.4	20140422	0.185	0.173
C215074172S	73.25	360	79.25	0	1041.2	1	20140512	0.17	0.206
C21517692S	78.5	180.45	68.5	0	633.9	3.2	20140621	0.171	0.264
C215176329S	80	360	76	299.475	160.3	3.8	20140601	0.222	0.182
C215278210S	65.5	360	81.75	74.25	997.6	3.3	20140706	0.174	0.186
C215332324N	23.25	360	37.5	285.525	798.9	10.8	20140726	0.181	0.142
C215374316S	77	360	75.75	270.225	257.2	0.8	20140727	0.123	0.153
C21554017N	39.75	34.2	39.75	0	319.2	0	20141014	0.29	0.15
C215635341N	31	360	42.25	320.175	411.3	15.8	20141015	0.28	0.22
C215682350S	79.5	360	83.25	341.25	56.9	11.3	20141015	0.1	0.11
C21568305S	83.5	12.375	83.25	0	17.6	1.2	20141110	0.1	0.1
C215624114N	16.5	139.5	34	82.35	662.4	17	20141102	0.22	0.21
C215712206N	8.25	232.425	14.25	186.975	546	7.5	20141122	0.3	0.31
C21573712N	38.25	29.925	36.75	0	288.8	2.9	20141207	0.14	0.15
C215786166S	87.25	208.35	87.5	129.375	44	0.2	20141124	0.14	0.12
C21582894N	29.25	111.15	30.5	79.425	334.3	2.3	20141227	0.19	0.21
C215946291N	45.75	314.775	47.75	272.25	354.5	2.7	20150111	0.19	0.16
C21593907S	39.25	16.425	40.5	0	153.8	4.4	20150131	0.33	0.19

Bibliography

Amari, T., Luciani, J.F., Mikic, Z., Linker, J.: 1999, Three-dimensional Solutions of Magnetohydrodynamic Equationsfor Prominence Magnetic Support: Twisted Magnetic Flux Rope. *Astrophys. J. Lett.* **518**, L57. DOI. ADS.

Antiochos, S.K., Klimchuk, J.A.: 1991, A model for the formation of solar prominences. *Astrophys. J.* **378**, 372. DOI. ADS.

Antiochos, S.K., Dahlburg, R.B., Klimchuk, J.A.: 1994, The magnetic field of solar prominences. *Astrophys. J. Lett.* **420**, L41. DOI. ADS.

Aulanier, G., Demoulin, P.: 1998, 3-D magnetic configurations supporting prominences. I. The natural presence of lateral feet. *Astron. Astrophys.* **329**, 1125. ADS.

Aulanier, G., DeVore, C.R., Antiochos, S.K.: 2002, Prominence Magnetic Dips in Three-Dimensional Sheared Arcades. *Astrophys. J. Lett.* **567**, L97. DOI. ADS.

Babcock, H.D.: 1959, The sun's polar magnetic field. *Astrophys. J.* **130**, 364. DOI. ADS.

Babcock, H.W.: 1961, The Topology of the Sun's Magnetic Field and the 22-YEAR Cycle. *Astrophys. J.* **133**, 572. DOI. ADS.

Babcock, H.W., Babcock, H.D.: 1955, The Sun's Magnetic Field, 1952-1954. *Astrophys. J.* **121**, 349. DOI. ADS.

Balanovsky, J., Perepelkin, E.: 1928, The distribution of brightness in the solar corona of 1927 June 29. *Mon. Not. Roy. Astron. Soc.* **88**, 740. ADS.

Bąk-Stęślicka, U., Gibson, S.E., Fan, Y., Bethge, C., Forland, B., Rachmeler, L.A.: 2013, The Magnetic Structure of Solar Prominence Cavities: New Observational Signature Revealed by Coronal Magnetometry. *Astrophys. J. Lett.* **770**, L28. DOI. ADS.

Berger, T., Testa, P., Hillier, A., Boerner, P., Low, B.C., Shibata, K., Schrijver, C., Tarbell, T., Title, A.: 2011, Magneto-thermal convection in solar prominences. *Nature* **472**, 197. DOI. ADS.

Chae, J.: 2003, The Formation of a Prominence in NOAA Active Region 8668. II. Trace Observations of Jets and Eruptions Associated with Canceling Magnetic Features. *Astrophys. J.* **584**, 1084. DOI. ADS.

Chae, J., Wang, H., Qiu, J., Goode, P.R., Strous, L., Yun, H.S.: 2001, The Formation of a Prominence in Active Region NOAA 8668. I. SOHO/MDI Observations of Magnetic Field Evolution. *Astrophys. J.* **560**, 476. DOI. ADS.

Chen, J.: 1996, Theory of prominence eruption and propagation: Interplanetary consequences. *J. Geophys. Res.* **101**, 27499. DOI. ADS.

Cheng, X., Zhang, J., Saar, S.H., Ding, M.D.: 2012, Differential Emission Measure Analysis of Multiple Structural Components of Coronal Mass Ejections in the Inner Corona. *Astrophys. J.* **761**, 62. DOI. ADS.

Contopoulos, I., Kalapotharakos, C., Georgoulis, M.K.: 2011, Nonlinear Force-Free Reconstruction of the Global Solar Magnetic Field: Methodology. *Solar Phys.* **269**, 351. DOI. ADS.

DeVore, C.R., Antiochos, S.K.: 2000, Dynamical Formation and Stability of Helical Prominence Magnetic Fields. *Astrophys. J.* **539**, 954. DOI. ADS.

Dikpati, M., Charbonneau, P.: 1999, A Babcock-Leighton Flux Transport Dynamo with Solar-like Differential Rotation. *Astrophys. J.* **518**, 508. DOI. ADS.

Dove, J.B., Gibson, S.E., Rachmeler, L.A., Tomczyk, S., Judge, P.: 2011, A Ring of Polarized Light: Evidence for Twisted Coronal Magnetism in Cavities. *Astrophys. J. Lett.* **731**, L1. DOI. ADS.

Engvold, O.: 1989, Prominence environment. In: Priest, E.R. (ed.) *Dynamics and Structure of Quiescent Solar Prominences*, *Astrophysics and Space Science Library* **150**, 47. DOI. ADS.

Fan, Y.: 2010, On the Eruption of Coronal Flux Ropes. *Astrophys. J.* **719**, 728. DOI. ADS.

Fan, Y., Gibson, S.E.: 2006, On the Nature of the X-Ray Bright Core in a Stable Filament Channel. *Astrophys. J. Lett.* **641**, L149. DOI. ADS.

Forland, B.C., Gibson, S.E., Dove, J.B., Rachmeler, L.A., Fan, Y.: 2013, Coronal Cavity Survey: Morphological Clues to Eruptive Magnetic Topologies. *Solar Phys.* **288**, 603. DOI. ADS.

Fuller, J., Gibson, S.E.: 2009, A Survey of Coronal Cavity Density Profiles. *Astrophys. J.* **700**, 1205. DOI. ADS.

Fuller, J., Gibson, S.E., de Toma, G., Fan, Y.: 2008, Observing the Unobservable? Modeling Coronal Cavity Densities. *Astrophys. J.* **678**, 515. DOI. ADS.

Gibson, S.E., Fan, Y.: 2006, Coronal prominence structure and dynamics: A magnetic flux rope interpretation. *Journal of Geophysical Research (Space Physics)* **111**, 12103. DOI. ADS.

Gibson, S.E., Low, B.C.: 1998, A Time-Dependent Three-Dimensional Magnetohydrodynamic Model of the Coronal Mass Ejection. *Astrophys. J.* **493**, 460. DOI. ADS.

Gibson, S.E., Fludra, A., Bagenal, F., Biesecker, D., del Zanna, G., Bromage, B.: 1999, Solar minimum streamer densities and temperatures using Whole Sun Month coordinated data sets. *J. Geophys. Res.* **104**, 9691. DOI. ADS.

Gibson, S.E., Foster, D., Burkepile, J., de Toma, G., Stanger, A.: 2006, The Calm before the Storm: The Link between Quiescent Cavities and Coronal Mass Ejections. *Astrophys. J.* **641**, 590. DOI. ADS.

Gibson, S.E., Kucera, T.A., Rastawicki, D., Dove, J., de Toma, G., Hao, J., Hill, S., Hudson, H.S., Marqué, C., McIntosh, P.S., Rachmeler, L., Reeves, K.K., Schmieder, B., Schmit, D.J., Seaton, D.B., Sterling, A.C., Tripathi, D., Williams, D.R., Zhang, M.: 2010, Three-dimensional Morphology of a Coronal Prominence Cavity. *Astrophys. J.* **724**, 1133. DOI. ADS.

Gopalswamy, N., Shimojo, M., Lu, W., Yashiro, S., Shibasaki, K., Howard, R.A.: 2003, Prominence Eruptions and Coronal Mass Ejection: A Statistical Study Using Microwave Observations. *Astrophys. J.* **586**, 562. DOI. ADS.

Guhathakurta, M., Rottman, G.J., Fisher, R.R., Orrall, F.Q., Altrock, R.C.: 1992, Coronal density and temperature structure from coordinated observations associated with the total solar eclipse of 1988 March 18. *Astrophys. J.* **388**, 633. DOI. ADS.

Guhathakurta, M., Fludra, A., Gibson, S.E., Biesecker, D., Fisher, R.: 1999, Physical properties of a coronal hole from a coronal diagnostic spectrometer, Mauna Loa Coronagraph, and LASCO observations during the Whole Sun Month. *J. Geophys. Res.* **104**, 9801. DOI. ADS.

Guo, W.P., Wu, S.T.: 1998, A Magnetohydrodynamic Description of Coronal Helmet Streamers Containing a Cavity. *Astrophys. J.* **494**, 419. DOI. ADS.

Habbal, S.R., Druckmüller, M., Morgan, H., Scholl, I., Rušin, V., Daw, A., Johnson, J., Arndt, M.: 2010, Total Solar Eclipse Observations of Hot Prominence Shrouds. *Astrophys. J.* **719**, 1362. DOI. ADS.

Hathaway, D.H.: 2015, The Solar Cycle. *ArXiv e-prints*. ADS.

Hathaway, D.H., Rightmire, L.: 2010, Variations in the Sun's Meridional Flow over a Solar Cycle. *Science* **327**. DOI. ADS.

Heinzel, P., Schmieder, B., Fárník, F., Schwartz, P., Labrosse, N., Kotrč, P., Anzer, U., Molodij, G., Berlicki, A., DeLuca, E.E., Golub, L., Watanabe, T., Berger, T.: 2008, Hinode, TRACE, SOHO, and Ground-based Observations of a Quiescent Prominence. *Astrophys. J.* **686**, 1383. DOI. ADS.

Hoeksema, J.T., Liu, Y., Hayashi, K., Sun, X., Schou, J., Couvidat, S., Norton, A., Bobra, M., Centeno, R., Leka, K.D., Barnes, G., Turmon, M.: 2014, The Helioseismic and Magnetic Imager (HMI) Vector Magnetic Field Pipeline: Overview and Performance. *Solar Phys.* **289**, 3483. DOI. ADS.

Hudson, H., Schwenn, R.: 2000, Hot Cores in Coronal Filament Cavities. *Advances in Space Research* **25**, 1859. DOI. ADS.

Hudson, H.S., Bougeret, J.-L., Burkepile, J.: 2006, Coronal Mass Ejections: Overview of Observations. *Space Sci. Rev.* **123**, 13. DOI. ADS.

Hudson, H.S., Acton, L.W., Harvey, K.L., McKenzie, D.E.: 1999, A Stable Filament Cavity with a Hot Core. *Astrophys. J. Lett.* **513**, L83. DOI. ADS.

Illing, R.M.E., Hundhausen, A.J.: 1986, Disruption of a coronal streamer by an eruptive prominence and coronal mass ejection. *J. Geophys. Res.* **91**, 10951. DOI. ADS.

Karna, N., Hess Webber, S.A., Pesnell, W.D.: 2014, Using Polar Coronal Hole Area Measurements to Determine the Solar Polar Magnetic Field Reversal in Solar Cycle 24. *Solar Phys.* **289**, 3381. DOI. ADS.

Karna, N., Pesnell, W.D., Zhang, J.: 2015, Appearances and Statistics of Coronal Cavities During the Ascending Phase of Solar Cycle 24. *Astrophys. J.* **810**, 123. DOI. ADS.

Karna, N., Zhang, J., Pesnell, W.D., Hess Webber, S.A.: 2015, Study of the 3D Geometric Structure and Temperature of a Coronal Cavity Using the Limb Synoptic Map Method. *Astrophys. J.* **810**, 124. DOI. ADS.

Karpen, J.T.: 2015, Plasma Structure and Dynamics. In: Vial, J.-C., Engvold, O. (eds.) *Solar Prominences*, *Astrophysics and Space Science Library* **415**, 237. DOI. ADS.

Karpen, J.T., Antiochos, S.K.: 2008, Condensation Formation by Impulsive Heating in Prominences. *Astrophys. J.* **676**, 658. DOI. ADS.

Kawaguchi, I.: 1967, On the Dome Formation in the Corona around a Prominence observed at the Total Eclipse of 15 February 1961. *Solar Phys.* **1**, 420. DOI. ADS.

Kucera, T.A., Gibson, S.E., Schmit, D.J., Landi, E., Tripathi, D.: 2012, Temperature and Extreme-ultraviolet Intensity in a Coronal Prominence Cavity and Streamer. *Astrophys. J.* **757**, 73. DOI. ADS.

Kundu, M.R., Fuerst, E., Hirth, W., Butz, M.: 1978, Multifrequency observations of solar filaments at centimeter wavelengths. *Astron. Astrophys.* **62**, 431. ADS.

Lemen, J.R., Title, A.M., Akin, D.J., Boerner, P.F., Chou, C., Drake, J.F., Duncan, D.W., Edwards, C.G., Friedlaender, F.M., Heyman, G.F., Hurlburt, N.E., Katz, N.L., Kushner, G.D., Levay, M., Lindgren, R.W., Mathur, D.P., McFeaters, E.L., Mitchell, S., Rehse, R.A., Schrijver, C.J., Springer, L.A., Stern, R.A., Tarbell, T.D., Wuelser, J.-P., Wolfson, C.J., Yanari, C., Bookbinder, J.A., Cheimets, P.N., Caldwell, D., Deluca, E.E., Gates, R., Golub, L., Park, S., Podgorski, W.A., Bush, R.I., Scherrer, P.H., Gummin, M.A., Smith, P., Auker, G., Jerram, P., Pool, P., Soufli, R., Windt, D.L., Beardsley, S., Clapp, M., Lang, J., Waltham, N.: 2012, The Atmospheric Imaging Assembly (AIA) on the Solar Dynamics Observatory (SDO). *Solar Phys.* **275**, 17. DOI. ADS.

Leroy, J.L., Servajean, R.: 1966, Sur la brillance de la couronne blanche au voisinage des protubérances solaires. *Annales d'Astrophysique* **29**, 263. ADS.

Li, K.J., Li, Q.X., Gao, P.X., Shi, X.J.: 2008, Cyclic behavior of solar full-disk activity. *J.G.R.* **113**, 11108. DOI. ADS.

Lin, Y., Martin, S.F., Engvold, O.: 2008, Filament Substructures and their Interrelation. In: Howe, R., Komm, R.W., Balasubramaniam, K.S., Petrie, G.J.D. (eds.) *Subsurface and*

Atmospheric Influences on Solar Activity, *Astronomical Society of the Pacific Conference Series* **383**, 235. ADS.

Lites, B.W.: 2005, Magnetic Flux Ropes in the Solar Photosphere: The Vector Magnetic Field under Active Region Filaments. *Astrophys. J.* **622**, 1275. DOI. ADS.

Litvinenko, Y.E., Wheatland, M.S.: 2005, A Simple Dynamical Model for Filament Formation in the Solar Corona. *Astrophys. J.* **630**, 587. DOI. ADS.

Liu, Y., Hoeksema, J.T., Scherrer, P.H., Schou, J., Couvidat, S., Bush, R.I., Duvall, T.L., Hayashi, K., Sun, X., Zhao, X.: 2012, Comparison of line-of-sight magnetograms taken by the Solar Dynamics Observatory/Helioseismic and Magnetic Imager and Solar and Heliospheric Observatory/Michelson Doppler Imager. *Solar Phys.* **279**, 295. DOI. ADS.

López Ariste, A., Aulanier, G., Schmieder, B., Sainz Dalda, A.: 2006, First observation of bald patches in a filament channel and at a barb endpoint. *Astron. Astrophys.* **456**, 725. DOI. ADS.

Low, B.C.: 1980, On magnetostatic equilibrium in a stratified atmosphere. *Solar Phys.* **65**, 147. DOI. ADS.

Low, B.C.: 1994, Coronal mass ejections and magnetic helicity. In: Hunt, J.J. (ed.) *Solar Dynamic Phenomena and Solar Wind Consequences, the Third SOHO Workshop*, *ESA Special Publication* **373**, 123. ADS.

Low, B.C.: 1996, Solar Activity and the Corona. *Solar Phys.* **167**, 217. DOI. ADS.

Low, B.C.: 1997, . *Solar Phys.* **65**, 147. DOI. ADS.

Low, B.C.: 2001, Coronal mass ejections, magnetic flux ropes, and solar magnetism. *J. Geophys. Res.* **106**, 25141. DOI. ADS.

Low, B.C., Hundhausen, J.R.: 1995, Magnetostatic structures of the solar corona. 2: The magnetic topology of quiescent prominences. *Astrophys. J.* **443**, 818. DOI. ADS.

Mackay, D., Yeates, A.: 2012, The Sun's Global Photospheric and Coronal Magnetic Fields: Observations and Models. *Living Reviews in Solar Physics* **9**, 6. DOI. ADS.

Mackay, D.H., van Ballegooijen, A.A.: 2009, A Non-Linear Force-Free Field Model for the Evolving Magnetic Structure of Solar Filaments. *Solar Phys.* **260**, 321. DOI. ADS.

Mackay, D.H., Gaizauskas, V., Yeates, A.R.: 2008, Where Do Solar Filaments Form?: Consequences for Theoretical Models. *Solar Phys.* **248**, 51. DOI. ADS.

Mackay, D.H., Karpen, J.T., Ballester, J.L., Schmieder, B., Aulanier, G.: 2010, Physics of Solar Prominences: II–Magnetic Structure and Dynamics. *Space Sci. Rev.* **151**, 333. DOI. ADS.

Makarov, V.I., Sivaraman, K.R.: 1989, Evolution of latitude zonal structure of the large-scale magnetic field in solar cycles. *Solar Phys.* **119**, 35. DOI. ADS.

Marqué, C.: 2004, Radio Metric Observations of Quiescent Filament Cavities. *Astrophys. J.* **602**, 1037. DOI. ADS.

Marqué, C., Lantos, P., Delaboudinière, J.P.: 2002, Multi wavelength investigation of the eruption of a sigmoidal quiescent filament. *Astron. Astrophys.* **387**, 317. DOI. ADS.

Mouradian, Z., Soru-Escaut, I.: 1994, A new analysis of the butterfly diagram for solar filaments. *Astron. Astrophys.* **290**, 279. ADS.

Parenti, S.: 2014, Solar Prominences: Observations. *Living Reviews in Solar Physics* **11**, 1. DOI. ADS.

Parker, E.N.: 1955a, Hydromagnetic Dynamo Models. *Astrophys. J.* **122**, 293. DOI. ADS.

Parker, E.N.: 1955b, The Formation of Sunspots from the Solar Toroidal Field. *Astrophys. J.* **121**, 491. DOI. ADS.

Pesnell, W.D., Thompson, B.J., Chamberlin, P.C.: 2012, The Solar Dynamics Observatory (SDO). *Solar Phys.* **275**, 3. DOI. ADS.

Poland, A.I., Mariska, J.T.: 1986, A siphon mechanism for supplying prominence mass. *Solar Phys.* **104**, 303. DOI. ADS.

Priest, E.R., Hood, A.W., Anzer, U.: 1989, A twisted flux-tube model for solar prominences. I - General properties. *Astrophys. J.* **344**, 1010. DOI. ADS.

Priest, E.R., van Ballegooijen, A.A., Mackay, D.H.: 1996, A Model for Dextral and Sinistral Prominences. *Astrophys. J.* **460**, 530. DOI. ADS.

Rachmeler, L.A., Casini, R., Gibson, S.E.: 2012, Interpreting Coronal Polarization Observations. In: Rimmele, T.R., Tritschler, A., Wöger, F., Collados Vera, M., Socas-Navarro, H., Schlichenmaier, R., Carlsson, M., Berger, T., Cadavid, A., Gilbert, P.R., Goode, P.R., Knölker, M. (eds.) *Second ATST-EAST Meeting: Magnetic Fields from the Photosphere to the Corona.*, *Astronomical Society of the Pacific Conference Series* **463**, 227. ADS.

Rachmeler, L.A., Gibson, S.E., Dove, J.B., DeVore, C.R., Fan, Y.: 2013, Polarimetric Properties of Flux Ropes and Sheared Arcades in Coronal Prominence Cavities. *Solar Phys.*. DOI. ADS.

Reeves, K.K., Gibson, S.E., Kucera, T.A., Hudson, H.S., Kano, R.: 2012, Thermal Properties of a Solar Coronal Cavity Observed with the X-Ray Telescope on Hinode. *Astrophys. J.* **746**, 146. DOI. ADS.

Régnier, S., Walsh, R.W., Alexander, C.E.: 2011, A new look at a polar crown cavity as observed by SDO/AIA. Structure and dynamics. *Astron. Astrophys.* **533**, L1. DOI. ADS.

Rust, D.M., Kumar, A.: 1994, Helical magnetic fields in filaments. *Solar Phys.* **155**, 69. DOI. ADS.

Saito, K., Hyder, C.L.: 1968, A Concentric Ellipse Multiple-Arch System in the Solar Corona. *Solar Phys.* **5**, 61. DOI. ADS.

Saito, K., Tandberg-Hanssen, E.: 1973, The Arch Systems, Cavities, and Prominences in the Helmet Streamer Observed at the Solar Eclipse, November 12, 1966. *Solar Phys.* **31**, 105. DOI. ADS.

Scherrer, P.H., Wilcox, J.M., Svalgaard, L., Duvall, T.L. Jr., Dittmer, P.H., Gustafson, E.K.: 1977, The mean magnetic field of the sun - observations at Stanford. *Solar Phys.* **54**, 353. DOI. ADS.

Schmit, D.J., Gibson, S.E.: 2011, Forward Modeling Cavity Density: A Multi-instrument Diagnostic. *Astrophys. J.* **733**, 1. DOI. ADS.

Schou, J., Scherrer, P.H., Bush, R.I., Wachter, R., Couvidat, S., Rabello-Soares, M.C., Bogart, R.S., Hoeksema, J.T., Liu, Y., Duvall, T.L., Akin, D.J., Allard, B.A., Miles, J.W., Rairden, R., Shine, R.A., Tarbell, T.D., Title, A.M., Wolfson, C.J., Elmore, D.F., Norton, A.A., Tomczyk, S.: 2012, Design and ground calibration of the Helioseismic and Magnetic Imager (HMI) instrument on the Solar Dynamics Observatory (SDO). *Solar Phys.* **275**, 229. DOI. ADS.

Schwenn, R.: 2006, Space Weather: The Solar Perspective. *Living Reviews in Solar Physics* **3**. DOI. ADS.

Shea, M.A., Smart, D.F.: 2012, Space Weather and the Ground-Level Solar Proton Events of the 23rd Solar Cycle. *Space Sci. Rev.* **171**, 161. DOI. ADS.

Shimojo, M.: 2013, Unusual Migration of Prominence Activities in the Southern Hemisphere during Cycles 23-24. *Pub. Astron. Soc. Japan* **65**, 16. DOI. ADS.

Shimojo, M., Yokoyama, T., Asai, A., Nakajima, H., Shibasaki, K.: 2006, One Solar-Cycle Observations of Prominence Activities Using the Nobeyama Radioheliograph 1992-2004. *Pub. Astron. Soc. Japan* **58**, 85. DOI. ADS.

St. Cyr, O.C., Webb, D.F.: 1991, Activity associated with coronal mass ejections at solar minimum - SMM observations from 1984-1986. *Solar Phys.* **136**, 379. DOI. ADS.

Sterling, A.C., Moore, R.L.: 2004, External and Internal Reconnection in Two Filament-Carrying Magnetic Cavity Solar Eruptions. *Astrophys. J.* **613**, 1221. DOI. ADS.

Straka, R.M., Papagiannis, M.D., Kogut, J.A.: 1975, Study of a filament with a circularly polarized beam at 3.8 CM. *Solar Phys.* **45**, 131. DOI. ADS.

Su, Y., van Ballegooijen, A., Lites, B.W., Deluca, E.E., Golub, L., Grigis, P.C., Huang, G., Ji, H.: 2009, Observations and Nonlinear Force-Free Field Modeling of Active Region 10953. *Astrophys. J.* **691**, 105. DOI. ADS.

Sun, X., Hoeksema, J.T., Liu, Y., Zhao, J.: 2015, On Polar Magnetic Field Reversal and Surface Flux Transport During Solar Cycle 24. *Astrophys. J.* **798**, 114. DOI. ADS.

Tandberg-Hanssen, E. (ed.): 1995, *The nature of solar prominences*, *Astrophysics and Space Science Library* **199**. ADS.

Tang, F.: 1987, Quiescent prominences - Where are they formed? *Solar Phys.* **107**, 233. DOI. ADS.

Thompson, W.T.: 2006, Coordinate systems for solar image data. *Astron. Astrophys.* **449**, 791. DOI. ADS.

Tomczyk, S., Card, G.L., Darnell, T., Elmore, D.F., Lull, R., Nelson, P.G., Streander, K.V., Burkepile, J., Casini, R., Judge, P.G.: 2008, An Instrument to Measure Coronal Emission Line Polarization. *Solar Phys.* **247**, 411. DOI. ADS.

Topka, K., Moore, R., Labonte, B.J., Howard, R.: 1982, Evidence for a poleward meridional flow on the sun. *Solar Phys.* **79**, 231. DOI. ADS.

van Ballegooijen, A.A.: 2004, Observations and Modeling of a Filament on the Sun. *Astrophys. J.* **612**, 519. DOI. ADS.

van Ballegooijen, A.A., Martens, P.C.H.: 1989, Formation and eruption of solar prominences. *Astrophys. J.* **343**, 971. DOI. ADS.

Vásquez, A.M., Frazin, R.A., Kamalabadi, F.: 2009, 3D Temperatures and Densities of the Solar Corona via Multi-Spacecraft EUV Tomography: Analysis of Prominence Cavities. *Solar Phys.* **256**, 73. DOI. ADS.

von Klüber, H.: 1961, Photometric investigation of the inner solar corona using an eclipse plate of 1927 June 29. *Mon. Not. Roy. Astron. Soc.* **123**, 61. ADS.

Waldmeier, M.: 1941, *Ergebnisse und probleme der sonnenforschung, von dr. M. Waldmeier ... MIT 102 figuren.* ADS.

Waldmeier, M.: 1981, Cyclic variations of the polar coronal hole. *Solar Phys.* **70**, 251. DOI. ADS.

Wang, Y.-M.: 1999, The Jetlike Nature of He II λ304 Prominences. *Astrophys. J. Lett.* **520**, L71. DOI. ADS.

Wang, Y.-M., Stenborg, G.: 2010, Spinning Motions in Coronal Cavities. *Astrophys. J. Lett.* **719**, L181. DOI. ADS.

Wang, Y.-M., Nash, A.G., Sheeley, N.R. Jr.: 1989, Evolution of the sun's polar fields during sunspot cycle 21 - Poleward surges and long-term behavior. *Astrophys. J.* **347**, 529. DOI. ADS.

Webb, D.F., Davis, J.M., McIntosh, P.S.: 1984, Observations of the reappearance of polar coronal holes and the reversal of the polar magnetic field. *Solar Phys.* **92**, 109. DOI. ADS.

Wiegelmann, T., Neukirch, T., Ruan, P., Inhester, B.: 2007, Optimization approach for the computation of magnetohydrostatic coronal equilibria in spherical geometry. *Astron. Astrophys.* **475**, 701. DOI. ADS.

Wu, S.T., Guo, W.P.: 1997, Numerical MHD modeling of the solar driver for the destabilization of a coronal helmet streamer. *Advances in Space Research* **20**, 2313. DOI. ADS.

Wu, S.T., Guo, W.P., Wang, J.F.: 1995, Dynamical evolution of a coronal streamer-bubble system. 1: A self-consistent planar magnetohydrodynamic simulation. *Solar Phys.* **157**, 325. DOI. ADS.

Xia, C., Keppens, R., Antolin, P., Porth, O.: 2014, Simulating the in Situ Condensation Process of Solar Prominences. *Astrophys. J. Lett.* **792**, L38. DOI. ADS.

Zhang, J., Richardson, I.G., Webb, D.F., Gopalswamy, N., Huttunen, E., Kasper, J., Nitta, N.V., Poomvises, W., Thompson, B.J., Wu, C.-C., Yashiro, S., Zhukov, A.N.: 2007a, Correction to Solar and interplanetary sources of major geomagnetic storms (Dst = -100 nT) during 1996-2005. *Journal of Geophysical Research (Space Physics)* **112**, A12103. DOI. ADS.

Zhang, J., Richardson, I.G., Webb, D.F., Gopalswamy, N., Huttunen, E., Kasper, J.C., Nitta, N.V., Poomvises, W., Thompson, B.J., Wu, C.-C., Yashiro, S., Zhukov, A.N.: 2007b, Solar and interplanetary sources of major geomagnetic storms (Dst = -100 nT) during 1996-2005. *J. Geophys. Res.* **112**, 10102. DOI. ADS.

Curriculum Vitae

Nishu Karna was born in Janakpur, Nepal. She completed her first Bachelor degree in Physics in 2007 from Tri-Chandra Multiple College, Kathmandu, Nepal. In 2010, she completed her second Bachelor degree in Physics with Astrophysical Track from St. Cloud State University, St. Cloud, Minnesota. In Fall 2010 she enrolled in the Computational Sciences and Informatics graduate program at George Mason University in Fairfax, Virginia. She received her Masters degree in Computational Sciences from George Mason University in 2012. Beginning Fall 2010 she has worked under the supervision of Dr. William Dean Pesnell and Dr. Jie Zhang in the field of Solar Physics.